MBE Growth and Characterization of III-V Bismide Semiconductor Alloys for Mid- and Long-Wave Infrared Applications

by

Stephen T Schaefer

A Dissertation Presented in Fulfillment
of the Requirements for the Degree
Doctor of Philosophy

Approved October 2020 by the
Graduate Supervisory Committee:

Shane R. Johnson, Chair
Yong-Hang Zhang
Michael Goryll
Richard King

ARIZONA STATE UNIVERSITY

December 2020

ABSTRACT

The molecular beam epitaxy growth of the III-V semiconductor alloy indium arsenide antimonide bismide (InAsSbBi) is investigated over a range of growth temperatures and V/III flux ratios. Bulk and quantum well structures grown on gallium antimonide (GaSb) substrates are examined. The relationships between Bi incorporation, surface morphology, growth temperature, and group-V flux are explored. A growth model is developed based on the kinetics of atomic desorption, incorporation, surface accumulation, and droplet formation. The model is applied to InAsSbBi, where the various process are fit to the Bi, Sb, and As mole fractions. The model predicts a Bi incorporation limit for lattice matched InAsSbBi grown on GaSb.

The optical performance and bandgap energy of InAsSbBi is examined using photoluminescence spectroscopy. Emission is observed from low to room temperature with peaks ranging from 3.7 to 4.6 μm. The bandgap as function of temperature is determined from the first derivative maxima of the spectra fit to an Einstein single-oscillator model. The photoluminescence spectra is observed to significantly broaden with Bi content as a result of lateral composition variations and the highly mismatched nature of Bi atoms, pairs, and clusters in the group-V sublattice.

A bowing model is developed for the bandgap and band offsets of the quinary alloy GaInAsSbBi and its quaternary constituents InAsSbBi and GaAsSbBi. The band anti-crossing interaction due to the highly mismatched Bi atoms is incorporated into the relevant bowing terms. An algorithm is developed for the design of mid infrared GaInAsSbBi quantum wells, with three degrees freedom to independently tune transition energy, in-plane strain, and band edge offsets for desired electron and hole confinement.

The physical characteristics of the fundamental absorption edge of the relevant III-V binaries GaAs, GaSb, InAs, and InSb are examined using spectroscopic ellipsometry. A five parameter model is developed that describes the key physical characteristics of the absorption edge, including the bandgap energy, the Urbach tail, and the absorption coefficient at the bandgap.

The quantum efficiency and recombination lifetimes of bulk $InAs_{0.911}Sb_{0.089}$ grown by molecular beam epitaxy is investigated using excitation and temperature dependent steady-state photoluminescence. The Shockley-Read-Hall, radiative, and Auger recombination lifetimes are determined.

ACKNOWLEDGEMENTS

First and foremost I would like to acknowledge the continued support of my parents Edward and Janet Schaefer for my studies. I thank my advisor Dr. Shane Johnson for his steady guidance and invaluable knowledge of semiconductor physics and molecular beam epitaxy. I would also like to thank the other members of my committee, Dr. Yong-Hang Zhang, Dr. Michael Goryll, and Dr. Richard King, for their support of my research and their critical feedback.

I acknowledge financial support through research sponsored by Sandia National Laboratories, National Science Foundation (NSF) award DMR-1410393, and the Air Force Research Laboratory under agreement number FA9453-19-2-0004. I acknowledge further financial support from the Ira. A. Fulton Schools of Engineering Dean's Fellowship, ARCS Foundation Scholar Award, Barrett Electronic Materials Fellowship, and Pamela and Jack Saltich Fellowship. I also acknowledge the use of facilities in the Eyring Materials Center at Arizona State University.

TABLE OF CONTENTS

Page

LIST OF TABLES vi

LIST OF FIGURES ix

CHAPTER

1 INTRODUCTION 1

2 MOLECULAR BEAM EPITAXY OF III-V-Bi ALLOYS 7

2.1 MBE Growth of InAsSbBi 7

2.2 Structural and Chemical Properties of InAsSbBi 15

2.3 Kinetic Model for Molecular Beam Epitaxy Growth of InAsSbBi 23

2.4 Growth Model Fit Results and Discussion 48

3 OPTICAL PROPERTIES OF III-V SEMICONDUCTORS 62

3.1 Optical Absorption Edge in III-V Semiconductors 62

3.2 Carrier Recombination Measurements of InAsSb 93

3.3 Optical Properties of InAsSbBi Measured by Photoluminescence Spectroscopy 112

4 BANDGAP AND BAND OFFSETS IN III-V-Bi SEMICONDUCTOR ALLOYS 127

5 III-V-Bi ACTIVE LAYER DESIGN FOR MID-IR LASERS 138

6 CONCLUSIONS 147

REFERENCES 153

APPENDIX

A: CALCULATION OF Bi MOLE FRACTION UNCERTAINTY 163

APPENDIX Page

B: AFM FLATTENING PROCEDURE 169

C: CALCULATION OF DROPLET ACCUMULATION RATE 172

D: LITERATURE COMPARISON OF BANDGAP ENERGIES.....175

E: MATLAB CODE FOR MBE GROWTH MODEL FITTING ROUTINE.....182

LIST OF TABLES

Table Page

1. Description and Growth Conditions of the InAsSbBi Samples 10
2. Lattice Constant, In-Plane Strain, and Average Mole Fractions of the InAsSbBi Layers Determined by X-ray Diffraction and Photoluminescence Measurements ... 19
3. InAsSbBi Sample Cross Section, Growth Temperature, V/In flux Ratios, Excess V/In Flux Ratios, and Visual Surface Morphology 36
4. InAsSbBi Sample Cross Section, Growth Temperature, Group-V Mole Fractions, Group-V Incorporation Coefficients, and Mole Fraction Uncertainty 37
5. Key Droplet Coverage Statistics from Atomic Force Microscopy Analysis 39
6. InAsSbBi Layer Thickness, Volume per Unit Area of Metallic In and Bi, Total Atomic Density Contained Within Droplet Features, and Bi Droplet Accumulation Rate Relative to In Flux 41
7. Fit Options Specified for the fmincon() Function 45
8. Growth Model Parameters for the Globally Minimized Least-Squared Error on Bi, Sb, and As Mole Fractions 46
9. Physical and Electrical Characteristics of III-V Substrates Studied By Ellipsometry 72
10. Oxide Layer Thickness for Ellipsometry Models of III-V Wafers 73
11. Best Fit Parameters for the Absorption Coefficient Model and the Absorption Coefficient Knee for Semi-Insulating GaAs Samples A, B, and C, and Undoped GaSb, InAs, and InSb 75

Table Page

12. GaAs Bandgap Energy Determined by First Derivative Maximum of Extinction Coefficient, Absorption Coefficient, and Imaginary Dielectric Function. Also Shown are Bandgap Energies Determined from the Maximum Values of Refractive Index and Real Dielectric Function 78

13. Material Parameters and Calculated Absorption Amplitude at the Bandgap Energy 80

14. Sample and Material Parameters Used in Photoluminescence Measurement Analysis 101

15. Summary of Material Parameters Used in Calculation of Radiative Recombination Coefficient 105

16. Experimental Fitting Parameters, SRH Coefficients, Radiative Coefficients, and Auger Coefficients 107

17. Parameter Values for the InAsSbBi Bandgap Model in Eq. 46 as Function of Sb and Bi Mole Fraction and Temperature 117

18. Einstein Single Oscillator Model Parameters, Photoluminescence Width Parameters, and Bi and Sb Mole Fractions for Each Sample Listed in the Order of Decreasing Bandgap Energy 118

19. Material Parameters for the Constituent Binary and Ternary Alloys of InAsSbBi Used to Model the Unstrained and Strained Band Edge and Bandgap Energies 130

20. Material Parameters for the Constituent Binary and Ternary Alloys of GaAsSbBi Used to Model the Unstrained and Strained Band Edge and Bandgap Energies 132

Table Page

21. Bi, Sb, and As Mole Fraction Uncertainties Due to Bandgap Energy and Lattice Constant Measurement Uncertainty 168

22. Comparison of GaAs Bandgap Energies Measured in This Work with Those from the Literature 177

23. Comparison of GaSb Bandgap Energies Measured in This Work with Those from the Literature 179

24. Comparison of InAs Bandgap Energies Measured in This Work with Those from the Literature 180

25. Comparison of InSb Bandgap Energies Measured in This Work with Those from the Literature 181

LIST OF FIGURES

Figure Page

1. Low Temperature (0 K) Bandgap Energy as a Function of Lattice Constant for III-V-Bi Materials 3
2. Sample Cross-Sections for 210 nm Bulk InAsSbBi and 10 nm InAsSbBi Quantum Wells....8
3. Reflection High-Energy Electron Diffraction Images of the Surface Reconstructions During the Growth of the First InAsSb Barrier and InAsSbBi Quantum Well 12
4. Bi Incorporation Coefficient as a Function of Growth Temperature for Various As/In and Bi/In Flux Ratios 14
5. Coupled (004)-Plane X-Ray Diffraction Scan and Dynamical Diffraction Simulation for Nearly-Lattice Matched 380 °C - Grown InAsSbBi on GaSb....16
6. Rutherford Back-Scattering Spectrometry, Nomarski Optical Micrograph, and Scanning Electron Micrograph of InAsSbBi 21
7. Schematic of (100) Growth Surface Illustrating the Six Processes Occurring During Molecular Beam Epitaxy Growth 26
8. Unprocessed 100 μm by 100 μm Atomic Force Microscopy Images of 400 °C Grown Sample B and 420 °C Grown Sample M....38
9. Measured and Model Predicted Bismuth, Antimony, Arsenic, and Total Mole Fractions for the 400 °C and 420 °C Grown InAsSbBi Sample Set 50
10. Model Predicted Bismuth, Antimony, Arsenic, and Total Group-V Surface Coverage Fractions for 400 °C and 420 °C Grown InAsSbBi Sample Set 52

Figure Page

11. Model Predicted Bi Mole Fraction as a Function of Absolute As/In flux Ratio and Excess As/In Flux.....53

12. Model Predicted As/In, Sb/In, and Bi/In flux Ratios for Growth of InAsSbBi on GaSb at 400 °C and 420 °C.....55

13. Excess As/In Flux Ratio as a Function of Growth Temperature.....58

14. Ultimate Bi Mole Fraction Limit and Corresponding Bi/In, Sb/In, and As/In Flux Ratios as a Function of Growth Temperature for InAsSbBi Lattice Matched to GaSb 60

15. Normalized Model Absorption Coefficient as a Function of Normalized Energy ...69

16. Absorption Coefficient as a Function of Photon Energy Relative to the Bandgap for Semi-Insulating GaAs Sample A and Undoped GaSb, InAs, and InSb Substrates ..75

17. Complex Index of Refraction and Complex Dielectric Function of Three Different Semi-Insulating GaAs Samples Measured by Spectroscopic Ellipsometry.....76

18. The Calculated Absorption Amplitude and the Experimental Absorption Amplitudes and Absorption Knee Compared for GaAs, GaSb, InAs, and InSb 82

19. Comparison of GaAs Bandgap Energies at 297 K Determined from the Absorption Edge Model and the Measured Data for the Various Optical Constants and Analytical Methods.....85

20. Comparison of the Position of the First Derivative Maximum to the Model Parameter $E_p - E_g$ as a Function of Power Law p_g for GaAs, GaSb, InAs, InSb, and for E_u = 1 meV 87

Figure Page

21. The Ratio of the Model Parameters E_m/E_g and E_m/E_{ex} as a Function of Model Parameter p_g for GaAs, GaSb, InAs, and InSb....88

22. Cross Section of Sample Used for Photoluminescence Measurements of $InAs_{0.911}Sb_{0.089}$....98

23. Photon Recycling Factor, Photon Extraction Factor, and Photon Extraction Quantum Efficiency for Bulk InAsSb as Functions of Temperature....100

24. Excitation Density Over Detected Spontaneous Emission as a Function of Pump Power....103

25. Internal Excitation Density as a Function of the Internal Radiative Recombination Rate at Various Temperatures....104

26. SRH Coefficient and Auger Coefficient for Bulk InAsSb as Functions of Temperature....106

27. Carrier Concentration as a Function of Temperature at Various Excitation Levels for bulk InAsSb....108

28. Radiative Recombination Rate Plotted Versus Carrier Concentration at Various Temperatures for Bulk InAsSb....110

29. Auger Recombination Rate Plotted Versus Carrier Concentration at Various Temperatures for Bulk InAsSb....110

30. Total Recombination Rate Plotted Versus Carrier Concentration at Various Temperatures for Bulk InAsSb....111

Figure Page

31. Photoluminescence Spectra Measured at 70 K with a 100 mW (120 W/cm2) Excitation for InAsSb Reference Sample R2, 430 °C Grown InAsSbBi Sample A, 420 °C grown Sample B, and 400 °C Grown Sample C 113

32. Bandgap Energy as a Function of Temperature for Unstrained InAs, InAsSb, and InAsSbBi 114

33. Photoluminescence Spectra from Bulk InAs, $InAs_{0.911}Sb_{0.089}$, and $InAs_{0.900}Sb_{0.097}Bi_{0.003}$ at Several Temperatures 119

34. Photoluminescence Width Versus Thermal Energy for InAs, $InAs_{0.911}Sb_{0.089}$, and InAsSbBi Bulk and Quantum Well Samples 121

35. Low-Temperature Strained Bandgap Energy of InAsSbBi as a Function of Strain with Contours of Constant Sb and Constant Bi 123

36. Low-Temperature Bandgap of InAsSbBi on GaSb and GaAsSbBi on GaSb Versus In-Plane Biaxial Strain 134

37. Conduction Band Edge and Valence Band Edge as a Function of Ga Mole Fraction in GaInAsSb/AlGaAsSb and Bi Mole Fraction in GaInAsSbBi 135

38. Bandgap Energy of Lattice-Matched GaInAsSbBi as a Function of Ga Mole Fraction and Bi Mole Fraction 137

39. Effect of 1% Compressive Biaxial Strain on the Band Edge Position of GaInAsSbBi 140

40. Laser Design A Band Offsets and Refractive Index 142

41. Laser Design A Quantum Well at Low Temperature with 0.354 eV (3.50 um) Ground State Transition Energy and 0.999 Wavefunction Overlap Integral Squared 142

Figure Page

42. Laser Design B Band Offsets and Refractive Index 144

43. Laser Design B Quantum Well at Low Temperature with 0.354 eV (3.50 um) Ground State Transition Energy and 0.999 Wavefunction Overlap Integral Squared 144

44. Laser Design C Band Offsets and Refractive Index 145

45. Laser Design C Quantum Well at Low Temperature with 0.248 eV (5.00 um) Ground State Transition Energy and 0.999 Wavefunction Overlap Integral Squared 146

46. Low-Temperature Photoluminescence Width for 210 nm Thick Bulk InAsSbBi and 10 nm Thick InAsSbBi Quantum Wells from Table V in Ref. 1 165

47. Background Flattening Procedure for 100 μm by 100 μm Atomic Force Microscopy Images of 400 °C Grown Sample B 171

1: INTRODUCTION

The amazing advances in the understanding and utilization of semiconductor materials in the 20th and 21st centuries have transformed our society, and optoelectronic materials have played a key role in the establishment of this "Semiconductor Age". Optoelectronic devices such as LEDs, lasers, and photodetectors play a pivotal role in the function of nearly all consumer electronics. Within this broad class of optical devices, the infrared spectrum finds important applications in both commerce and government. Examples include medical imaging and diagnostics, autonomous vehicle sensors, telecommunications, and gas sensing among many others. Devices for these applications require high-performance materials that efficiently detect and emit infrared light. The III-AsSb material system alloyed with bismuth is attractive for these applications as it offers highly-tunable bandgaps using either thick lattice matched bulk layers or strain-balanced superlattices grown on readily available large-area GaSb substrates[1,2] that can be processed using mature III-V processing techniques. Moreover, bismuth is the largest nonradioactive element and is relatively nontoxic and abundant compared to other nearby heavy elements such as lead, thallium, or mercury.

Minimizing material strain and subsequent misfit dislocations is an important design consideration for high performance optoelectronic devices due to the limits imposed on epitaxial layer thickness and optical quality. Practical IR device designs demand high-quality feature thicknesses on the order of a wavelength, and hence coherently strained layers with thicknesses of several microns that is not attainable for materials with more than ~0.01% in-plane strain.[3] Quaternary III-V alloys have two degrees of freedom allowing the designer the ability to independently adjust strain and bandgap energy,

providing an efficient means of tuning bandgap energy without introducing high levels of detrimental strain.

The design space offered by III-V bismide alloys for infrared applications is illustrated in Fig. 1, where the related low-temperature ternary bandgaps are plotted as a function of lattice constant. The materials with negative bandgap energies are semimetallic. The shaded region indicates the bandgap energies and lattice constants accessible to InAsSbBi on GaSb with up to a -2% lattice mismatch that corresponds to a critical thickness[3] of approximately 10 nm. The InAsSb and InAsBi ternary compositions lattice matched to GaSb are identified as solid circles. Lattice matched InAsSbBi spans bandgaps from 0.324 to 0.104 eV (3.8 to 11.9 μm) at low temperature and 0.277 to 0.048 eV (4.5 to 25.8 μm) at room temperature (not shown), encompassing much of the mid- and long-wave infrared spectrum.

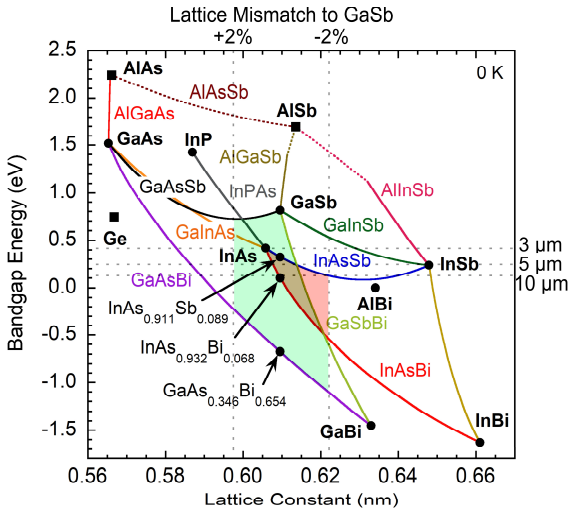

FIG. 1. Low temperature (0 K) bandgap energy as a function of lattice constant for III-V-Bi materials. The lattice mismatch to GaSb is shown on the upper horizontal axis. The ternary compounds lattice matched to GaSb are indicated by the arrows. Red and green shaded regions indicate the practical growth space bounded by ±2% lattice mismatch to GaSb for InAsSbBi and GaAsSbBi, respectively.

The incorporation of Bi in InAs reduces the room-temperature bandgap energy (0.356 eV) by approximately 51 meV/%Bi,[4] compared to a rate of 9.3 meV/%Sb for InAsSb.[5] Similarly, the incorporation of Bi in GaSb reduces the room temperature bandgap energy (0.729 eV) by 35 meV/%Bi,[6,7] compared to a rate of 9.6 meV/%In for GaInSb.[8] Since InAsSb lattice matched to GaSb exhibits a broken type-II band alignment with GaSb,[5,9] the quaternary alloys GaAsSbBi and InAsSbBi with dilute Bi mole fractions near the GaSb lattice constant are expected to have a type-II band lineup. Both lattice matched InAsSbBi layers and type-II strain-balanced InAsSbBi/GaAsSbBi superlattices can be grown on GaSb at arbitrary thicknesses. Indeed, one of the key features of quaternary alloys is the

ability to independently specify bandgap energy and strain,[2,4] and conduction/valence band alignment in the case of the strained layer superlattices.[9]

Accurate knowledge of the III-V-bismide material's absorption characteristics is required to design high-performance optoelectronic devices. The optical absorption edge is a key property determining the optical emission spectrum in direct-bandgap III-V semiconductors. It reflects the influence of numerous properties including the joint optical density of states, the optical transition oscillator strength, the presence of localized tail states within the bandgap, and defect-induced recombination and scattering. Precise and repeatable measurement of the absorption edge is crucial for assessing material quality and provides insight to the density of states and transition probabilities in the material. Specifically, these include the fundamental bandgap energy, E_g, the size of the absorption coefficient at the bandgap energy, α_g, and the Urbach tail energy, E_u, that characterizes localized tail states due to lattice disorder.[10-13]

In order to obtain these parameters from measured absorption data, analytical models of interband absorption[14-17] and empirical models of absorption edge broadening[10-13] have been developed to fit the intrinsic absorption edge of III-V semiconductors. Existing models usually treat the bulk interband absorption and exponential absorption edge broadening separately, a key drawback which complicates accurate measurement of bandgap energy from the absorption coefficient spectrum. In this work a new model composed of two terms describing the asymptotic interband absorption behavior and the exponential absorption edge broadening is developed. The model identifies both the fundamental bandgap energy E_g and the band edge broadening Urbach energy E_u as fitted parameters, as well as the absorption coefficient at the bandgap, α_g. Additionally, the

model provides some insight to the influence of free exciton absorption, the band structure, and optical transition strength of the material. Bandgap energy is also obtained by identifying the first derivative maximum energy from the absorption spectrum and is compared with the results obtained by fitting this model.

In addition to the optical absorption edge characteristics, the performance of many III-V optoelectronic devices is critically dependent on quantum efficiency making it desirable to understand nonradiative losses. This is particularly important for materials operating in the mid- and long-infrared spectrum (3 – 10 μm) where small-bandgap Auger losses[18,19] and point defects can significantly affect performance. Therefore, reliable lifetime and quantum efficiency measurements are desirable to feedback to material growth for the development of high optical quality devices.

Comprehensive studies of III-V-bismide alloy growth, band alignment, optical absorption, and recombination characteristics pave the way for use of these alloys in practical devices such as semiconductor diode lasers. A key factor determining lasing wavelength is the bandgap of the gain medium. While bulk InAsSbBi on GaSb provides tunable bandgap energies in mid-IR and long-IR, it forms a type-II band lineup with bulk AlGaAsSb on GaSb. This is a general concern in mid IR lasers at the GaSb lattice constant, where hole confinement is difficult to achieve when InAs based active materials are combined with GaSb based confinement materials. By adding Ga to the active material to form a quinary GaInAsSbBi alloy, the bandgap energy and valence band offset can be tuned independently to form heterostructures with the desired carrier confinement. Using a quinary alloy provides 3 degrees of design freedom that for example can be used to independently specify layer strain, bandgap energy, and heterojunction band offset.

Equivalently, for quantum well designs these degrees of freedom may be used independently control ground state transition energy, well thickness, and electron-hole wavefunction overlap, which directly influences the radiative recombination rate. The quinary alloy composition can be tuned to achieve mid-IR emission with type-I band alignments to typical barrier materials such as AlGaAsSb and even GaSb, providing the carrier confinement necessary for stimulated emission from lasers.

2: MOLECULAR BEAM EPITAXY OF III-V-Bi ALLOYS

2.1 MBE growth of InAsSbBi

The growth of InAsSbBi on (100) GaSb substrates with near unity Bi incorporation[2] occurs at comparatively low growth temperatures from 280 to 300 °C under low As/In flux overpressures, defined as the difference between incident As/In flux ratio and As mole fraction incorporated. These growths yield material with good structural quality, but photoluminescence is not observed; a result of short non-radiative recombination lifetimes, likely due to the presence of point defects associated with lower growth temperatures.[20-22]

This work examines InAsSbBi grown at temperatures from 400 to 430 °C that approach the optimal growth temperature of 450 °C for InAs. Nearly lattice matched InAsSbBi bulk and InAsSb/InAsSbBi/InAsSb quantum well structures are grown using a VG V80H solid source molecular beam epitaxy system on ¼ 50 mm (100)-oriented p-type GaSb substrates. The sample cross-sections are illustrated in Fig. 2 with 210 nm thick InAsSbBi layers shown in (a) and10 nm thick InAsSbBi quantum wells confined by InAsSb spacers shown in (b). The growths consist of a 500 nm GaSb buffer, a 10 nm InAs/10 nm AlSb partially strain-balanced barrier, an active region containing InAsSbBi bulk or quantum well layers, and a 10 nm AlSb/10 nm InAs barrier and cap layer. The GaSb buffer layer is grown at 500 °C except for the last 70 nm where the substrate temperature is reduced by 70 to 100 °C in preparation for the growth of InAsSbBi.

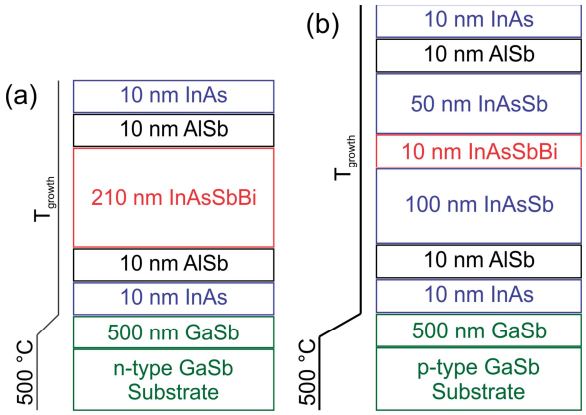

FIG. 2. Sample cross-sections for (a) 210 nm bulk InAsSbBi (samples A through D and I through R), and (b) 10 nm InAsSbBi quantum wells (samples E through G). The 10 nm thick compressive AlSb and tensile InAs barriers provide carrier confinement. Growth temperature profiles shown at the left.

Bulk InAs and lattice matched InAsSb reference samples are also grown. The InAs reference sample consists of 1 µm of InAs grown at 450 °C on a 50 mm (100)-oriented n-type InAs substrate that is sandwiched between 10 nm AlSb barriers with a 10 nm InAs capping layer. The InAsSb reference sample consists of 500 nm of lattice matched InAsSb grown at 430 °C on ¼ 50 mm (100)-oriented GaSb substrate that is sandwiched between 10 nm AlSb barriers with a 10 nm GaSb capping layer.[5]

The MBE growth rate is directly proportional to the incident group III flux[23,24] since group III elements including In do not desorb from the surface during MBE growth[23,24] due to their low vapor pressure.[25] The samples are grown with a constant In flux of 4.4×10^{14} cm^{-2} s^{-1} corresponding to an InAsSbBi on the GaSb growth rate of about 15 nm/min or 0.82 monolayers per second.[1] The In growth rate is calibrated by X-ray diffraction measurements of InAs/AlSb superlattices grown on GaSb and is maintained on an ongoing

basis from measurements of bulk InAsSb and InAsSbBi growths. The substrate temperature is measured using an Ircon Modline 3 (model 3G-10C05) pyrometer. To aid Bi incorporation, the constituent V/In flux ratios are comparatively lean for As/In at 0.900 and 0.977 and Sb/In at 0.080 and 0.120 and comparatively rich for Bi/In at 0.05 and 0.20. With As mole fractions from 89.1% to 93.5%, the fraction of the As flux incorporated is at or near unity and ranges from 0.96 to 1.00. With Sb mole fractions from 6.2% to 10.8% the fraction of Sb flux incorporated ranges from 0.69 to 0.90. With Bi mole fractions from 0.2% to 1.9% the fraction of Bi flux incorporated is relatively low at 0.02 to 0.19. The growth conditions are summarized in Table 1 for the InAs reference sample R_1, the InAsSb reference sample R_2, the InAsSbBi bulk samples A through D and H through R, and the InAsSbBi quantum well samples E through G.

TABLE 1. Description and growth conditions of the InAsSbBi samples.

Sample Description		Growth temp (°C)	Flux Ratios Bi/In	Sb/In	As/In	Surface Reconstruction	Surface Morphology
R_1 B2380	1000 nm InAs on (100) InAs	450	0.00	0.000	2.000	2×4	Specular
R_2 B2496	500 nm InAsSb on (100) GaSb	430	0.00	0.120	1.200	2×3	Specular
A B2511	210 nm InAsSbBi, (100) on-axis	400	0.05	0.120	0.940	2×4	Specular
B B2561	210 nm InAsSbBi, (100) on-axis	400	0.05	0.120	0.911	2×1	Rough
C B2562	210 nm InAsSbBi, (100) 1° to (011)	400	0.05	0.120	0.911	2×1	Rough
D B2563	210 nm InAsSbBi, (100) 4° to (111)	400	0.05	0.105	0.911	2×1	Rough
E B2566	10 nm InAsSbBi QW, (100) on-axis	400	0.10	0.100	0.911	2×4	Specular
F B2567	10 nm InAsSbBi QW, (100) 1° to (011)	400	0.10	0.100	0.911	2×1	Specular
G B2568	10 nm InAsSbBi QW, (100) 4° to (111)	400	0.10	0.100	0.911	2×1	Specular
H B2509	210 nm InAsSbBi, (100) on-axis	420	0.05	0.120	0.940	2×4	Specular
I B2513	210 nm InAsSbBi, (100) on-axis	420	0.05	0.120	0.940	2×4	Specular
J B2514	210 nm InAsSbBi, (100) on-axis	420	0.05	0.120	0.930	2×4	Specular
K B2515	210 nm InAsSbBi, (100) on-axis	420	0.05	0.120	0.920	2×4	Specular
L B2518	210 nm InAsSbBi, (100) on-axis	420	0.05	0.120	0.910	2×4	Specular
M B2519	210 nm InAsSbBi, (100) on-axis	420	0.05	0.120	0.900	2×4	Rough
N B2523	210 nm InAsSbBi, (100) on-axis	420	0.05	0.080	0.977	2×4	Specular
O B2524	210 nm InAsSbBi, (100) on-axis	420	0.05	0.080	0.947	2×4	Rough
P B2526	210 nm InAsSbBi, (100) on-axis	420	0.10	0.080	0.977	2×4	Specular
Q B2527	210 nm InAsSbBi, (100) on-axis	420	0.20	0.080	0.947	2×4	Rough
R B2505	210 nm InAsSbBi, (100) on-axis	430	0.10	0.120	0.911	2×4	Rough

Reflection high energy electron diffraction is used to monitor the surface reconstructions during the growth of the various materials. The As/In and Sb/In fluxes are calibrated prior to each growth by growing InAs on InAs and InSb on InSb and slowly lowering the V/In flux ratio until the transition from a group-V to a group-III rich surface reconstruction is observed. This procedure accurately and repeatably calibrates the one-to-one V/In flux ratios for As and Sb. The Bi flux is calibrated using scanning electron microscope measurements of the thickness of 190 nm of elemental Bi deposited on GaAs at 100 °C. The Bi flux calibration is maintained on an ongoing basis by Rutherford backscattering and x-ray diffraction measurements of InAsBi layers grown on GaSb substrates at 270 to 280 °C using near-unity As/In flux ratios, resulting in near-unity Bi incorporation.[26]

Over the 400 to 430 °C growth temperatures examined, a typical As terminated 2 x 4 surface reconstruction is observed during the growth of InAs. The presence of both an As and Sb flux during the growth of InAsSb results in a typical Sb terminated 2 x 3 surface reconstruction, while the addition of a Bi flux to the mix results in a transition to either a 2 x 4 or a 2 x 1 surface reconstruction. The surface reconstructions observed during the growth of InAsSbBi are listed in Table 1. The transition from a 2 x 3 to a 2 x 4 surface reconstruction is shown in Fig. 3 during the growth of an InAsSb/InAsSbBi/InAsSb quantum well at 400 °C (sample E). Moreover, the As/In and Sb/In flux ratios are simultaneously reduced to encourage Bi incorporation when the Bi shutter is opened. The 2 x 4 and 2 x 1 surface reconstructions are Bi-mediated, but may not represent a fully Bi terminated surface. The surfactant properties of Bi in InAs/InAsSb heterostructures are well documented,[27,28] with small Bi/In fluxes providing a beneficial effect on interface quality and photoluminescence.

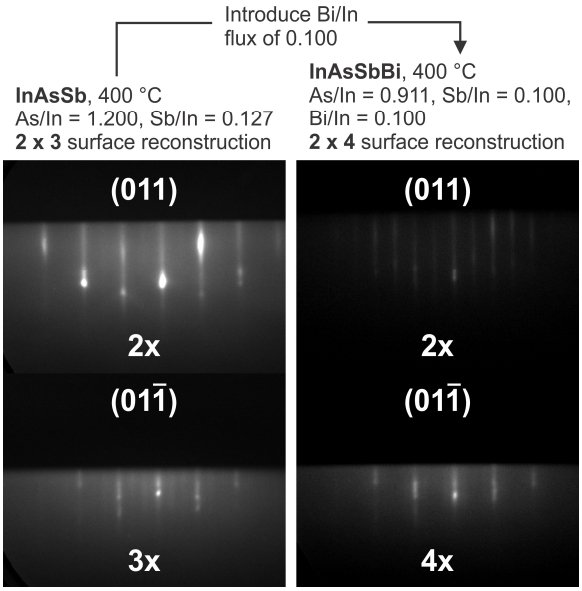

FIG. 3. Reflection high-energy electron diffraction images of the surface reconstructions during the growth of the first InAsSb barrier and InAsSbBi quantum well of sample E. The introduction of Bi flux modifies the Sb-terminated 2 x 3 surface reconstruction of InAsSb to a 2 x 4 reconstruction typical of an As-terminated surface.

The surface morphology for each sample is listed in Table 1 and is dependent on the InAsSbBi layer thickness and constituent As, Sb, and Bi fluxes. The surface reconstructions remain static throughout the growth of InAsSbBi, even for those that become visually rough, indicating that the InAsSbBi material continues high quality epitaxial growth on the microscopic scale regardless of what is occurring on an optical scale during the formation of relatively large surface features. This suggests that surface segregation and coalescing of excess surface Bi has a comparatively small effect on bulk incorporation and the material optical properties, a hypothesis supported by photoluminescence measurements discussed below. The two growths A and H with a slightly larger As/In flux ratio of 0.940 have a smooth surface, while the four growths B,

C, D, and R with As/In flux ratio of 0.911 are rough. The quantum well samples are smooth as the 10 nm InAsSbBi growth is short enough that a significant amount of Bi does not accumulate on the surface.

The growth temperature dependence of the Bi incorporation coefficient is shown in Fig. 4 for bulk InAsSbBi, including both samples presented here and low-temperature (280 – 320 °C) grown samples from previous work. The Bi incorporation coefficient is defined as the ratio of the Bi mole fraction to the incident Bi/In flux ratio. The Bi mole fractions are ascertained using Rutherford back-scattering, which provides a consistent measurement of the Bi mole fraction when the samples have droplet-free surfaces. In the relatively low temperature growth regime ≤ 320 °C two incorporation rates are identified, one where near unity Bi incorporation is observed when the As overpressure is near stoichiometric with As/In flux ratios of 0.91 to 0.97, and one where a fraction of the Bi incorporates when the As overpressure is more typical with an As/In flux ratio of 1.20. Nevertheless at higher growth temperatures, despite using near stoichiometric As/In flux ratios of 0.940, the Bi incorporation coefficient decreases exponentially as a function of temperature with characteristic temperature of about 16 °C, as indicated by the best fit solid curve and equation shown in Fig. 4. The As/In flux ratio is shown for each data point.

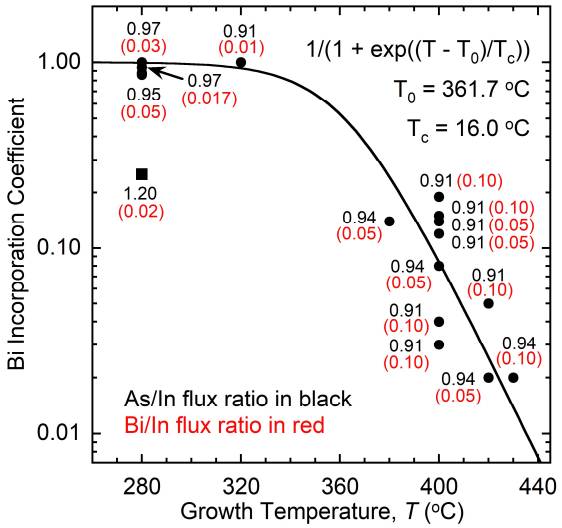

FIG. 4. Bi incorporation coefficient as a function of growth temperature for various As/In and Bi/In flux ratios as indicated beside each measurement shown as a solid circle. An exponential decrease in Bi incorporation is observed for the higher temperature growths, which is shown by the best fit solid curve and equation. The square data point for growth at 280 °C with As/In flux ratio of 1.20 is not included in the fit.

2.2 Structural and Chemical Properties of InAsSbBi

High-resolution X-ray diffraction measurements are performed to determine the layer thicknesses and in-plane strain for the InAsSbBi bulk and quantum well samples. Coupled $\omega - 2\theta$ scans of the (004) plane are collected using a Panalytical X'Pert Pro MRD triple-axis diffractometer for the InAsSbBi samples in Table 1. The measured intensity as a function of diffraction angle is then simulated using Panalytical X'Pert Epitaxy, a dynamical diffraction modeling program. The diffraction parameters for Bi and InBi are manually added to the software material database.[26,29] A measured x-ray diffraction scan and simulation is shown below in Fig. 5 for bulk InAsSbBi grown at 380 °C. Two layer peaks corresponding to the Ga(As)Sb buffer and InAsSbBi layer are distinguished. Arsenic incorporates unintentionally in the ~500 nm GaSb buffer at mole fractions of 0.12 – 0.55%. This unintentional As incorporation is a result of high As background pressure in the MBE chamber and is insufficient to induce relaxation of the GaSb buffer,[3] hence it is ignored in subsequent analysis of the material's optical properties.

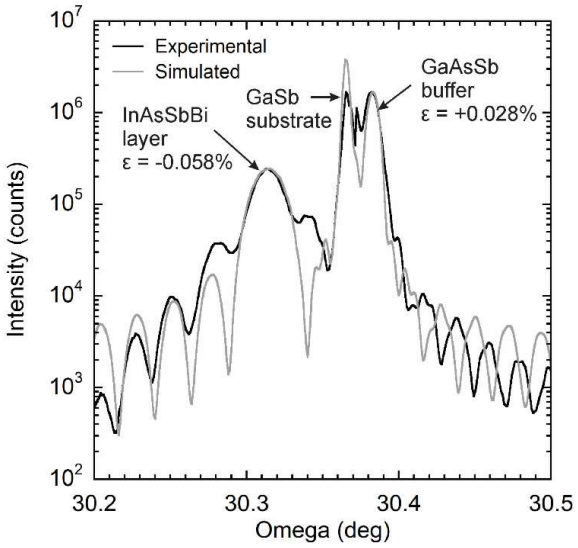

FIG. 5. Coupled (004)-plane x-ray diffraction scan and dynamical diffraction simulation for nearly-lattice matched 380 °C - grown InAsSbBi on GaSb. In-plane strain values displayed. Note the tensile peak near the GaSb substrate peak, which indicates unintentional As incorporation during GaSb buffer growth.

The lattice of a coherently strained epitaxial layer such as InAsSbBi is distorted in the growth direction and matched to the substrate lattice in the growth plane. For small levels of strain, the tetragonal distortion, $\varepsilon_{\perp}$, of the epitaxial lattice relative to the substrate lattice is accurately described to first order[30] as

$$\varepsilon_{\perp} = -\frac{\theta_{InAsSbBi} - \theta_{sub}}{tan(\theta_{sub})}. \quad (1)$$

Where the angular positions of the substrate and the InAsSbBi layer diffraction angles, θ_{sub} and $\theta_{InAsSbBi}$, are specified by the symmetric ω-2θ (400) X-ray diffraction pattern. The coherently strained InAsSbBi lattice constant, $a_{InAsSbBi}$, in terms of the unit cell tetragonal distortion and the substrate lattice constant, a_{sub}, is given as[30]

$$a_{InAsSbBi} = \left[\left(\frac{1-\nu_{InAsSbBi}}{1+\nu_{InAsSbBi}}\right)\varepsilon_{\perp} + 1\right] a_{sub} \,. \quad (2)$$

Poisson's ratio, $\nu_{InAsSbBi}$, is estimated using a linear interpolation of the binary values ν_{InAs} = 0.3521,[9] ν_{InSb} = 0.3530,[9] and ν_{InBi} = 0.3503.[26] For the compositions examined here, its value for InAsSbBi varies by less than 1 part in 1000 from 0.35213 to 0.35219. Therefore Poisson's ratio can be assumed to be constant with $\nu_{InAsSbBi}$ = 0.3522, which simplifies the relation in Eq. 2 as a given tetragonal distortion corresponds to a unique lattice constant, regardless of the mole fraction distribution.

The $InAs_{1-x-y}Sb_yBi_x$ lattice constant in terms of the known InAs, InSb, and InBi binary lattice constants is, assuming Vegard's law[31], given as

$$a_{InAsSbBi} = (1-x-y)a_{InAs} + ya_{InSb} + xa_{InBi} \,. \quad (3)$$

From which the Sb mole fraction in terms of the InAsSbBi lattice constant and Bi mole fraction is

$$y = \frac{a_{InAsSbBi} - a_{InAs}}{a_{InSb} - a_{InAs}} - x\frac{a_{InBi} - a_{InAs}}{a_{InSb} - a_{InAs}} \,. \quad (4)$$

This provides a family of Sb and Bi mole fractions for a given InAsSbBi lattice constant. Determining the individual mole fractions requires an additional measurement of, for example, the Bi mole fraction using Rutherford backscatering[26] or the bandgap energy using photoluminecence.

The in-plane biaxial strain is defined as $\varepsilon_{xx} = \varepsilon_{yy} = a_{sub}/a_{InAsSbBi} - 1$, the resulting out-of-plane uniaxial strain is $\varepsilon_{zz} = -\varepsilon_{xx}2\nu_{InAsSbBi}/(1-\nu_{InAsSbBi})$, and the tetragonal distortion in terms of layer strain is $\varepsilon_{\perp} = (\varepsilon_{zz} - \varepsilon_{xx})/(1+\varepsilon_{xx})$. The mole fraction relations in terms of diffraction angle and in-plane strain are provided in Eqs. 5 and 6, respectively.

$$y = \frac{a_{sub} - a_{InAs}}{a_{InSb} - a_{InAs}} - x\frac{a_{InBi} - a_{InAs}}{a_{InSb} - a_{InAs}} - \frac{\theta_{InAsSbBi} - \theta_{sub}}{tan(\theta_{sub})}\left(\frac{1 - \nu_{InAsSbBi}}{1 + \nu_{InAsSbBi}}\right)\frac{a_{sub}}{a_{InSb} - a_{InAs}} \quad (5)$$

$$y = \frac{a_{sub} - a_{InAs}}{a_{InSb} - a_{InAs}} - x\frac{a_{InBi} - a_{InAs}}{a_{InSb} - a_{InAs}} - \left(\frac{\varepsilon_{xx}}{1 + \varepsilon_{xx}}\right)\frac{a_{sub}}{a_{InSb} - a_{InAs}} \quad (6)$$

In this work on GaSb substrates Eq. 6 becomes

$$\mathrm{y} = 0.0893 - 1.3120 \cdot x - 14.4763 \cdot \left(\frac{\varepsilon_{xx}}{1 + \varepsilon_{xx}}\right). \quad (7)$$

A dynamical simulation that accounts for interference effects is required to determine the precise diffraction angles from an X-ray diffraction pattern that displays strong Pendellösung fringes due to thin film interference. The relations above are implicit in any simulation, but not necessarily directly apparent as inputs or outputs of the simulator, other than the various binary lattice constants and Poisson ratios that are in the simulator database. Therefore in practice, rather than extracting the tetragonal distortion from a dynamical simulation, a reasonable value for the Bi mole fraction is input into the simulator and the Sb mole fraction is adjusted until the simulated diffraction pattern matches that measured. The two mole fractions determine the InAsSbBi lattice constant (Eq. 3) and the subsequent in-plane strain. The exact Sb and Bi mole fractions are determined using their relationship given in Eqs. 4 or 6 along with an additional measurement related to mole fraction. When Poisson's ratio is not constant, the lattice constant and subsequent in-plane strain depends on the exact values of the mole fractions and the simulation is repeated until it converges to consistent mole fraction and strain values. The results are reported in Table

2, where the InAsSbBi layer lattice constant is given by Vegard's law in Eq. 3 and the in-plane strain is reported as $a_{GaSb}/a_{InAsSbBi} - 1$.

TABLE 2. Lattice constant, in-plane strain, and average mole fractions of the InAsSbBi layers as determined by X-ray diffraction and photoluminescence measurements.

Sample description	In-plane biaxial strain (%)	Lattice constant (Å)	Mole fractions (%)			Flux ratios			Growth temp (°C)	Bi rich droplets
			Bi	Sb	As	Bi/In	Sb/In	As/In		
R_1, 1 µm bulk InAs	-	6.0583	-	-	100	0.00	0.000	2.000	450	No
R_2, 500 nm bulk InAsSb	0.002	6.0958	-	8.91	91.09	0.00	0.120	1.200	430	No
A, bulk, (100) on-axis	-0.061	6.0996	0.58	9.06	90.36	0.05	0.120	0.940	400	No
B, bulk, (100) on-axis	-0.111	6.1027	0.71	9.61	89.68	0.05	0.120	0.911	400	Yes
C, bulk, (100) 1°to (011)	-0.151	6.1051	0.81	10.05	89.14	0.05	0.120	0.911	400	Yes
D, bulk, (100) 4°to (111)	-0.052	6.0991	0.58	8.92	90.50	0.05	0.105	0.911	400	Yes
E, quantum well, (100) on-axis	-0.025	6.0974	1.86	6.85	91.29	0.10	0.100	0.911	400	No
F, quantum well, (100) 1°to (011)	-0.099	6.1020	1.67	8.17	90.16	0.10	0.100	0.911	400	No
G, quantum well, (100) 4°to (111)	-0.120	6.1032	1.35	8.90	89.75	0.10	0.100	0.911	400	No
H, bulk, (100) on-axis	-0.080	6.1008	0.29	9.70	90.01	0.05	0.120	0.940	420	No
I, bulk, (100) on-axis	-0.054	6.0992	0.22	9.42	90.36	0.05	0.120	0.940	420	No
J, bulk, (100) on-axis	-0.057	6.0994	0.21	9.48	90.31	0.05	0.120	0.930	420	No
K, bulk, (100) on-axis	-0.055	6.0992	0.20	9.46	90.34	0.05	0.120	0.920	420	No
L, bulk, (100) on-axis	-0.077	6.1006	0.23	9.74	90.03	0.05	0.120	0.910	420	No
M, bulk, (100) on-axis	-0.070	6.1002	0.21	9.67	90.12	0.05	0.120	0.900	420	Yes
N, bulk, (100) on-axis	0.044	6.0863	0.12	6.48	93.40	0.05	0.080	0.977	420	No
O, bulk, (100) on-axis	0.158	6.0854	0.20	6.18	93.62	0.05	0.080	0.947	420	Yes
P, bulk, (100) on-axis	0.173	6.0863	0.29	6.28	93.43	0.10	0.080	0.977	420	No
Q, bulk, (100) on-axis	0.157	6.0861	0.33	6.18	93.49	0.20	0.080	0.947	420	Yes
R, bulk, (100) on-axis	-0.142	6.1046	0.18	10.76	89.06	0.10	0.120	0.911	430	Yes

In addition to x-ray diffraction strain measurements, an accurate measurement of either Bi or Sb mole fraction is required to precisely determine the InAsSbBi layer composition. Random Rutherford back-scattering spectrometry measurements were performed to determine Bi mole fraction. A 2.0 MeV He^{2+} ion beam is directed at the randomly-rotating sample and a passivated implanted planar silicon detector is used to detect the energy-dependent yield of the backscattered ions. The Rutherford backscattering analysis software RUMP[32] is used to simulate the ion yields for each element in the structure. Rutherford

backscattering is well-suited to detecting dilute concentrations of Bi due to the atom's large atomic mass.[2] The backscattered ion spectrum and RUMP simulation are shown in Fig. 6 for 380 °C - grown InAsSbBi and 430 °C – grown bulk InAsSbBi sample R. A distinct Bi signature is observed permitting accurate simulation of the measured ion yield and Bi mole fraction, indicated on the figure.

Rutherford backscattering does not provide accurate measurements of bulk Bi mole fraction in InAsSbBi samples with rough or droplet-covered surfaces. This is because Rutherford back-scattering is a surface sensitive measurement technique; ions backscattered directly from the sample surface contribute more strongly to the total yield than do ions backscattered from the middle of the sample.[33] This is apparent in Fig. 6(c) where a distinct peak in the backscattered ion yield is observed at about 1.85 MeV. This peak is attributed to the presence of Bi-rich surface droplets as shown in the scanning electron microscopy (SEM) image of the sample surface in Fig. 6(d). The droplet peak in the backscattered yield is well modeled by a 50 nm $InAs_{0.923}Sb_{0.039}Bi_{0.038}$ upper layer and $AlSb_{0.955}Bi_{0.045}$ and $InAs_{0.950}Bi_{0.050}$ capping layers, simulating a sample surface covered in approximately 5% Bi. In contrast the 380 °C grown sample with a smooth droplet-free surface as shown by Nomarski optical microscopy in Fig. 6(b) exhibits no irregularities in backscattered ion yield. Photoluminescence measurements yield luminescence at approximately the same wavelength from both samples. This shows that the Bi mole fraction obtained from simulation of Rutherford backscattering measurements of the droplet-covered sample is an overestimate of the bulk Bi incorporation.

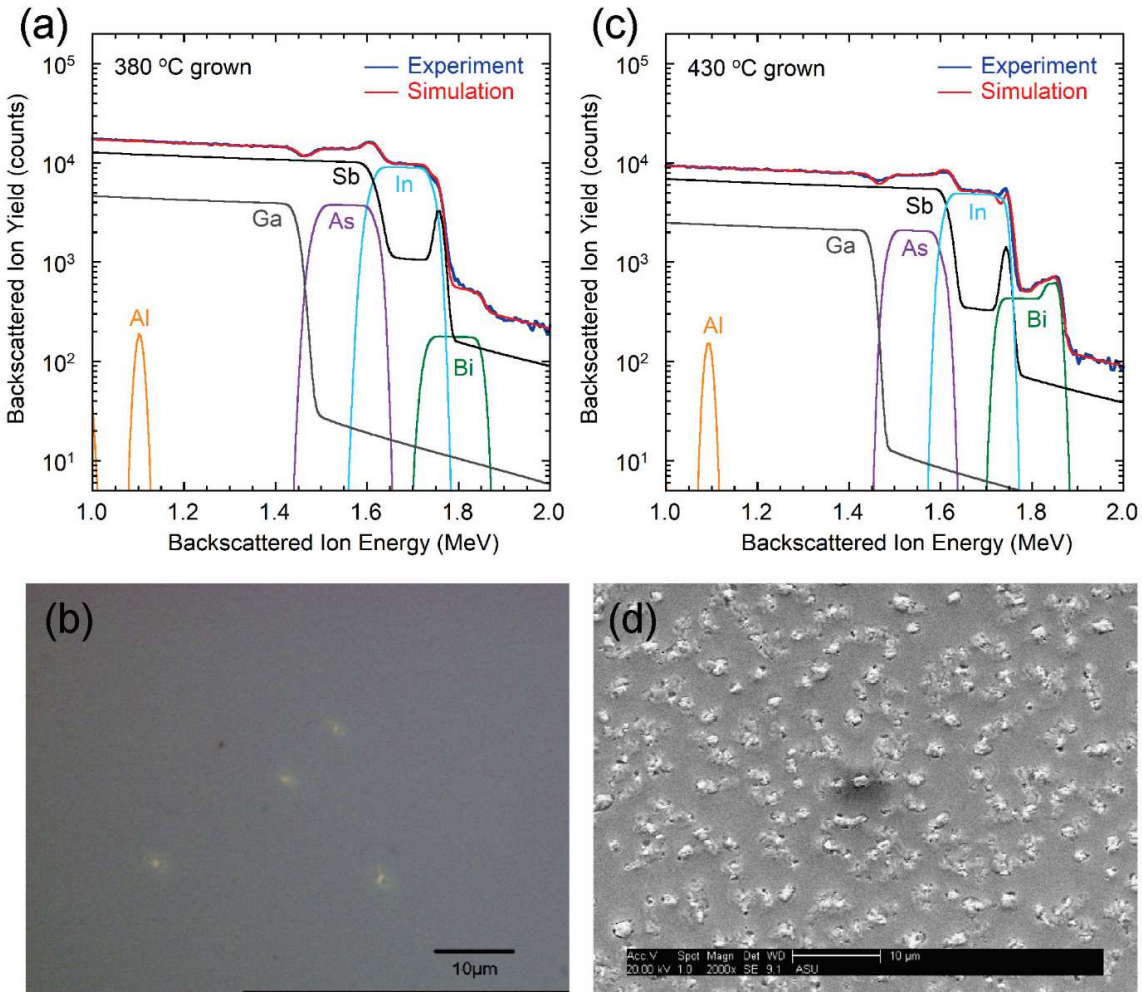

FIG. 6. .Rutherford back-scattering spectrometry of InAsSbBi. (a) Rutherford backscattering spectrum of 380 °C grown InAsSbBi and (b) Nomarski optical micrograph of sample surface indicating smooth droplet-free growth. (c) Rutherford backscattering spectrum of 430 °C grown sample R and (d) scanning electron micrograph of the surface, indicating dense Bi-rich droplet coverage.

High angle annular dark field (HAADF) scanning transmission electron microscopy (STEM) images were collected for InAsSbBi samples A, B, H, and R as described in Kosireddy *et al*.[34] Subtle thickness and contrast modulations in the images are due to lateral

composition modulation with darker regions indicating smaller average atomic mass and lighter regions rich in higher atomic masses such as Sb and Bi. These lateral composition and thickness modulations are present only at the upper interface and are further evidence of a 2-D surface segregation of Bi atoms which intensifies as growth proceeds and excess unincorporated Bi adatoms accumulate. The lateral scale of the thickness and composition modulations imaged by TEM are on the order of 10 nm whereas the Bi-rich droplet features in Fig. 6(b) and (d) are about 1 μm in diameter. This suggests that while segregation of Bi is microscopic in origin, the mobility of Bi adatoms is sufficiently great to diffuse several micrometers across the sample surface and coalesce into droplets.

2.3 Kinetic Model for Molecular Beam Epitaxy Growth of InAsSbBi

InAsSbBi is a highly mismatched alloy with isoelectronic group V elements of different sizes, ionicities, and electronegativities. Highly mismatched alloys can have miscibility gaps[3] over certain composition ranges that make them challenging to grow. Molecular beam epitaxy is a non-equilibrium technique well-suited to growth of bismide alloys, which exhibit a strong tendency for surface segregation and composition modulation[7,27,34-36] due to the very low solid solubility of Bi in host materials such as InAs.[37] Despite its wide use throughout research and production, the impact of molecular beam epitaxy growth conditions on chemical composition is not well understood. It is important to develop a comprehensive model for molecular beam epitaxy growth of bismide alloys to predict the outcome of growth experiments and guide the selection of growth temperatures and V/In flux ratios to maximize Bi incorporation. For example, when InAsSbBi is grown at the relatively low temperature of 280 °C, the Bi incorporation coefficient is known to be near unity[2], which is defined as the fraction of incident Bi flux that incorporates into the film. However, low temperature grown InAsSbBi results in greatly reduced optical quality.[2] By contrast InAsSbBi grown at relatively high temperatures of 400 °C to 430 °C exhibits greatly improved optical performance but with a much smaller Bi incorporation coefficients from 1 to 10%.[1] Identification of V/In flux ratios for maximum Bi mole fraction in the 400 °C to 430 °C temperature regime is key to extending optical performance further into the infrared spectrum.

Semi-empirical molecular beam epitaxy growth models have been successfully applied to dilute bismide alloys such as GaAsBi and GaSbBi. Lu *et al*[38] developed a three-term growth model for GaAsBi which accounts for the rates of formation of As-Ga-Bi bonds,

Ga-Bi bonds, and displacement of Bi from Ga-Bi bonds by As. A key concept in this model is the presence of a Bi surface coverage layer which is described by a Langmuir isotherm[39] and serves as a reservoir from which Bi can incorporate into the crystal termination layer. Lewis *et al*[40] expanded on this concept, recasting the problem in terms of the Ga/Bi ratio on the surface of the growing crystal. While both models succeed in predicting Bi mole fraction in GaAsBi across a range of Bi/Ga and As/Ga flux ratios, they do not include the influence of other mechanisms such as As-assisted desorption of Bi and are not easily extended to include the influence of a third group V element such as Sb. Furthermore, these models do not address the commonly observed formation of Bi-rich droplet features.[1,7,27,34,35] Tait and Millunchick[35] considered these additional mechanisms by developing a six-term growth model which includes the mechanisms of Bi adsorption, desorption, anion-assisted displacement of Bi from the crystal termination layer, anion-assisted removal of Bi from the surface, and Bi-rich droplet accumulation. This model provides an estimate of the Bi mole fraction in GaSbBi alloys[35] and accounts for the process of droplet formation. Furthermore it is readily extendable to growth of other bismide III-V ternary alloys such as GaAsBi and InAsBi and to quaternary alloys such as GaAsSbBi and InAsSbBi.

The kinetic growth model presented here borrows elements from the work of Lu *et al*[38], Lewis *et al*[40], and Tait and Millunchick[35] discussed in the introduction. These include the concepts of a weakly-bound surface layer of Bi distinct from the crystal termination layer,[35,38,40] the possibility of anion exchange with Bi incorporated in the termination layer,[35,38] and the accumulation of surface Bi into droplets.[35] Specifically this model of molecular beam epitaxy growth consists of six mechanisms, illustrated schematically in

Fig. 7. (1) Incident Bi flux physically adsorbs to the growth surface in a weakly-bound surface layer. (2) The physisorbed Bi desorbs from the surface, depleting the surface layer, or (3) chemisorbs to a group V lattice site in the crystal termination layer by forming an In-Bi bond. (4) Incident As or Sb flux displaces Bi from the crystal termination layer back into the physisorbed surface layer, breaking the In-Bi bond and replacing it with an In-As or In-Sb bond. (5) The desorption of excess As or Sb flux from the surface results in anion-assisted removal of Bi from the surface layer. Only the portion of the As or Sb flux that does not incorporate in the film is available to participate in anion-assisted removal of Bi by a co-desorption process. This stands in contrast to the model presented by Tait and Millunchick[4] which assumes that this process is proportional to the total incident As flux. Finally, (6) the coalescence of excess physisorbed Bi into Bi-rich droplet features commonly observed in bismide alloys.[1,7,27,34,35]

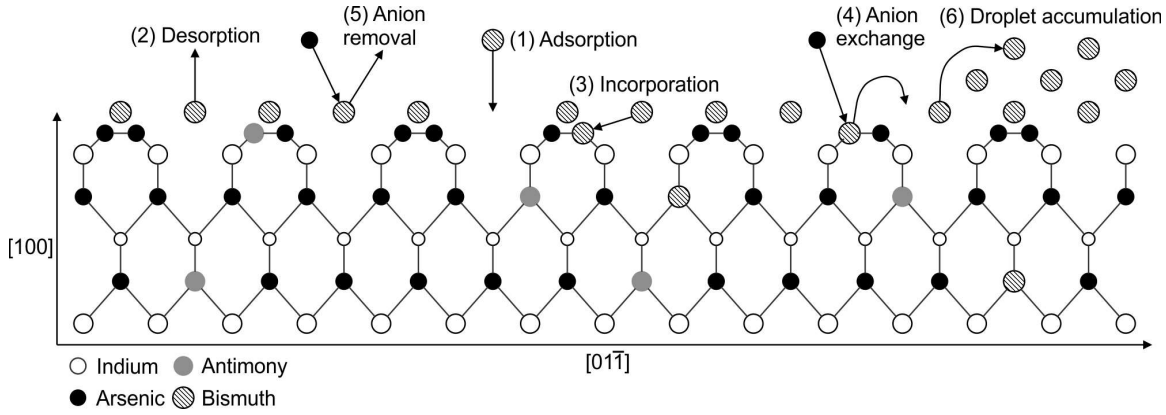

FIG. 7. Schematic of (100) growth surface illustrating the six processes occurring during molecular beam epitaxy growth. (1) Adsorption of incident Bi flux into the surface layer. (2) Desorption of Bi from the surface layer. (3) Incorporation of Bi on a group V lattice site. (4) Anion exchange wherein an incident As or Sb atom displaces a Bi atom from a group V lattice site back into the adsorbed surface layer. (5) Anion-assisted removal wherein the desorption of As or Sb from the surface participates in the removal of Bi from the surface layer. (6) Accumulation of adsorbed Bi into Bi-rich surface droplets.

The physisorbed Bi layer covers a fraction θ_{Bi} of the growth surface and is initially absent at the beginning of growth. It is assumed that i) all incident Bi flux physisorbs to this surface layer, ii) the Bi mole fraction in the crystal termination layer is the same as that of the bulk crystal, and iii) all processes affecting the Bi surface layer occur at its surface or interface with the crystal termination layer. A reflection of any part of the incident Bi flux without physisorption into the surface Bi layer is not distinguishable from the Bi desorption process, and is hence accounted for in that term.

In principle, the rate equations for the Bi surface coverage fraction θ_{Bi} and Bi mole fraction can be developed for the time-dependent growth of InAsSbBi given appropriate

knowledge of rates, probabilities, initial conditions, and the density of available sites in the surface layer and crystal termination layer. However these properties are generally not well characterized and the time-dependent solution of these equations is intractable except in the simplest cases. In this work the assumption of steady state growth is invoked, where the Bi surface coverage and mole fraction are constant with respect to time. Key to this assumption is that the relaxation time to achieve steady state growth is significantly less than the InAsSbBi epilayer growth duration. The Bi surface layer coverage is thus governed by the balance between mechanisms that increase the coverage and those that reduce it, with

$$F_{Bi} + \hat{x}\left(F_{As}P_{exc,As} + F_{Sb}P_{exc,Sb}\right) = \theta_{Bi}\left(R_{des} + R_{inc} + R_{dro} + \Delta F_{As}P_{rem,As} + \Delta F_{Sb}P_{rem,Sb}\right). \quad (8)$$

The terms on the left-hand side serve to increase the Bi surface coverage. The first term, F_{Bi}, is the incident Bi flux, labeled as (1) in Fig. 7. The second bracketed term is the anion-assisted exchange, labeled as (4) in Fig. 7. This process is proportional to the Bi mole fraction $\hat{x}$, the incident As and Sb fluxes F_{As} and F_{Sb}, and the probabilities $P_{exc,As}$ and $P_{exc,Sb}$ that an As or Sb atom displaces a Bi atom back into the surface layer.

The terms on the right-hand side scale with and serve to decrease the Bi surface coverage fraction θ_{Bi}. The first, second, and third terms are the rates of Bi self-desorption R_{des}, Bi incorporation R_{inc}, and droplet accumulation R_{dro}, labeled as (2), (3), and (6) respectively in Fig. 7. The fourth and fifth terms are anion-assisted removal of Bi by the excess As and Sb fluxes ΔF_{As} and ΔF_{Sb} and the associated probabilities $P_{rem,As}$ and $P_{rem,Sb}$, labeled as (5) in Fig. 7. Excess flux is defined as the fraction of incident flux that does not incorporate.

By similar logic the modeled Bi mole fraction $\hat{x}$ in the crystal termination layer is given by the sum of the rates of the incorporation and removal processes, with

$$\hat{x}F_{In} = \theta_{Bi}R_{inc} - \hat{x}\left(F_{As}P_{exc,As} + F_{Sb}P_{exc,Sb}\right). \tag{9}$$

Where F_{In} is the In flux that is observed to (and hence assumed to) fully incorporate into the surface termination layer. The anion-assisted exchange removes Bi from the crystal termination layer into the surface layer; a process that is proportional to the density of Bi occupied group V sublattice sites and hence the Bi mole fraction. Solving the system of Eqs. 8 and 9 yields the steady state solution for the Bi surface coverage fraction and the Bi mole fraction, with

$$\theta_{Bi} = \frac{F_{Bi}(F_{In} + F_{As}P_{exc,As} + F_{Sb}P_{exc,Sb})}{\left(F_{In} + F_{As}P_{exc,As} + F_{Sb}P_{exc,Sb}\right)\left(R_{des} + R_{dro} + \Delta F_{As}P_{rem,As} + \Delta F_{Sb}P_{rem,Sb}\right) + F_{In}R_{inc}}, \tag{10}$$

$$\begin{aligned}\hat{x} &= \frac{\theta_{Bi}R_{inc}}{\left(F_{In} + F_{As}P_{exc,As} + F_{Sb}P_{exc,Sb}\right)} \\ &= \frac{F_{Bi}R_{inc}}{\left(F_{In} + F_{As}P_{exc,As} + F_{Sb}P_{exc,Sb}\right)\left(R_{des} + R_{dro} + \Delta F_{As}P_{rem,As} + \Delta F_{Sb}P_{rem,Sb}\right) + F_{In}R_{inc}}.\end{aligned} \tag{11}$$

Eqs. 10 and 11 constitute the model for bismuth incorporation in the molecular beam epitaxy growth of InAsSbBi.

During the growth of III-V materials using mixed group-V fluxes with a cumulative flux greater than the cumulative group-III flux, the group-V elements terminate the growth surface and compete to incorporate into the growing crystal. At typical growth temperatures the group-III elements readily incorporate setting the growth rate of the III-V crystal. Therefore there is a similar set of surface coverage and incorporation relations for Sb and As, with respective mole fractions $\hat{y}$ and $\hat{z} = 1 - \hat{x} - \hat{y}$ and surface layer fractions θ_{Sb} and θ_{As} respectively. Like Bi, the presence of adsorbed Sb and As drives the incorporation of these elements into the crystal termination layer. The total fraction of

surface covered is given by the sum of the fraction covered by each group-V element, which is at most unity, with

$$\theta_{Bi} + \theta_{Sb} + \theta_{As} \leq 1. \quad (12)$$

In the model, the surface coverage fractions are constants of proportionality that mediate the rates of incorporation and removal of the various group-V elements from the surface layer. Driven by the relative fractions of the incoming group-V fluxes, each element competes for a fraction of the surface states that subsequently drives their incorporation into the group-V sublattice sites. The inequality in Eq. 12 comes from the fact that there can be surface states that are occupied by vacancies or group-III elements, particularly at near stoichiometric group-V fluxes. The interpretation of the surface coverage fractions, which do not specify the amount of a given element on the surface but instead the compositional makeup of the surface layer, is similar to that of the bulk mole fractions, which do not specify the thickness of the InAsSbBi layer but instead the compositional makeup of the bulk layer.

The model is linear in that the rates are constant for a given temperature and do not depend on the size of the flux or the surface coverage. This is a reasonable assumption when the excess group-V fluxes are relatively small compared to the total incoming flux, as in this work. However, the constant rates do not necessarily extrapolate to the presence of much larger excess group-V fluxes. In this case, desorption of the group-V material from the surface can exceed the growth rate, while the surface fractions and rates of incorporation remain roughly constant. The amount of group-V material on the surface likely increases, however as much of the increase is not as strongly bound to the surface layer, the desorption rate itself increases.

The three models for Bi, Sb, and As are symmetric with the exception of the absence of accumulation of Sb and As into surface droplets that are not observed when Bi is not present. The Sb model equations include the probabilities of As- and Bi-assisted exchange and removal, while the As model equations include the probabilities of Sb- and Bi-assisted exchange and removal. In general the probabilities relating the interactions between Bi, Sb, and As are not bidirectional. For example, the probability of a given As atom exchanging with a Bi atom in the crystal termination layer is not equal to the probability of a given Bi atom exchanging with an As atom.

The model parameters determined by experimental measurements are the In, As, Sb, and Bi fluxes (F_{In}, F_{As}, F_{Sb}, and F_{Bi}), the excess As, Sb, and Bi fluxes (ΔF_{As}, ΔF_{Sb}, and ΔF_{Bi}), and the Bi droplet accumulation rate (R_{dro}). The model parameters determined by a best fit of Eq. 11 and its equivalent forms to experimental measurements of the As, Sb, and Bi mole fractions are the desorption, incorporation, and droplet accumulation rates (R_{des}, R_{inc}, and R_{dro}), the exchange probabilities (P_{exc}), and the removal probabilities (P_{rem}), some of which may in general depend on growth temperature. In addition, the model outputs the best fit values for the surface coverage fractions θ_{Bi}, θ_{Sb}, and θ_{As}, and the mole fractions $\hat{x}$, $\hat{y}$, and $\hat{z}$.

In the absence of *in-situ* measurements of the droplet evolution, it is assumed that the presence of any surface droplets accumulate at an average rate of R_{dro} during growth, with the rate of accumulation determined using *ex-situ* measurements of the surface droplets after growth. It is observed that the Bi-rich droplets do not significantly desorb or diffuse across the growth surface during the growth of the InAsSbBi layers or the subsequent capping layers or during the ramp-down of the sample to room temperature. Therefore the

droplet surface coverage and associated droplet accumulation rate is treated as an independent variable in the analysis whose value is determined by surface morphology measurements using atomic force microscopy that are described below. These *ex-situ* measurements of the amount of Bi accumulated in surface droplets do not directly probe the droplet accumulation rate R_{dro} but rather the amount of incident Bi flux which accumulated in droplets, expressed as $\theta_{Bi}R_{dro}$ in Eq. 8. Therefore the Bi surface coverage θ_{Bi} and average droplet accumulation rate R_{dro} are determined using a self-consistent fitting procedure described below.

It is instructive to consider the limiting cases of the growth model, all subject to the assumption that the growth rate is group-III limited and the growth is group-V rich with an accumulated V/In flux ratio that is greater than or equal to one. As the probabilities of anion-assisted removal and anion exchange go to zero, the Bi surface layer coverage θ_{Bi} goes to $F_{Bi}/(R_{des}+R_{dro}+R_{inc})$ and the Bi mole fraction $\hat{x}$ goes to $(F_{Bi}/F_{In})\,R_{inc}/(R_{des}+R_{dro}+R_{inc}) = \theta_{Bi}R_{inc}/F_{In}$. In this case the Bi mole fraction is reduced to $\hat{x} = F_{Bi}/F_{In} - \theta_{Bi}(R_{des}+R_{dro})/F_{In}$. In this limit the Bi/In flux ratio drives the incorporation of Bi and the surface coverage θ_{Bi} drives the desorption and droplet accumulation of Bi. At growth temperatures that are insufficient to desorb surface Bi, the excess Bi flux that does not incorporate surface segregates and accumulates in surface droplets. In addition, if both the rates of desorption and droplet accumulation are small compared to the rate of incorporation, the Bi surface coverage θ_{Bi} approaches F_{Bi}/R_{inc} and the Bi mole fraction $\hat{x}$ approaches F_{Bi}/F_{In}. Physically this typically occurs during low temperature growth with small As overpressures and results in an alloy with a Bi mole fraction that equals the incident Bi/In flux ratio. Furthermore, when the Bi incorporation

rate R_{inc} is small compared to any of the processes that remove surface Bi, Eqs. 10 and 11 can be approximated to first order in R_{inc} as

$$\theta_{Bi} \approx \frac{F_{Bi}}{\left(R_{des} + R_{dro} + \Delta F_{As} P_{rem,As} + \Delta F_{Sb} P_{rem,Sb}\right)} \tag{13a}$$

$$\hat{x} \approx \frac{F_{Bi} R_{inc}}{\left(F_{In} + F_{As} P_{exc,As} + F_{Sb} P_{exc,Sb}\right)\left(R_{des} + R_{dro} + \Delta F_{As} P_{rem,As} + \Delta F_{Sb} P_{rem,Sb}\right)} \tag{13b}$$

Physically this corresponds to the case where the Bi does not significantly accumulate on the surface or incorporate in crystal, which typically occurs during high temperature growth or with the use of excessively large As and Sb fluxes. Furthermore to first order, the incorporation rate is

$$R_{inc} \approx \frac{\hat{x} F_{In}}{F_{Bi}}\left(1 + \frac{F_{As}}{F_{In}} P_{exc,As} + \frac{F_{Sb}}{F_{In}} P_{exc,Sb}\right)\left(R_{des} + R_{dro} + \Delta F_{As} P_{rem,As} + \Delta F_{Sb} P_{rem,Sb}\right), \tag{13c}$$

where $\hat{x} F_{In} / F_{Bi}$ is the Bi incorporation coefficient.

The growth model is applied to the nearly lattice matched bulk InAsSbBi and InAsSb/InAsSbBi/InAsSb quantum well structures grown by molecular beam epitaxy at 400 °C and 420 °C. The sample set examined here consists of bulk samples A though D and I through Q, and quantum well samples E through G. The sample cross-sections are illustrated in Fig. 2. Molecular beam epitaxy growth conditions and flux calibration procedures are discussed in detail in section 2.1, "MBE growth of InAsSbBi". The relevant growth conditions for the sample set are listed below in Table 3.

The quaternary alloy InAsSbBi requires two measurements sensitive to the group-V mole fractions to determine its chemical composition. The Bi and Sb mole fractions are determined from the unstrained bulk lattice constant ascertained from X-ray diffraction

measurements and the unstrained zero-temperature bandgap ascertained from steady state photoluminescence spectroscopy measurements.[1] The InAsSbBi tetragonal distortion, in-plane strain, and unstrained lattice constant is determined from symmetric $\omega - 2\theta$ X-ray diffraction measurements of the (400) crystal plane and subsequent dynamical simulations of the diffraction pattern. For all samples, the in-plane strain is observed to be less than 0.18%, with corresponding Matthews-Blakeslee critical thickness[3] greater than 210 nm, thus justifying the use of symmetric X-ray diffraction measurements to determine the InAsSbBi lattice constant.

The steady state photoluminescence spectroscopy measurements yield the bandgap energy as a function of temperature in the range from 12 K to 300 K. The samples are mounted in a closed-loop He-refrigerated cryostat and optically pumped using a modulated 785 nm laser diode at an average pump power of 100 mW, providing an active layer excitation density of 36 W/cm^2.[1] The photoluminescence is collected using a Nicolet Magna-IR 760 Fourier Transform infrared spectrometer with an InSb detector with a cutoff wavelength of 5.5 μm.[1] The pump laser is modulated at 50 kHz and the detector signal is fed through a phase-locked loop amplifier for improved signal-to-noise ratio.[1] The system optical throughput is measured and corrected using the spectrum from a Mikron M305 black body source at 800 °C.[1] The bandgap energy is determined from the first derivative maximum of the photoluminescence spectrum, which corresponds to the energy at which the joint optical density of states increases at its greatest rate.[1,4,5,41,42] An Einstein single oscillator model is fit to the temperature-dependent bandgap energy data to determine the low-temperature bandgap energy of each InAsSbBi sample.[1,5,11,43]

The measured InAsSbBi lattice constant and low-temperature bandgap energy are related to the Bi, Sb, and As mole fractions through Vegard's Law[31] and the InAsSbBi bandgap bowing model.[1] This system of two equations is numerically solved to determine the Bi and Sb mole fractions x and y respectively, from which the As mole fraction is given as $1 - x - y$. The uncertainty σ in the Bi and Sb mole fractions is given by the uncertainty in the determination of the InAsSbBi lattice constant from X-ray diffraction measurements and the uncertainty in the determination of the low temperature bandgap energy from temperature dependent photoluminescence measurements, with

$$\sigma = \sqrt{{\sigma_a}^2 + {\sigma_g}^2}. \tag{14}$$

Where σ_a is the uncertainty in the mole fraction inferred from the precision of the InAsSbBi lattice constant measurement and σ_g is the uncertainty in the mole fraction inferred from the frozen-in width of the InAsSbBi low-temperature photoluminescence spectrum, that in particular is significantly broadened by the addition of even dilute amounts of Bi. The broadening is a result of lateral composition modulation[5] and an increase in the density of localized tail states due to the size and electronic mismatch of Bi atoms, pairs, and clusters.[44-46] As such, σ_g is also a measure of the inhomogeneous range of the Bi mole fractions present. In Eq. 14 it is assumed that the two uncertainties are uncorrelated such that the covariance of σ_a and σ_g is zero. Details of the determination of the Bi, Sb, and As mole fraction uncertainties $\sigma_{Bi,i}$, $\sigma_{Sb,i}$, and $\sigma_{As,i}$ are provided in Appendix A.

Seven InAsSbBi samples grown at 400 °C and the ten samples grown at 420 °C are examined and summarized in Tables 3 and 4. The sample name, growth cross-section, growth temperature, incident group-V/In flux ratios, group-V mole fractions, mole fraction

uncertainty, and surface morphology (specular or droplet-covered) are provided. Also shown are the excess group-V/In flux ratios, which are determined by the incident flux ratio less the incorporated mole fraction. Although not directly controlled, the excess As/In flux ratio is targeted for each growth as it is observed to be a strong mediator of the incorporation of Bi and the formation of Bi-rich surface droplets. For the Sb/In and Bi/In flux ratios used here, As/In flux ratios near 0.9 result in near unity incorporation of the incident As flux, while larger values result in the presence of excess As at the growth surface. The total group-V flux is greater than unity, and in particular there is excess Sb flux present, therefore at the very least a small positive excess As flux is expected. Nevertheless, the reported excess As/In flux ratio is slightly negative for two growths, -0.2% for sample E and -0.1% for sample M. Nonetheless, these values are within that expected when the uncertainties in the mole fraction measurements and As/In flux calibrations are considered.

TABLE 3. InAsSbBi sample cross section, growth temperature, V/In flux ratios, excess V/In flux ratios, and visual surface morphology. The "Bulk" cross section is the 210 nm thick InAsSbBi layer shown in Fig. 2a. The "QW" cross section is the 10 nm thick InAsSbBi quantum well shown in Fig. 2b.

Sample	Cross section	Growth temperature (°C)	Flux ratios			Excess flux ratios			Surface morphology
			Bi/In	Sb/In	As/In	Bi/In	Sb/In	As/In	
A	Bulk	400	0.05	0.120	0.940	0.044	0.029	0.036	Specular
B	Bulk	400	0.05	0.120	0.911	0.043	0.024	0.014	Droplets
C	Bulk	400	0.05	0.120	0.911	0.042	0.020	0.020	Droplets
D	Bulk	400	0.05	0.105	0.911	0.044	0.016	0.006	Droplets
E	QW	400	0.10	0.100	0.911	0.081	0.032	-0.002	Specular
F	QW	400	0.10	0.100	0.911	0.083	0.018	0.009	Specular
G	QW	400	0.10	0.100	0.911	0.087	0.011	0.014	Specular
H	Bulk	420	0.05	0.120	0.940	0.047	0.023	0.040	Specular
I	Bulk	420	0.05	0.120	0.940	0.048	0.026	0.036	Specular
J	Bulk	420	0.05	0.120	0.930	0.048	0.025	0.027	Specular
K	Bulk	420	0.05	0.120	0.920	0.048	0.025	0.017	Specular
L	Bulk	420	0.05	0.120	0.910	0.048	0.023	0.010	Specular
M	Bulk	420	0.05	0.120	0.900	0.048	0.023	-0.001	Droplets
N	Bulk	420	0.05	0.080	0.977	0.049	0.015	0.043	Specular
O	Bulk	420	0.05	0.080	0.947	0.048	0.018	0.011	Droplets
P	Bulk	420	0.10	0.080	0.977	0.097	0.017	0.043	Specular
Q	Bulk	420	0.20	0.080	0.947	0.197	0.018	0.012	Droplets

TABLE 4. InAsSbBi sample cross section, growth temperature, group-V mole fractions, group-V incorporation coefficients, and mole fraction uncertainty. The "Bulk" cross section is the 210 nm thick InAsSbBi layer shown in Fig. 2a. The "QW" cross section is the 10 nm thick InAsSbBi quantum well shown in Fig. 2b.

Sample	Cross section	Growth temperature (°C)	Measured mole fractions (%)			Incorporation coefficients (%)			Mole fraction uncertainty (%)		
			Bi	Sb	As	Bi	Sb	As	Bi	Sb	As
A	Bulk	400	0.58	9.06	90.36	11.7	76.3	96.1	0.21	0.28	0.49
B	Bulk	400	0.71	9.61	89.68	13.7	77.4	98.4	0.22	0.28	0.50
C	Bulk	400	0.81	10.05	89.14	15.1	78.1	97.8	0.22	0.28	0.51
D	Bulk	400	0.58	8.92	90.50	11.0	80.2	99.3	0.21	0.28	0.49
E	QW	400	1.86	6.85	91.29	18.6	68.7	100.2	0.31	0.47	0.77
F	QW	400	1.67	8.17	90.16	16.7	81.7	99.0	0.31	0.47	0.76
G	QW	400	1.35	8.90	89.75	13.5	89.0	98.5	0.31	0.47	0.76
H	Bulk	420	0.29	9.70	90.01	5.9	82.8	95.8	0.18	0.28	0.46
I	Bulk	420	0.22	9.42	90.36	4.4	78.6	96.1	0.17	0.28	0.46
J	Bulk	420	0.21	9.48	90.31	4.2	79.1	97.1	0.17	0.28	0.45
K	Bulk	420	0.20	9.46	90.34	4.0	79.0	98.2	0.17	0.28	0.45
L	Bulk	420	0.23	9.74	90.03	4.6	81.2	98.9	0.18	0.28	0.46
M	Bulk	420	0.21	9.67	90.12	4.2	80.7	100.1	0.17	0.28	0.45
N	Bulk	420	0.12	6.48	93.40	2.4	81.7	95.6	0.16	0.28	0.44
O	Bulk	420	0.20	6.18	93.62	4.0	77.9	98.9	0.17	0.28	0.45
P	Bulk	420	0.29	6.28	93.43	2.9	79.1	95.6	0.18	0.28	0.46
Q	Bulk	420	0.33	6.18	93.49	1.7	77.9	98.7	0.19	0.28	0.47

The samples are examined by Nomarski optical microscopy using an Olympus MX50 optical microscope with Nomarski prism, analyzer, and polarizer components. The Nomarski images indicate that 400 °C grown samples B, C, D, and 420 °C grown samples M, O, and Q exhibit significant droplet coverage, while the remaining samples are specular with no observable droplet features. The results are listed as specular or droplets in Table 3, which are in agreement with the visual observations of either specular or hazy surfaces to the eye.

The six droplet-covered samples are investigated further using atomic force microscopy (AFM) to determine the total amount of Bi, N_{Bi}, accumulated in droplet features. The measurements are performed using a Brucker multimode 8 with a lateral scan range of 153

μm and vertical scan range of 5.5 μm. Typical images are displayed in Fig 8 for samples B and M. The images are 100 μm by 100 μm and are captured using ScanAsyst-AIR tips in the Bruker ScanAsyst-in-air imaging mode. The droplet morphology varies between samples with large droplets present on the 400 °C grown samples and small, sparse droplets on the 420 °C grown samples.

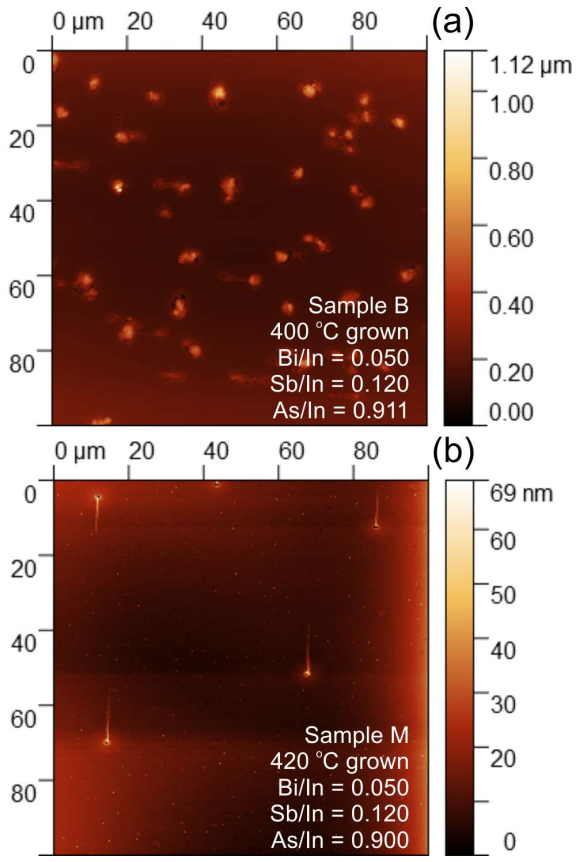

FIG. 8. Unprocessed 100 μm by 100 μm atomic force microscopy images of (a) 400 °C grown sample B and (b) 420 °C grown sample M. Large, dense droplets are observed on the 400 °C grown samples B, C, and D. By contrast droplets on 420 °C grown sample M are small and sparse with a streaky morphology.

The measured images are flattened and corrected for probe streaking using the Gwyddion[47] image analysis software according to the procedure described in Appendix B. This process converts the surface of the unprocessed image into a uniform plane on which the droplet features reside. The droplet features are then masked using height thresholding. The height threshold is 35 nm for 400 °C grown samples B, C, and D, while the threshold height varies from 4.0 to 10 nm for the 420 °C grown samples M, O, and Q. The volume contained within the masked droplets is then calculated in the Gwyddion software using a Laplacian background basis.[47] Dividing the total droplet volume by the image area of 10^4 μm^2 yields the volume per unit area, $h_{droplet}$, contained within the droplet features. The droplet coverage statistics from the AFM measurements are summarized in Table 5.

TABLE 5. Key droplet coverage statistics from atomic force microscopy (AFM) analysis, including density, average area of a single droplet, fraction of surface covered by droplets, and volume per unit area contained by droplets. Only the bulk InAsSbBi samples which exhibit significant roughness under Nomarski optical microscopy are shown. The remaining samples are specular and do not exhibit droplet features.

Sample	Growth temperature (°C)	Droplet density (cm^{-2})	Average droplet area (μm^{-2})	Droplet surface coverage (%)	Droplet volume/unit area (nm)
B	400	1.04×10^6	7.79	8.10	8.59
C	400	1.19×10^6	10.58	12.59	10.24
D	400	1.88×10^6	6.69	12.58	10.02
M	420	3.72×10^6	0.10	0.37	0.05
O	420	1.95×10^7	0.11	2.18	0.08
Q	420	1.11×10^7	0.09	1.04	0.08

Of the droplet covered samples, the ones grown at 400 °C (B, C, and D) have significantly more material on the surface in the form of droplets. Furthermore, for these three samples, the InAsSbBi layer thickness obtained from the X-ray diffraction (XRD) pattern simulations is significantly smaller than the growth target and hence indicates that in addition to excess Bi, a fraction of the incident In is consumed by the droplets during the Bi accumulation process. The loss of material is confirmed by thickness measurements from bright field transmission electron microscopy images[34] for all four bulk layers grown at 400 °C. The InAsSbBi layer thickness measurements are compared in Table 6. For the smooth droplet-free 400 °C grown samples and for all 420 °C grown samples, the X-ray diffraction simulated thicknesses agree within ± 4 nm of the target thicknesses, which lies within the precision of the measurement. This confirms that the incident In flux fully incorporates into the InAsSbBi layer of the droplet free samples and that there is no measurable decrease in the incorporation of In into the InAsSbBi layers of droplet covered samples M, O, and Q grown at 420 °C. Based on the experimental observations, the surface droplet features are hypothesized to be composed of a mixture of metallic Bi and In with insignificant amounts of Sb and As. However, since no measurable In loss is observed in the droplet covered samples grown at 420 °C, the droplets are considered to be comprised of Bi for calculation purposes.

TABLE 6. InAsSbBi layer thickness, volume per unit area of metallic In and Bi, total atomic density contained within droplet features, and Bi droplet accumulation rate relative to In flux. Droplet statistics are shown only for rough, droplet-covered samples B, C, D, M, O, and Q; all other samples are smooth and free of surface droplets. Indium is present in the droplets on the 400 °C grown samples only. The droplets are assumed to be composed entirely of metallic Bi for the 420 °C grown samples.

Sample	Growth temperature (°C)	InAsSbBi layer thickness (nm)			Volume/unit area (nm)		Total atomic density in droplets (cm^{-2})		Measured Bi droplet accumulation rate, $\theta_{Bi}R_{dro}$ (dimensionless)
		Target	XRD	Difference, h_{diff}	In, h_{In}	Bi, h_{Bi}	In, N_{In}	Bi, N_{Bi}	
A	400	210	210	-	-	-	-	-	0.00
B	400	210	194	16	7.35	1.24	2.82×10^{16}	3.49×10^{15}	9.45×10^{-3}
C	400	210	189	21	9.64	0.61	3.69×10^{16}	1.71×10^{15}	4.61×10^{-3}
D	400	210	190	20	9.20	0.82	3.53×10^{16}	2.30×10^{15}	6.22×10^{-3}
E	400	10	9.0	-	-	-	-	-	0.00
F	400	10	9.7	-	-	-	-	-	0.00
G	400	10	9.7	-	-	-	-	-	0.00
H	420	210	210	-	-	-	-	-	0.00
I	420	210	210	-	-	-	-	-	0.00
J	420	210	214	-	-	-	-	-	0.00
K	420	210	214	-	-	-	-	-	0.00
L	420	210	210	-	-	-	-	-	0.00
M	420	210	210	-	-	0.05	-	1.27×10^{14}	3.43×10^{-4}
N	420	210	210	-	-	-	-	-	0.00
O	420	210	214	-	-	0.08	-	2.23×10^{14}	6.02×10^{-4}
P	420	210	214	-	-	-	-	-	0.00
Q	420	210	214	-	-	0.08	-	2.28×10^{14}	6.17×10^{-4}

X-ray diffraction measurements provide a reliable measurement of the layer thickness and are used to determine the fraction of In lost to the droplets. The loss of material relative to the 210 nm target thickness is 16, 21, and 20 nm for samples B, C, and D respectively. This thickness difference, h_{diff}, is due to metallic In accumulation in the droplet features. The total amount of In per unit area, N_{In}, accumulated in the droplets is calculated directly from the thickness difference. The corresponding amount of metallic Bi per unit area, N_{Bi}, contained within the droplets is given from difference between the total volume per unit

area of droplet features, $h_{droplet}$, from Table 5 and the metallic In volume per unit area, h_{In}. Finally, the measured rate of Bi accumulation in droplets, $\theta_{Bi}R_{dro}$, is determined by dividing the amount of metallic Bi per unit area by the incident In flux. Table 6 summarizes the InAsSbBi layer thickness, volume per unit area of metallic In and Bi, the total amount of In and Bi per unit area, and the measured Bi droplet accumulation rate, $\theta_{Bi}R_{dro}$, expressed in dimensionless units where the In flux is one. The calculation details are shown in Appendix C.

It is noted that the droplets observed on 400 °C grown samples B, C, and D are composed primarily of In, which may be a product of growth for an extended duration at low As and Sb overpressures. Group III rich droplet formation is known to occur for molecular beam epitaxy growth of bismide alloys at unity or very slightly group-V rich V/III flux ratios.[48]

The inputs to the steady state kinetic growth model embodied by Eqs. 10 and 11 are the growth temperature, Bi/In, Sb/In, and As/In flux ratios, and excess Bi/In, Sb/In, and As/In flux ratios listed in Table 3, and the measured droplet accumulation rate $\theta_{Bi}R_{dro}$ listed in Table 6. Without loss of generality, all fluxes and rates are normalized to the incident In flux F_{In}. The growth model parameters R_{des}, R_{inc}, R_{dro}, P_{exc}, and P_{rem} are independent adjustable parameters that are fit to the measured Bi, Sb, and As mole fractions. All processes are assumed to scale with the In flux and the rates R_{des}, R_{inc}, and R_{dro} are normalized to the In flux such that they are expressed in dimensionless units where the In flux is one. The probabilities of anion-assisted exchange P_{exc} and removal P_{rem} are restricted to be between zero and one in the fit. The best fit values for the rates R_{des}, R_{inc}, and R_{dro} are restricted to be greater than or equal to zero.

The average droplet accumulation rate R_{dro} is determined self-consistently from the measured droplet accumulation rate $\theta_{Bi}R_{dro}$ listed in Table 6 and the modeled Bi surface coverage θ_{Bi} given by Eq. 10. Because the Bi surface coverage depends on the model parameters, an iterative process is utilized wherein the growth model parameters R_{des}, R_{inc}, $P_{exc,As}$, $P_{exc,Sb}$, $P_{rem,As}$, and $P_{rem,Sb}$ are fitted to the Bi mole fraction data as described below, the Bi surface coverage θ_{Bi} is calculated for each sample, and the average droplet uptake rate R_{dro} is calculated from the measured droplet accumulation rates:

$$R_{dro} = \frac{1}{N}\sum_{i=1}^{N}\frac{\theta_{Bi}R_{dro}[i]}{\theta_{Bi}[i]}, \tag{15}$$

Where $\theta_{Bi}R_{dro}[i]$ is the measured droplet accumulation rate reported in Table 6 and $\theta_{Bi}[i]$ is the calculated Bi surface coverage of the *i*-th droplet covered sample at each growth temperature; i.e. samples B, C, and D for 400 °C growth and samples M, O, and Q for 420 °C growth. An absolute tolerance of 10^{-5} (normalized to the In flux) on the average droplet accumulation rate R_{dro} and initial guess of θ_{Bi} = 0.2 is used, resulting in rapid convergence of the droplet accumulation rates.

The probabilities of anion-assisted exchange and removal are modeled as temperature independent parameters for each of the group-V elements, as these particular processes are not expected to depend on temperature for Bi, Sb, and As. The self-desorption rate of Sb and As are also modeled as temperature independent parameters, as they are expected to be small over this temperature range and thus do not vary significantly. On the other hand, the self-desorption rate for Bi and the incorporation rates for Bi, Sb, and As are treated as temperature dependent parameters. In particular, the incorporation of Bi is observed to be strongly dependent on temperature.[1]

The modeling work indicates that the temperature dependence of the incorporation and desorption rates are correlated in the fit. Therefore to attain a unique temperature dependence for each, the temperature dependence of the incorporation rate is fixed at that observed for the measured incorporation coefficients. The ratio $R_{inc}(420)/R_{inc}(400)$ of the 420 to 400 °C incorporation rates for Bi, Sb, and As are set at 26.1%, 98.5%, and 99.0% respectively, which are the ratios of the average values of the incorporation coefficients provided in Table 4. The temperature dependence of the self-desorption rates is determined from the fit of the model to the experimental data. As a result there is a total of 23 independently adjustable parameters fit to the Bi, Sb, and As mole fractions of the 17 samples. The independently adjustable parameters for each group-V element are $R_{des}(400)$, $R_{des}(420)$, $R_{inc}(400)$, $P_{exc,As}$, $P_{exc,Sb}$, $P_{rem,As}$, and $P_{rem,Sb}$, with $R_{inc}(420)$ determined separately from the temperature dependence of the incorporation coefficients. The Bi droplet uptake rates $R_{dro}(400)$ and $R_{dro}(420)$ are determined separately from the analysis of the droplet covered samples.

Fitting to the mole fractions is accomplished using the `fmincon()` nonlinear least-squares fitting function in MATLAB R2020a.[49] The objective function to be minimized by `fmincon()` is the squared error between measured and modeled group-V mole fractions, weighted by the uncertainty in each measured group-V mole fraction

$$\chi^2 = \chi^2_{Bi} + \chi^2_{Sb} + \chi^2_{As} = \sum_{i=1}^{N}\left[\frac{(x_i - \hat{x}_i)^2}{{\sigma_{Bi,i}}^2} + \frac{(y_i - \hat{y}_i)^2}{{\sigma_{Sb,i}}^2} + \frac{(z_i - \hat{z}_i)^2}{{\sigma_{As,i}}^2}\right]. \qquad (16)$$

Where x_i, y_i, and z_i are the measured Bi, Sb, and As mole fractions for the i-th sample, $\hat{x}_i$, $\hat{y}_i$, and $\hat{z}_i$ are the modeled Bi, Sb, an As mole fractions, and $\sigma_{Bi,i}$, $\sigma_{Sb,i}$, and $\sigma_{As,i}$ are the Bi, Sb, and As mole fraction uncertainties from Table 4.

In the model fit the measured mole fractions sum to unity, with $x_i + y_i + z_i = 1$, and modeled mole fractions for the best fit parameters sum to be near unity within an uncertainty of -2.3/+2.1%. Since the samples are grown under group-V rich conditions where very few surface layer vacancies or group-III elements are expected, the surface coverage fractions are constrained to be near unity in the model. In practice it is not possible to find a set of model parameters that exactly satisfy the unity surface coverage constraint for each of the 17 samples examined. Therefore a surface coverage fraction range of $0.9 \leq \theta_{Bi} + \theta_{Sb} + \theta_{As} \leq 1.1$ is implemented as a nonlinear constraint in MATLAB's `fmincon()` function.

A satisfactory fit quality is difficult to acquire as the number of fitting parameters increases. Therefore the fit options must be judiciously chosen so a good fit is achieved. The default 'interior-point' algorithm provided by MATLAB is used as it handles bounds on the fitting parameters. The fit options including limits, tolerances, and iterations are shown in Table 7.

TABLE 7. Fit options specified for the `fmincon()` function. Fit options not listed use the default values provided in MATLAB R2020a.[49]

Fit option	Value
`options.Algorithm`	`Interior-point`
`options.ObjectiveLimit`	`1e-20`
`options.OptimalityTolerance`	`1e-7`
`options.StepTolerance`	`1e-12`
`options.MaxFunctionEvaluations`	`1e4`
`options.MaxIterations`	`2e3`
`options.ConstraintTolerance`	`1e-6`

Stochastic initialization is used to locate the global minimum of the fit. A set of 1000 initial conditions is randomly generated for the growth model parameters. The fitting algorithm is iterated for each of the 1000 sets of initial conditions and the minimized least-squared error given by Eq. 16 is evaluated. A global minimum of $\chi^2 = 160.09$ for the combined 400 °C and 420 °C sample set is identified. The individual sums of squared residuals for Bi, Sb, and As are χ^2_{Bi} = 6.13, χ^2_{Sb} = 20.05, and χ^2_{As} = 133.92. The best fit parameters are summarized in Table 8 below.

TABLE 8. Growth model parameters for the globally minimized least-squared error on Bi, Sb, and As mole fractions.

Bismuth parameters	Rates (relative to In flux)			Probabilities			
	R_{des}	R_{inc}	R_{dro}	$P_{exc,As}$	$P_{exc,Sb}$	$P_{rem,As}$	$P_{rem,Sb}$
400 °C growth	0.3992	0.1246	0.0669	0.7816	0.2019	0.7013	0.4381
420 °C growth	0.6878	0.0325	0.0053				
Antimony parameters	Rates (relative to In flux)			Probabilities			
	R_{des}	R_{inc}	R_{dro}	$P_{exc,As}$	$P_{exc,Bi}$	$P_{rem,As}$	$P_{rem,Bi}$
400 °C growth	0.1078	0.7975	-	0.2125	0.1185	0.6567	0.4501
420 °C growth	0.1116	0.7856	-				
Arsenic parameters	Rates (relative to In flux)			Probabilities			
	R_{des}	R_{inc}	R_{dro}	$P_{exc,Sb}$	$P_{exc,Bi}$	$P_{rem,Sb}$	$P_{rem,Bi}$
400 °C growth	0.0242	1.3891	-	0.0265	0.0015	0.0732	0.0333
420 °C growth	0.0351	1.3752	-				

Allowing the other model parameters, such as the probabilities of anion-assisted exchange or removal, to vary with growth temperature results in marginal reductions of less than 1% in the normalized sum of residuals χ^2. However in such cases the fitted values of the parameters vary orders of magnitude from 400 °C to 420 °C which is not a physically plausible or interpretable result. Therefore only the desorption rate R_{des}, incorporation

rate R_{inc}, and Bi droplet accumulation rate R_{dro} are allowed to vary with temperature while all other parameters are held constant, which leads to physically interpretable fit results.

2.4 Growth Model Fit Results and Discussion

The growth model presented in Section 2.3, "Kinetic Model for Molecular Beam Epitaxy Growth of InAsSbBi", important insights to the physics of group-V incorporation and desorption during growth of mixed III-V bismide alloys. The model predicts the chemical composition of InAsSbBi given the key molecular beam epitaxy inputs of growth temperature and V/In flux ratios. Furthermore, the model predicts growth temperature dependent limits to the achievable Bi incorporation.

It is evident from the growth model parameters listed in Table 8 that the group-V incorporation rates and Bi droplet accumulation rate decrease with growth temperature while the desorption rates increase. The results indicate thermally-activated behavior for the Bi desorption, incorporation, and droplet accumulation rates, consistent with literature.[38-40] The characteristic temperature of Bi self-desorption is approximately twice as large as that of the Bi incorporation rate, which in turn is approximately twice as large as that of the droplet accumulation rate. The result is that Bi mole fraction increases quickly as growth temperature is lowered, consistent with experimental growth of dilute bismide alloys including InAsSbBi,[1,2] InAsBi,[27] GaAsBi[36,38,40], and GaSbBi.[35,50]. However the rate of Bi droplet accumulation increases greatly with reduction in growth temperature and is expected to dominate growth at low temperatures and excess As/In flux ratios.

Rates of desorption are observed to decrease from Bi to Sb to As at both 400 °C and 420 °C. Likewise, rates of incorporation are observed to increase from Bi to Sb to As at both growth temperatures. This trend is consistent with lean group-V molecular beam epitaxy growth of InAs and InAsSb on GaSb substrates in which nearly all incident As is experimentally observed to incorporate, while a smaller but still substantial portion of

incident Sb flux incorporates.[1,2,5] This trend is also consistent with the theoretically predicted decrease in solid solubility[37] with increasing atomic size from As to Sb to Bi.

The As-assisted removal mechanism is seen to play a dominant role in Bi desorption, evident from the high probability $P_{rem,As}$ of removal by excess As flux. With relatively high As flux and high probability of Bi removal, the As-assisted removal mechanism is primarily responsible for reduction of excess surface Bi. Additionally, As is observed to displace Bi from the crystal termination layer with high probability $P_{exc,As}$. By contrast the probabilities of Sb-assisted removal and exchange mechanisms are small. Therefore the Sb flux has little effect on the Bi surface coverage and Bi mole fraction.

The As- and Bi-assisted removal mechanisms $P_{rem,As}$ and $P_{rem,Bi}$ are observed to have a moderate effect on the removal of Sb from the surface layer. In contrast the results indicate that Sb and Bi do not assist in the removal of As from the surface layer or exchange with As in the crystal termination layer. This is consistent with growth observations that variations in As flux can strongly influence Bi and Sb mole fractions, however variations in Bi and Sb fluxes have little or no influence on As mole fractions.

Fig. 9 shows the measured and modeled Bi, Sb, and As mole fractions as circles and squares respectively. Solid symbols indicate specular droplet-free samples while open symbols are rough droplet-covered samples. Error bars on the measured group-V mole fractions are the uncertainties σ_i as reported in Table 4. The measured Bi mole fractions range from 0.12% for 210 nm thick bulk InAsSbBi grown at 420 °C (sample M) to 1.86% for a 10 nm thick InAsSbBi quantum well (sample E) grown at 400 °C. The model predicted Bi mole fractions agree to within +31/-24% relative error of the measured mole fraction for 400 °C growth and to within +61/-56% relative error for 420 °C growth. The

model predicted Sb mole fractions agree to within +17/-10% relative error and the model predicted As mole fractions agree to within +2/-3% relative error. The model predicted total group-V mole fraction (which is expected to sum to unity) is 100 +2.1/-2.3%. The model accurately replicates the measured Bi mole fractions to within one standard deviation $\sigma_{Bi,i}$ of uncertainty for each InAsSbBi sample.

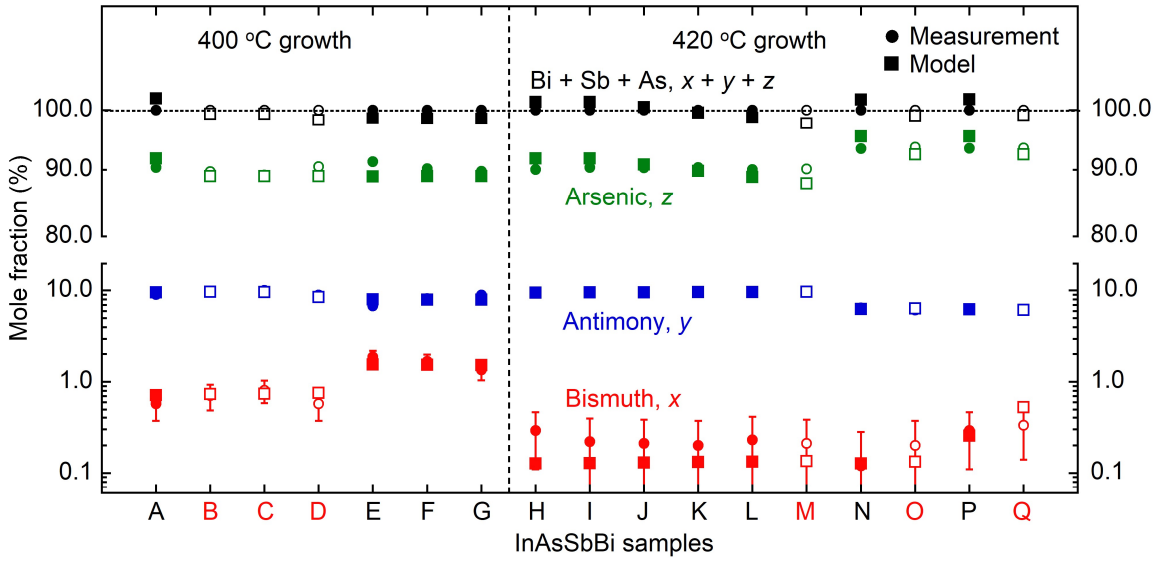

FIG. 9. Measured (circles) and model predicted (squares) bismuth (red), antimony (blue), arsenic (green), and total (black) mole fractions for the 400 °C and 420 °C grown InAsSbBi sample set. Solid symbols indicate specular droplet-free samples while open symbols indicate droplet-covered samples. Error bars on measured mole fractions are the uncertainties reported in Table 4.

Fig. 10 shows the Bi, Sb, and As surface coverage fractions in steady state predicted by the model. The solid circles indicate droplet-free specular samples and the open circles indicate droplet-covered rough samples. The total group-V surface coverage fraction

indicated by the black symbols ranges between 90% and 110%, or the tolerance bounds on the unity surface coverage constraint $\theta_{Bi} + \theta_{Sb} + As = 1$ employed in the fitting routine. The surface coverage fractions are not measurable *ex-situ* and are very challenging to measure *in-situ*, but regardless the model prediction offers important insights for molecular beam epitaxy growth of bismide alloys. The surface coverage is approximately proportional to the Bi/In, Sb/In, and As/In flux ratio for all samples. The steady state Bi surface coverage fraction is slightly reduced for droplet covered samples where the droplet accumulation rate R_{dro} reduces the surface coverage. A trend of increasing Bi surface coverage with decreasing As flux is observed in the 420 °C grown bulk sample series H – M, confirming the dominant role of As flux in desorbing Bi from the growth surface. The model predicts that Bi desorption, incorporation, droplet accumulation, and As- and Sb-assisted removal will all act to deplete the surface reservoir of Bi. The As-assisted exchange rate $F_{As}P_{exc,As}$ serves to replenish the Bi surface reservoir from Bi atoms in the crystal termination layer, however the net effect is a reduction in the Bi surface coverage due to the much greater contribution from the incorporation, desorption, droplet accumulation, and As-assisted removal mechanisms.

Interestingly, As is predicted to occupy the largest fraction of the surface layer, with Sb and Bi occupying roughly comparable fractions of 10 – 20%. This is consistent with RHEED patterns which indicate As-terminated (2×4) surface reconstructions for growth of InAs which transitions to an Sb-terminated (2×3) reconstruction for growth of InAsSb, then back to an As-like (2×4) or (2×1) surface reconstruction when Bi flux is introduced during growth of InAsSbBi.[1,27] In all three cases the surface reconstruction is dominated by the presence of a comparatively large amount of As on the adsorbed surface layer.

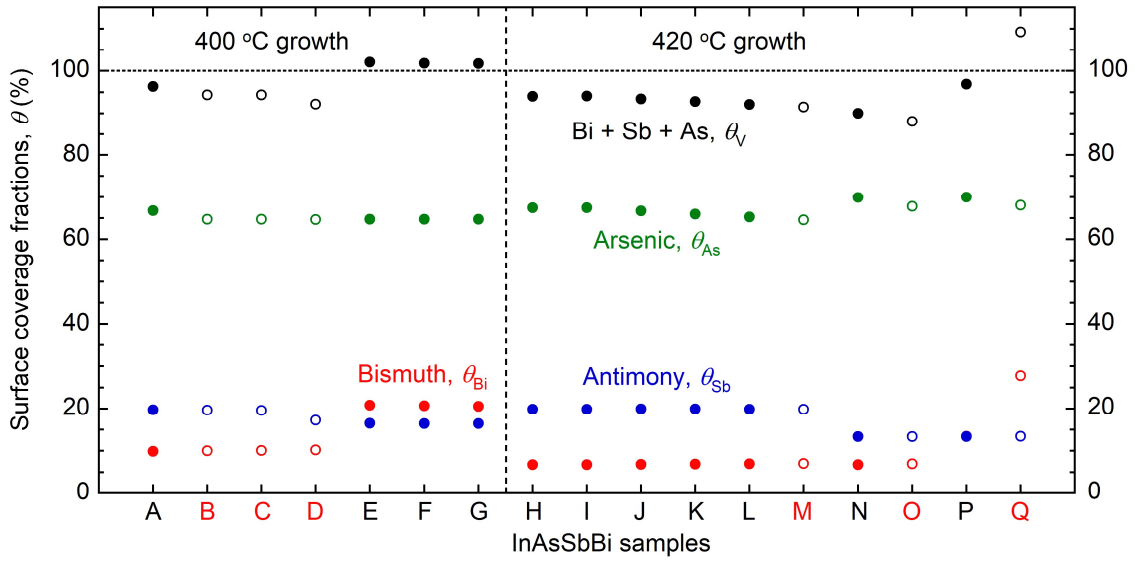

FIG. 10. Model predicted bismuth (red), antimony (blue), arsenic (green), and total group-V (black) surface coverage fractions for 400 °C and 420 °C grown InAsSbBi sample set. The solid circles indicate specular droplet-free samples and the open circles indicate droplet-covered samples.

The model predicted dependence of the Bi and Sb mole fractions on the As/In flux ratio is illustrated in Fig. 11 for growth at 400 °C and 420 °C. The excess As/In flux is directly proportional to the As/In flux ratio and is shown on the upper x-axis. Typical Bi/In flux ratios of 0.10 and 0.05 are shown. The Bi mole fraction is directly proportional to the Bi/In flux ratio and decreases with increasing As flux in all cases, however the reduction in mole fraction with excess As flux in is greater than the reduction with absolute As flux. This is a consequence of the high probability of As-assisted removal by excess As flux which directly reduces the Bi surface coverage. In contrast, the As-assisted exchange by the absolute As flux has a smaller and less direct effect on Bi surface coverage and thus

incorporation. Sb mole fraction, given as $\hat{y} = 1 - \hat{x} - \hat{z}$, is reduced to zero as As/In flux ratio increases to 1.002 and 1.022 for 400 °C and 420 °C growth respectively. This is due to the increasing As mole fraction $\hat{z}$ which is linearly proportional to the As/In flux in the growth model.

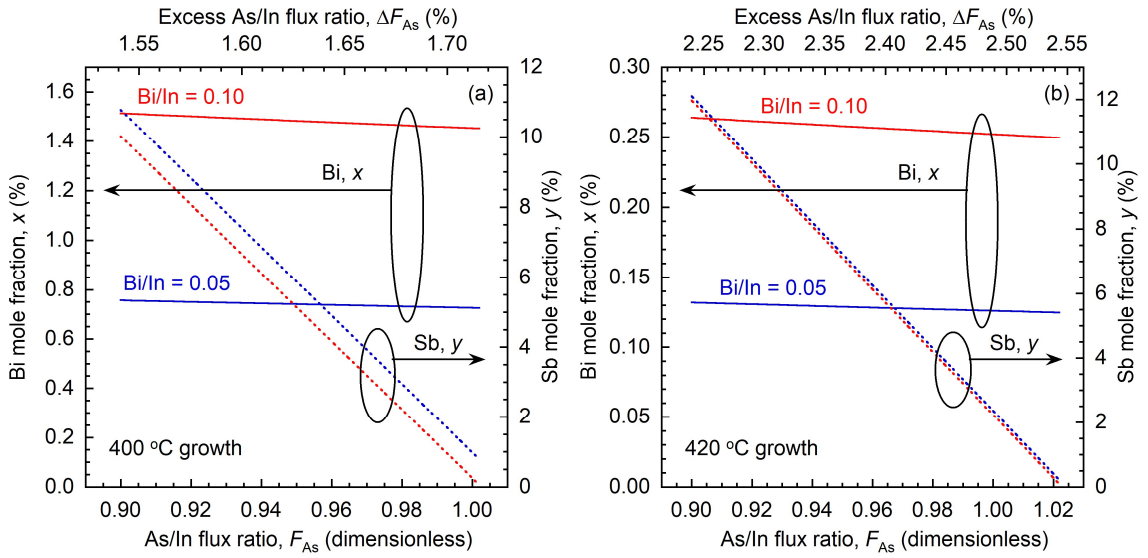

FIG. 11. Model predicted Bi mole fraction (solid lines) and Sb mole fraction (dashed lines) as a function of As/In flux ratio for (a) 400 °C growth and (b) 420 °C growth. Excess As/In flux is shown on upper x-axis. Bi/In flux ratios of 0.05 (blue lines) and 0.10 (red lines) are shown.

The steady state growth model embodied by Eqs. 10-11 can be used to specify the molecular beam epitaxy growth conditions to grow bulk InAsSbBi with a desired composition. The system of three equations for Bi, Sb, and As is invertible meaning that the Bi/In, Sb/In, and As/In flux ratios can be calculated for a given InAsSbBi composition x, y, and z. Furthermore the system of equations is one-to-one meaning that a single set

of flux ratios exists for a given InAsSbBi composition. Vegard's Law yields the relation between the Bi mole fraction x and Sb mole fraction y for InAsSbBi grown on GaSb substrates with in-plane biaxial strain of ε_{xx} in Eq. 7 above.

Fig. 12 shows the As/In, Sb/In, and Bi/In flux ratios as a function of Bi mole fraction for growth of InAsSbBi on GaSb substrates. Solid black lines on Fig. 12 are contours of constant biaxial strain ranging from lattice matched to 0.25% compressive or tensile strain. The rightmost boundary contour corresponds to unity total group-V surface coverage $\theta_{Bi} + \theta_{Sb} + \theta_{As} = \theta_V = 1$. When interpreted as the fraction of the growth surface covered by adsorbed Bi, Sb, and As, the total surface coverage can range only between zero and one. Attempting to increase the surface coverage above unity will not result in an increase in an increase of group-V incorporation as the surface is already completely covered. The flux ratios for the measured samples from Table 3 are shown on Fig. 12 as data points, with droplet-free specular samples indicated by solid circles and droplet-covered samples indicated by open circles.

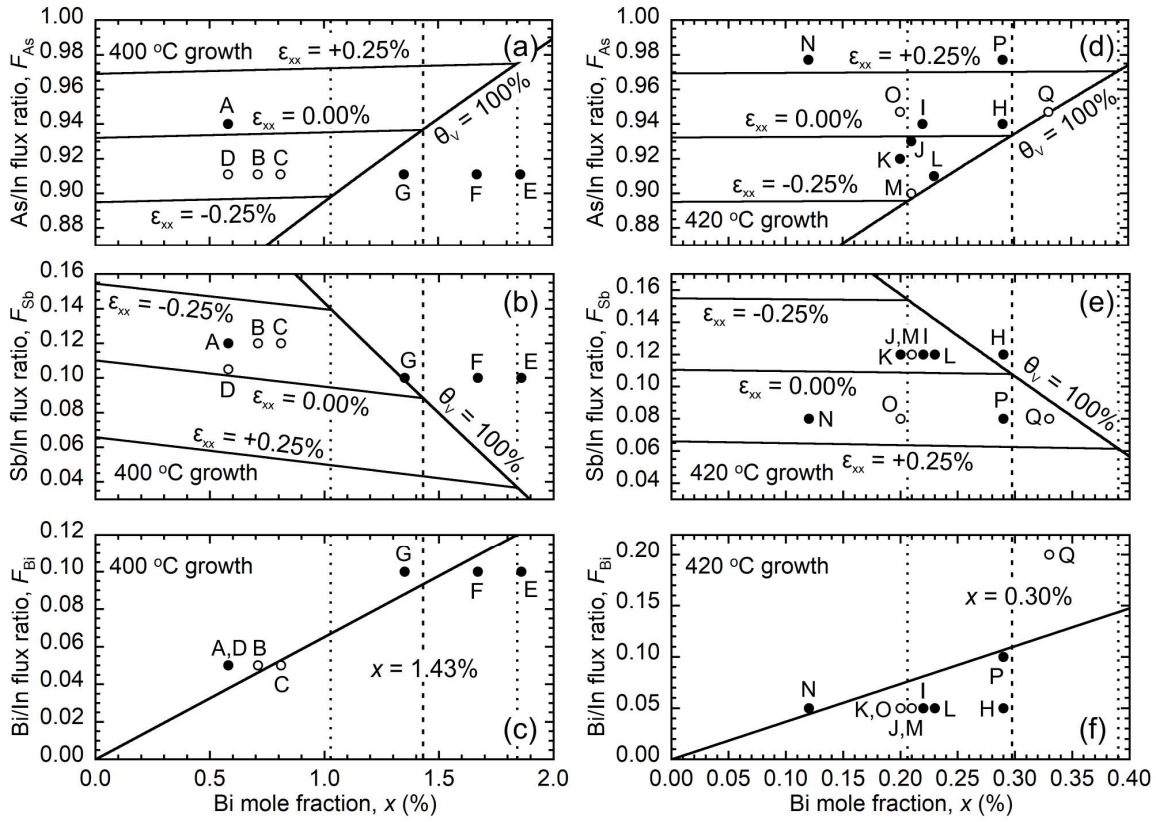

FIG. 12. Group-V flux ratios for the growth of InAsSbBi on GaSb as a function of Bi mole fraction, for 400 °C growths in left hand plots and 420 °C growths in right hand plots. The black lines are contours of constant in-plane biaxial strain ε_{xx} = 0.00%, -0.25%, and +0.25%. The dashed vertical lines indicate the ultimate Bi mole fractions for lattice-matched growth with ε_{xx} = 0.00%; dotted vertical lines indicate the Bi mole fractions for strained growth with ε_{xx} = -0.25% and +0.25%. The measured flux ratios provided in Table 3 are shown as solid circles for droplet-free specular surfaces and by open circles for droplet-covered samples. (a) and (d) As/In flux ratios, (b) and (e) Sb/In flux ratios, and (c) and (f) Bi/In flux ratios.

The vertical dashed lines indicate the Bi mole fraction corresponding to unity total group-V surface coverage for lattice matched InAsSbBi. This mole fraction is 1.43% and 0.30% for growth at 400°C and 420 °C respectively. Bi mole fraction is linearly proportional to the Bi surface coverage, and thus maximum Bi mole fraction is supported by the largest achievable Bi surface coverage fraction θ_{Bi}. Increasing Bi flux further will result in total group-V surface coverage increasing above unity and consequently no further Bi incorporation will occur, while increasing As flux will deplete the Bi surface coverage and thereby reduce Bi mole fraction. The results suggest that the mole fractions 1.43% and 0.30% are the ultimate limits for growth of InAsSbBi lattice matched to GaSb at 400 °C and 420 °C respectively. However, larger Bi mole fractions are achievable for tensilely strained material with smaller Sb mole fraction and consequently smaller Sb surface coverage fraction which provides additional scope for the accumulation of Bi in the surface layer. The three quantum well samples E, F, and G are observed to lie outside the unity group-V surface coverage boundary. This is a consequence of the quasi steady-state growth conditions of the quantum well samples. Continued growth under these flux ratios is expected to result in the formation of Bi-rich droplets which would reduce the Bi surface coverage fraction θ_{Bi} and push the total group-V surface coverage back within the boundary.

Of particular interest to materials designers are the conditions for droplet-free growth of InAsSbBi. The presence of Bi- and In-rich surface droplets is generally considered detrimental to the physical and optical quality of the material.[27,34,35,48] Fig. 13 illustrates the excess As/In flux ratio as a function of growth temperature for the experimental data. The growths are performed on ¼ 50 mm wafers which are sufficiently small that the radial

dependence of V/In flux ratio is negligible.[27] The data indicate that surface droplets form when excess As flux is below 2.0% and 1.2% at 400 °C and 420 °C respectively. This yields an equation of a line describing the excess As flux threshold for droplet formation as a function of growth temperature, indicated by the dashed line on Fig. 13:

$$\Delta F_{As}(T) = 18 - 0.04T\ (\%) \tag{17}$$

Growth with excess As flux below this threshold is expected to result in the formation of surface droplets. The model suggests that excess As plays a crucial role in the removal of excess unincorporated Bi from the growth surface. Excess unincorporated As co-desorbs with Bi carrying it away as an As-Bi molecule. When insufficient excess As flux is present to co-desorb unincorporated Bi, it begins to accumulate in Bi-rich droplet features due to the comparatively low rates of Bi incorporation and self-desorption.

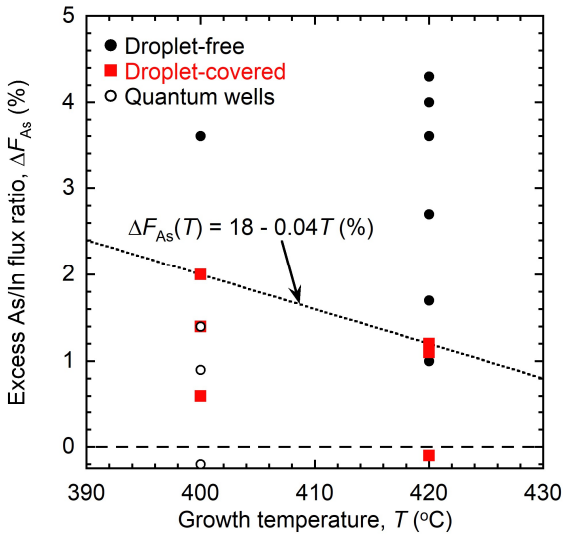

FIG. 13. Excess As/In flux ratio as a function of growth temperature. Data points indicate droplet-free bulk samples (black circles), droplet-covered bulk samples (red squares), and the droplet-free quantum well samples (open circles). The excess As flux threshold for droplet formation is shown by a dashed line and equation. Growth of InAsSbBi with excess As flux below this threshold is expected to result in Bi-rich surface droplet formation.

The growth model is extended to lower and higher growth temperatures by assuming an exponential temperature dependence in the Bi, Sb and As incorporation rates with a characteristic temperature of T_{inc}. This is consistent with the experimentally observed exponential temperature dependence of the Bi incorporation coefficient.[1] Since the incorporation rate R_{inc} is closely related to the incorporation coefficient, it is assumed to have the same temperature dependence with

$$R_{inc}(T) = R_{inc}(400)e^{-\frac{(T-400)}{T_{inc}}}. \quad (18)$$

The Bi self-desorption rate R_{des} is also observed to be a strong function of growth temperature and is assumed to have a similar form as the Bi incorporation rate, except with the opposite sign, resulting in

$$R_{des}(T) = R_{des}(400)e^{\frac{(T-400)}{T_{des}}}. \quad (19)$$

Which provides a characteristic temperature for the self-desorption process. The characteristic temperatures for incorporation T_{inc} = 14.88 °C, 1325 °C, and 1986 °C and desorption T_{des} = 36.76 °C, 577.3 °C, and 53.79 °C for Bi, Sb, and As respectively are determined from the 400 °C and 420 °C parameters at in Table 8. The characteristic temperatures generally decrease with atomic number. All probabilities of anion-assisted removal and exchange are assumed to be independent of growth temperature.

The ultimate Bi mole fraction limit illustrated in Fig. 12 and corresponding Bi/In, Sb/In, and As/In flux ratios for InAsSbBi lattice matched to GaSb is plotted as a function of growth temperature in Fig. 14. The figure corresponds to growth with unity total group V surface coverage. The Bi mole fraction decays approximately exponentially with growth temperature with a characteristic temperature of 12.88 °C. The Bi mole fraction limit decreases with growth temperature from 3.66% at 390 °C to 0.14% at 430 °C. The required Bi/In flux ratio increases from 0.102 at 390 °C to 0.125 at 430 °C. The growth model indicates that the growth temperature must be reduced to 384.9 °C or lower to obtain the lattice matched ternary alloy $InAs_{0.932}Bi_{0.068}$ on GaSb, and that increases in growth temperature strongly reduce the Bi incorporation coefficient.

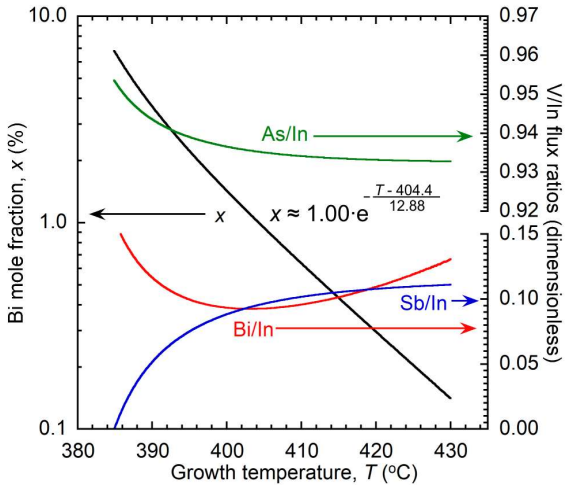

FIG. 14. Ultimate Bi mole fraction limit (black curve) and corresponding Bi/In (red curve), Sb/In (blue curve), and As/In (green curve) flux ratios as a function of growth temperature for InAsSbBi lattice matched to GaSb. The Bi mole fraction decays approximately exponentially with growth temperature with a characteristic temperature of 12.88 K as shown by the fit equation.

The growth model is fully generalizable to other dilute bismide alloys including GaSbBi, InAsBi, GaAsBi, and GaAsSbBi, among others. However it is important to note that the growth model presented in this work is linear with respect to the V/In flux ratios; i.e. the growth model parameters do not vary with flux. The assumption that the growth model parameters are independent of the flux values is applicable only to the near-unity group-V/In flux ratio regime. For example, if large As/In flux ratios greater than approximately 1.017 at 400 °C or 1.026 at 420 °C are used, then the As desorption rate must increase or the incorporation rate must decrease (or both) to maintain As mole fraction below unity. Similar nonlinearities will exist for the Bi and Sb growth model parameters. The linear growth model is nevertheless a powerful tool for predicting growth outcomes as

this relatively narrow growth window of group-V flux ratios must be employed to incorporate appreciable Bi mole fractions.[1,27]

3: OPTICAL PROPERTIES OF III-V SEMICONDUCTORS

The key parameters by which a semiconductor material's performance is assessed include its absorption spectrum, optical constants, and quantum efficiency, among others. These parameters are all ultimately traceable to the material's electronic band structure and the presence of various defects in the crystal lattice. Band structure and defect type and density are functions of chemical composition and crystal structure, which in turn are strongly influenced by material growth conditions. In this chapter an extensive study of the optical properties of III-V semiconductors is presented, beginning with an elementary treatment of absorption in binary III-V compounds, progressing to analysis of carrier recombination in the ternary alloy InAsSb, and finally concluding with discussion of photoluminescence measurements of the quaternary alloy InAsSbBi.

3.1 Optical Absorption Edge in III-V Semiconductors

The fundamental bandgap energy of a semiconductor is defined as the energy separation between the continuum valence band maximum and continuum conduction band minimum. This definition is precise in the absence of defect or tail states that cause sub-bandgap absorption. The unavoidable presence of these localized states results in a degree of ambiguity about the determination of the bandgap energy. The bandgap energy of bulk semiconductors is at times identified as the energy at which the first derivative of the absorption coefficient α, extinction coefficient k, or imaginary part of the dielectric function ε_2 attains its maximum value.[4,5,41,42] This so-called first derivative maximum method approximates the energy at which the joint optical density of states increases at the greatest rate.[5,41] For direct-bandgap bulk semiconductors this corresponds to the onset of

optical transitions involving the edges of valence and conduction band continuum states once the photon energy equals or exceeds the fundamental bandgap energy. The first derivative maximum method is also used to identify the ground state transition energy for quantum-confined structures such as quantum wells or superlattices.[41] Nevertheless, the first derivative maximum provides little insight into the shape of the absorption edge that can be strongly influenced by the Coulomb interaction[51] between the electrons and holes and the presence of localized states near the continuum band edges. These effects influence the fundamental bandgap energy as defined by the energy separation of the continuum band edges.

In its textbook form, the optical absorption spectrum of a semiconductor is expressed as a product of the joint optical density of states $\rho(h\nu)$ ($cm^{-3}\cdot eV^{-1}$) and a transition strength $S(h\nu)$ ($cm^2\cdot eV$) with[15,58]

$$\alpha(h\nu) = \rho(h\nu) \cdot S(h\nu)\,. \tag{20}$$

The joint optical density of states depends on the electron and hole density of states, which are determined by the band structure in the vicinity of the fundamental bandgap. For direct-gap semiconductors, such as III-V binaries, electrons and holes have approximately parabolic band dispersion near the band edges.[15] The corresponding joint optical density of states[15] exhibits a square root dependence on photon energy $h\nu$, with

$$\rho(h\nu) = \frac{8\sqrt{2}\pi}{h^3}\left(m_e \frac{m_c m_v}{m_c + m_v}\right)^{3/2} \sqrt{h\nu - E_g}\,. \tag{21}$$

where m_e is the free electron mass, and m_c and m_v are the dimensionless effective masses of the conduction band electrons and valence band holes, respectively.[15] In the absence of strain the light hole and heavy hole bands are degenerate at the Γ point, and the joint optical

density of states is dominated by the smaller electron effective mass. Here $\rho(h\nu)$ is the density of states in the absence of band filling effects, such as the Moss-Burstein shift and bandgap renormalization.[51] These effects are negligible for measurements where the photoexcited carrier concentration is well below degeneracy.

The transition strength in Eq. 20 can be expressed in terms of a dimensionless transition strength[15,52] $S_0(h\nu)$ with

$$S(h\nu) = \frac{he^2}{4c\varepsilon_0 m_e n(h\nu)} S_0(h\nu)\,, \tag{22}$$

where h is Planck's constant, c is the speed of light, ε_0 is the vacuum permittivity, e is the electron charge, and $n(h\nu)$ is the refractive index that typically has a weak dependence on photon energy. The absorption coefficient changes by orders of magnitude in the vicinity of the band edge of the materials considered in this work, while the refractive index changes by less than 2% and as such is assumed to be an average constant value.

The transition strength S_0 describes the probability of a given optical transition and is described by the optical perturbation to the crystal Hamiltonian due to the presence of light. According to Fermi's golden rule[15] the rate of optical transitions is proportional to the perturbed Hamiltonian matrix element for interband transitions. In the long-wavelength dipole approximation where the wavelength of the perturbing optical field is much greater than the unit cell, the transition strength associated with this matrix element is equivalently related to either the momentum matrix element $\langle\psi_h|\boldsymbol{p}|\psi_e\rangle$ or dipole matrix element $\langle\psi_h|\boldsymbol{r}|\psi_e\rangle$ as[41]

$$S_0 = \left(\frac{2}{m_e}\right)\frac{|\langle\psi_h|\boldsymbol{p}|\psi_e\rangle|^2}{h\nu} = \left(\frac{8\pi^2 m_e}{h^2}\right)|\langle\psi_h|\boldsymbol{r}|\psi_e\rangle|^2 h\nu$$
$$= \frac{4\pi}{h}\sqrt{|\langle\psi_h|\boldsymbol{p}|\psi_e\rangle|^2 \cdot |\langle\psi_h|\boldsymbol{r}|\psi_e\rangle|^2}\,. \tag{23}$$

In practice, either the momentum matrix element, dipole matrix element, or transition strength is assumed to be a constant that is independent of photon energy[15,53,54] in much of the analyses performed in the literature. The assumption that any one of these three is constant assumes an energy dependence for the other two. Using Eqs. 20 through 23 the absorption coefficient is expressed in terms of the momentum matrix element $\langle\psi_h|\boldsymbol{p}|\psi_e\rangle$ in Eq. 24a, the dipole matrix element $\langle\psi_h|\boldsymbol{r}|\psi_e\rangle$ in Eq. 24b, and the product of the two in Eq. 24c.

$$\alpha(h\nu) = \frac{4\sqrt{2}\pi e^2}{nc\varepsilon_0 h^2\sqrt{m_e}}\left(\frac{m_c m_v}{m_c + m_v}\right)^{3/2}|\langle\psi_h|\boldsymbol{p}|\psi_e\rangle|^2 \cdot \left(h\nu - E_g\right)^{1/2}(h\nu)^{-1} \tag{24a}$$

$$\alpha(h\nu) = \frac{16\sqrt{2}\pi^3 e^2 {m_e}^{3/2}}{nc\varepsilon_0 h^4}\left(\frac{m_c m_v}{m_c + m_v}\right)^{3/2}|\langle\psi_h|\boldsymbol{r}|\psi_e\rangle|^2 \cdot \left(h\nu - E_g\right)^{1/2} h\nu \tag{24b}$$

$$\alpha(h\nu) = \frac{8\sqrt{2}\pi^2 e^2\sqrt{m_e}}{nc\varepsilon_0 h^3}\left(\frac{m_c m_v}{m_c + m_v}\right)^{3/2}\sqrt{|\langle\psi_h|\boldsymbol{p}|\psi_e\rangle|^2 \cdot |\langle\psi_h|\boldsymbol{r}|\psi_e\rangle|^2} \cdot \left(h\nu - E_g\right)^{1/2} \tag{24c}$$

By writing the equations in this form, the photon energy dependence of each of the three assumptions is explicitly shown. In addition to the square root density states term, the constant momentum matrix element approximation results in a one over energy term, the constant dipole matrix element results in a linear energy term, and the constant transition strength approximation has no additional energy dependent term. The choice of which is taken to be constant influences the interpretation of the behavior of the absorption coefficient above the bandgap energy.

This treatment of the absorption edge considers only the continuum states involved in transitions at and above the fundamental bandgap energy and does not account for free exciton absorption,[14,51] the Coulomb enhancement of absorption near the bandgap,[16,51] or the broadening effects of thermal and frozen in crystal lattice disorder. Even high-quality materials exhibit an Urbach absorption edge[10-13] that is mainly due to the electron-phonon interaction. Excitonic absorption is a significant effect in high purity material, particularly at low temperatures, and results in absorption peaks below the bandgap energy.[14,16,55]

Furthermore, the Coulomb interaction between free electrons and holes results in an enhancement of absorption near the bandgap that is dependent on the free exciton binding energy[16,51,55] that typically scales with bandgap energy in the III-Vs. The Coulomb interaction is a multi-particle phenomenon involving both an electron and hole and as such cannot be treated within the free electron band structure framework, but rather requires the addition of the electron-hole Coulomb potential to the crystal Hamiltonian.[56] Thus the Coulomb interaction can modify both the density of states and the transition strength. The effect of the Coulomb interaction is large near the bandgap energy and asymptotically approaches unity at energies above the bandgap energy, which has been quantified by an enhancement factor[14,51] described as

$$F(h\nu) = \frac{2\pi\sqrt{\frac{E_{ex}}{h\nu - E_g}}}{1 - e^{-2\pi\sqrt{\frac{E_{ex}}{h\nu - E_g}}}}. \tag{25}$$

The exciton binding energy E_{ex} scales with bandgap energy and is experimentally determined as 4.0 meV for GaAs[16], 2.1 meV for GaSb[51], 1.0 meV for InAs[57], and 0.4 meV

for InSb.[58] As such, the Coulomb enhancement of absorption is expected to increase with bandgap energy.

A model is developed that evaluates the onset of absorption at the fundamental bandgap and that encompasses the asymptotic behaviors of the absorption coefficient above and below the bandgap. The model is shown in Eq. 26 and contains 5 parameters: the bandgap energy E_g, determined by the behavior of the absorption coefficient above bandgap; the characteristic Urbach energy E_u, based on the slope of the absorption tail below the bandgap; the magnitude of the absorption coefficient at the bandgap energy α_g; and the power law dependence $p(h\nu)$ of the absorption coefficient above the bandgap that is comprised of a constant term p_g that describes the power law at the bandgap and a photon energy $h\nu$ dependent term that describes the variation in the power law above the bandgap with characteristic energy, E_m.

$$\alpha(h\nu) = \alpha_g \left[\frac{ln\left(1 + e^{(h\nu - E_g)/pE_u}\right)}{\ln 2}\right]^p \tag{26a}$$

$$p(h\nu) = p_g + \frac{h\nu - E_g}{E_m} \tag{26b}$$

For energies above the bandgap, $h\nu > E_g$, the asymptotic behavior reflects optical absorption involving continuum states and is specified as a power law with

$$\alpha(h\nu) = \alpha_g \left(\frac{h\nu - E_g}{\ln(2) \cdot p(h\nu) \cdot E_u}\right)^{p(h\nu)} . \tag{27}$$

For energies below the bandgap, $h\nu \leq E_g$, the asymptotic behavior reflects optical absorption involving localized tail states specified by an exponential Urbach tail with

$$\alpha(h\nu) = \alpha_g (\ln 2)^{-p(h\nu)} e^{(h\nu - E_g)/E_u} \cong \alpha_g (\ln 2)^{-p_g} e^{(h\nu - E_g)/E_u} , \tag{28}$$

where the right-hand approximation is valid for abrupt absorption edges, with $E_u \ll E_m$.

Examining the absorption coefficient in terms of these model parameters provides insight into the optical joint density of states, the optical transition strength, and Coulomb enhancement of the optical transition strength. As an example, the parabolic single-electron band model predicts a square root density of states with power law one half and an Urbach tail width that approaches zero. The model in Eq. 26 does not describe bound exciton absorption peaks when present in the data, which would be modeled by an additional function.

The model is shown in Fig. 15, where it is plotted in terms of normalized absorption coefficient $\left(\alpha/\alpha_g\right)(\ln 2)^p$ as a function of normalized energy $\left(h\nu - E_g\right)/E_u$. Two cases are illustrated: i) for a square root density of states and a constant transition strength, where the power law is a constant one half with p_g = 1/2 and $1/E_m$ = 0, and ii) for a strong Coulomb interaction, where the power law is small with p_g = 1/5 and $E_m = 2E_g$. The normalization $\left(\alpha/\alpha_g\right)(\ln 2)^p$ is selected such that the Urbach tail asymptotes of the two curves coincide. The power law p_g, which is related to the optical density of states and the influence of the Coulomb interaction, dictates the sharpness of the absorption turn-on at the bandgap energy. The characteristic energy E_m is related to the energy dependence of the optical transition strength (matrix element) and the decay in the strength of Coulomb interaction for optical transitions at photon energies above the bandgap.

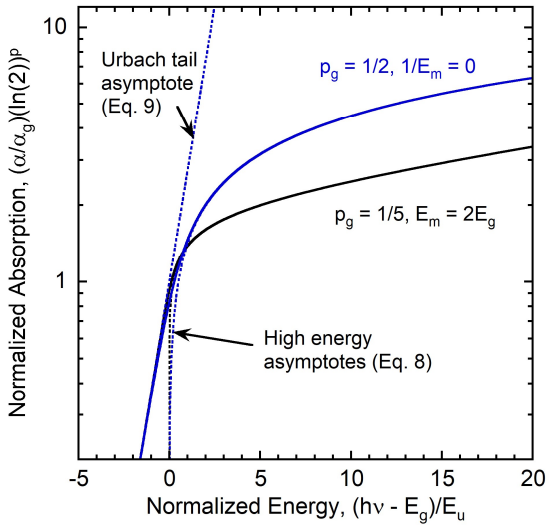

FIG. 15. Normalized absorption coefficient model with $(\alpha/\alpha_g)(\ln 2)^p$ as a function of normalized energy $(h\nu - E_g)/E_u$. Dashed lines show the low and high energy asymptotic expressions, Eqs. 27 and 28 respectively.

Although knowledge of the absorption coefficient at the bandgap energy is useful, it does not fully describe the overall magnitude of the absorption near the bandgap that is strongly influenced by the Coulomb interaction in addition to the density of states. For instance, the effective cutoff wavelength of a photodetector is typically shorter than the bandgap wavelength, as thin film materials can be transparent right at the bandgap. Therefore a better figure of merit for comparing the optical absorption strength of different materials for device applications is the "knee" of the absorption spectrum when viewed on a log scale, which identifies the magnitude of the absorption coefficient as it rolls over above the bandgap. The position of the absorption spectrum knee E_k is specified by the energy where the radius of curvature r_a of the absorption spectrum has a minimum value $r_k = \min_{h\nu} r_a$, with[59]

$$r_a = \left| \frac{\left(x'^2 + y'^2\right)^{3/2}}{x'y'' - y'x''} \right| = \left| \frac{a\left(\left(\frac{1}{a}\right)^2 + \left(\frac{1}{\alpha(h\nu)}\frac{d\alpha}{dh\nu}\right)^2\right)^{3/2}}{\frac{1}{\alpha(h\nu)}\frac{d^2\alpha}{dh\nu^2} - \left(\frac{1}{\alpha(h\nu)}\frac{d\alpha}{dh\nu}\right)^2} \right|. \quad (29)$$

Here $x = h\nu/a$ and $y = ln(\alpha(h\nu)/b)$ are the dimensionless energy and absorption coefficient normalized by the constants a with units of energy and b with units of inverse length. The parameter b does not appear in Eq. 27 as the derivatives of y are independent of the vertical scale when the absorption coefficient is observed on a log scale. The parameter a scales the horizontal energy axis to the energy range of interest, as the range selected affects the observed energy position of the knee. The first and second derivatives are $x' = 1/a$, $y' = \alpha'/\alpha$, $x'' = 0$, and $y'' = \alpha''/\alpha - (\alpha'/\alpha)^2$. The radius of curvature of $\ln\big(\alpha(h\nu)\big)$ exhibits a single well-defined minimum that is observed above the bandgap energy E_g, thus defining the position E_k and amplitude α_k of the knee in the absorption spectrum.

The absorption edge also manifests itself in the imaginary parts of the complex index of refraction, $\tilde{n} = n + ik$, and the complex dielectric function, $\tilde{\varepsilon} = \varepsilon_1 + i\varepsilon_2$, as is apparent in the following relationships between the optical constants.[15,60]

$$\alpha = \frac{4\pi k h\nu}{hc} \quad (30a)$$

$$\varepsilon_1 = n^2 - k^2 \quad (30b)$$

$$\varepsilon_2 = 2nk \quad (30c)$$

$$n^2 = \frac{1}{2}\left[\sqrt{\varepsilon_1^2 + \varepsilon_2^2} + \varepsilon_1\right] \quad (30d)$$

$$k^2 = \frac{1}{2}\left[\sqrt{\varepsilon_1^2 + \varepsilon_2^2} - \varepsilon_1\right] \tag{30e}$$

As such the absorption edge model in Eq. 26 is also suitable for examination of the extinction coefficient k and the imaginary dielectric coefficient ε_2.

The first derivative method of identifying bandgap energy finds the energy where the absorption edge increases at the greatest rate. Numerical calculation of the derivative at each data point is performed by the center-difference formula[61]

$$\frac{df[j]}{dh\nu[j]} = \frac{f[j+1] - f[j-1]}{h\nu[j+1] - h\nu[j-1]}. \tag{31}$$

Where f is the measured discrete data as a function of energy, which is either the absorption coefficient α, the extinction coefficient k, or the imaginary dielectric coefficient ε_2. If the energy spacing of the data is constant, the denominator $h\nu[j+1] - h\nu[j-1]$ may be replaced by $2\Delta h\nu$, where $\Delta h\nu$ is the constant energy spacing. The center-difference point-by-point derivative calculation does not shift of the maximum of the first derivative, unlike backward or forward difference formulas that shift the derivative by $\pm\ \Delta h\nu$, respectively.

The fundamental absorption-edge of semi-insulating GaAs and unintentionally doped GaSb, InAs, and InSb is investigated using spectroscopic ellipsometry. The measurements are performed on commercially available III-V wafers.[62] The material specifications for resistivity, Hall mobility, and carrier concentration supplied by the manufacture are summarized in Table 9. The carrier concentrations are well below the conduction and valence band effective density of states N_c and N_v at room temperature.[15] Therefore the material is not degenerate and band filling effects such as the Moss-Burstein shift are negligible. The absorption measurements are performed on three separate GaAs samples A, B, and C to assess the reproducibility of the measurement technique and modeling work.

TABLE 9. Physical and electrical characteristics of III-V substrates studied by ellipsometry. Values obtained from wafer datasheets.[62]

Material	Sample	Type	Thickness (μm)	Resistivity (Ω·cm)	Hall mobility ($cm^2V^{-1}s^{-1}$)	Carrier concentration (cm^{-3})
GaAs	A	Semi-insulating	500	2×10^{8}	5500	5×10^{6}
	B		350	2×10^{8}	5400	6×10^{6}
	C		350	2×10^{8}	5400	6×10^{6}
GaSb	-	Undoped (p-type)	500	7×10^{-2}	700	1×10^{17}
InAs	-	Undoped (n-type)	500	1×10^{-2}	2.5×10^{4}	2×10^{16}
InSb	-	Undoped (n-type)	640	6×10^{-2}	5.0×10^{5}	2×10^{14}

The spectroscopic ellipsometry measurements of GaAs and GaSb are performed using a J.A. Woollam VASE spectroscopic ellipsometer that covers 0.39 to 6.42 eV (193 to 3200 nm wavelength). Measurements of InAs and InSb are performed using a J.A. Woollam IR-VASE ellipsometer that covers 0.04 to 0.73 eV (1.7 to 30 μm). All measurements are performed at room temperature (297 K) using four incident angles (68°, 72°, 76°, and 80°) with a spectral resolution of 3.9 nm (6.3 meV for GaAs and 1.7 meV for GaSb) for the VASE measurements and 16 cm^{-1} (2.0 meV for InAs and InSb) for the IR-VASE measurements. Because the wafers are transparent below the bandgap energy, reflection from the backside of the wafer results in the collection of spurious depolarized light at the detector. Therefore, the wafer backsides are roughened sequentially with 320 and 400 grit sandpaper to diffusely scatter the backside reflections. After backside roughening, the depolarization is less than 2%.

The WVASE software[63] is used to obtain the optical constants of III-V wafers from the measured ellipsometry parameters Ψ and Δ. The ellipsometry optical model employs two layers, a surface oxide layer and the III-V layer. The thickness of the wafers ranges from 350 to 640 μm and is treated as infinite when analyzing ellipsometry data. This assumption

is justified as light that reaches the backside of the substrate is diffusely scattered. Optical constants of the oxide layers and the initial values of optical constants of the III-V substrates are provided by the WVASE software library. Since the optical constants for InSb oxide are not available, the InSb native oxide is modeled using the GaSb oxide optical constants. The best fit thickness of the oxide layers is shown in Table 10. The optical constants are determined using the wavelength-by-wavelength method of analysis, which provides the raw data that is not distorted by any mathematical modeling of the optical constants. The Kramers-Kronig consistency of the optical constants is verified by repeating the fits using a generalized oscillator (PSM0: Psemi-M0) model; the optical constants derived from the wavelength-by-wavelength fitting and generalized oscillator model agree to within less than 1% over the entire wavelength range.

TABLE 10. Oxide layer thickness for ellipsometry models of III-V wafers.

Material	GaAs			GaSb	InAs	InSb
Sample	A	B	C			
Oxide thickness (nm)	2.015	1.814	2.100	6.475	3.457	2.473

The measured absorption spectra for semi-insulating GaAs sample A and undoped GaSb, InAs, and InSb are presented in Fig. 16 as a function of photon energy less bandgap energy, which aligns the absorption edges for comparison. The absorption model in Eq. 26 (solid curve) is fit to the absorption data (solid circles). The fit range is from 140 meV above the bandgap down to an extinction coefficient of $k = \alpha hc/(4\pi h\nu) = 0.014$ below the bandgap, which is the sensitivity limit of the ellipsometric measurement. The least squares fit analysis assumes that the uncertainty in the value of each data point is

proportional to its value, which results in a proportionally weighted fit to the entire data set. The results are highly reproducible with a standard deviation of 0.2 meV in the measured bandgap energy for the three GaAs samples. The best fit values for parameters α_g, E_g, E_u, p_g, and E_m are summarized in Table 11, along with the absorption coefficient knee values E_k and α_k identified from the minimum of radius of curvature for $a = 0.100$ eV; see Eq. 27. The energy scaling parameter a is selected at 40% of the full-scale range of -0.05 to 0.20 eV in Fig. 16 to coincide with the visual roll-over point observed on this energy scale. The values in Table 11 are reported to the significant level of precision necessary to illustrate the reproducibility of the GaAs measurements and to accurately reproduce the model parameters and curves.

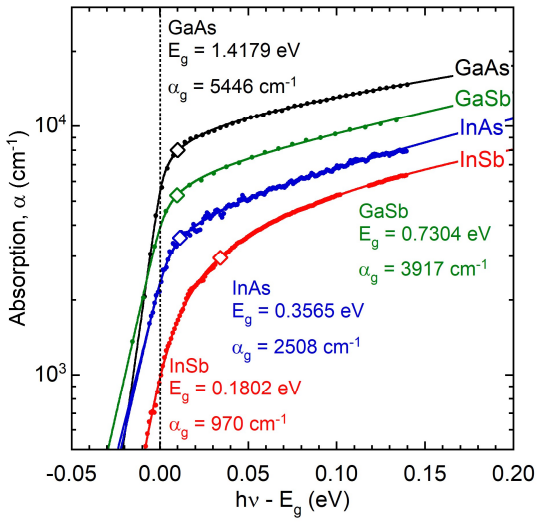

FIG. 16. Absorption coefficient α as a function of photon energy relative to the bandgap $h\nu - E_g$ for semi-insulating GaAs sample A and undoped GaSb, InAs, and InSb substrates. Measured data shown as solid circles. The solid lines are fits of the absorption model in Eq. 26 to the data. The best fit parameters for bandgap energy E_g and absorption coefficient α_g are shown for each curve. The position of the knee in the spectrum is indicated by the open diamonds.

TABLE 11. Best fit parameters for the absorption coefficient model (Eq. 26) and the absorption coefficient knee (Eq. 27) for semi-insulating GaAs, samples A, B, and C, and undoped GaSb, InAs, and InSb.

	GaAs			GaSb	InAs	InSb
	A	B	C			
α_g (cm^{-1})	5446	5427	5480	3917	2508	970
E_g (eV)	1.4179	1.4177	1.4183	0.7304	0.3565	0.1802
E_u (meV)	8.69	8.66	8.74	13.98	14.05	10.67
p_g	0.1580	0.1583	0.1584	0.1613	0.1929	0.4948
E_m (eV)	2.541	2.472	2.529	1.501	1.190	4.332
E_k (eV)	1.4279	1.4277	1.4283	0.7401	0.3677	0.2142
α_k (cm^{-1})	8014	7921	7990	5286	3568	2958

The optical constants n and k, and ε_1 and ε_2, are shown for the three semi-insulating GaAs samples in Fig. 17. The first derivative maxima of k and ε_2, and the maxima of the n and ε_1, are shown by vertical lines and indicated numerically. The location of the maxima is precisely determined by interpolating the data in the region of the peak with a Gaussian function, where the peak location is given by the best fit value. Detailed sensitivity analysis shows that the resulting precision of the discrete numerical calculation of the first derivative maximum is better than 0.02 meV.

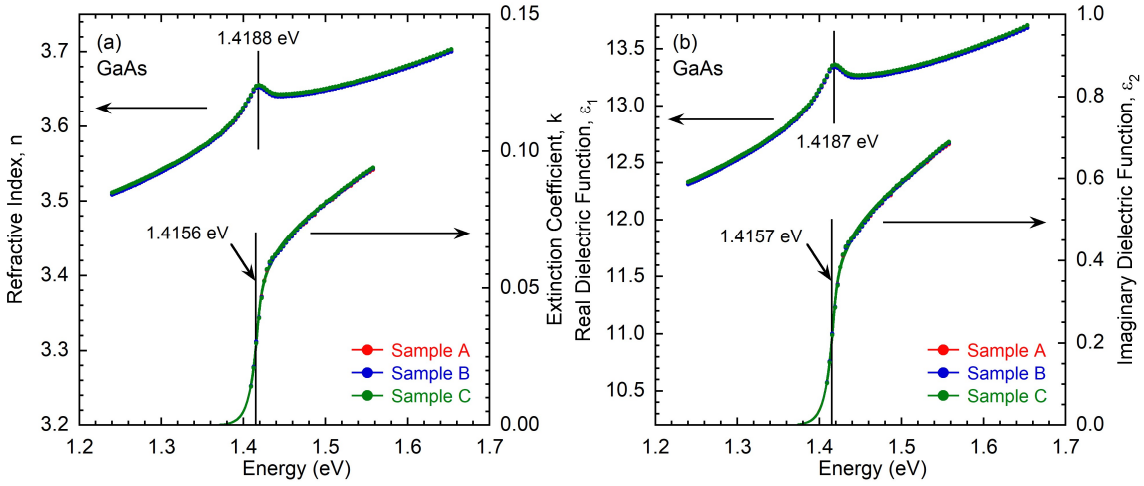

FIG. 17. (a) Complex index of refraction and (b) complex dielectric function for three different semi-insulating GaAs samples measured by spectroscopic ellipsometry. The peak value of the real parts n and ε_1, and the first derivative maximum of the imaginary parts k and ε_2, are indicated by vertical lines. The solid curves are fits of the model in Eq. 26 to the k and ε_2 data over the photon energy range 140 meV above the bandgap down to an extinction coefficient of k = 0.014 below the bandgap (1.4091 – 1.5579 eV).

The GaAs bandgap energy estimated by i) fitting the absorption model in Eq. 26 to α, k, and ε_2, ii) finding the first derivative maximum[4,5,41,42] of α, k, and ε_2, and iii) finding the peak values[64] of n and ε_1 are shown in Table 12. There is excellent agreement between the three GaAs samples with the average and standard deviation of the values of the three samples shown in the right-hand column.

TABLE 12. GaAs bandgap energy determined by first derivative maximum of extinction coefficient k, absorption coefficient α, and imaginary dielectric function ε_2. Also shown are bandgap energies determined from the maximum values of refractive index n and real dielectric function ε_1. The model parameters for α, k, and ε_2 are summarized for each GaAs sample in the lower portion of the table. The model fits are performed over the same photon energy range as in Fig. 16.

	Sample A (eV)	Sample B (eV)	Sample C (eV)	Average ± Standard Deviation (eV)
maximum of 1st derivative of ε_2	1.4157	1.4156	1.4158	1.4157 ± 0.00008
maximum of 1st derivative of k	1.4157	1.4156	1.4158	1.4157 ± 0.00008
maximum of 1st derivative of α	1.4156	1.4155	1.4157	1.4156 ± 0.00008
maximum of ε_1	1.4187	1.4186	1.4188	1.4187 ± 0.00012
maximum of n	1.4188	1.4186	1.4189	1.4188 ± 0.00012
absorption coefficient α fit to model	Sample A	Sample B	Sample C	Average ± Standard Deviation
Amplitude α_g (cm^{-1})	5446	5427	5480	5451 ± 22
E_g (eV)	1.4179	1.4177	1.4183	1.4180 ± 0.0002
E_u (meV)	8.69	8.66	8.74	8.70 ± 0.03
p_g	0.1580	0.1583	0.1584	0.1582 ± 0.0002
E_m (eV)	2.54	2.47	2.53	2.51 ± 0.03
extinction coefficient k fit to model	Sample A	Sample B	Sample C	Average ± Standard Deviation
Amplitude k_g	0.0383	0.0380	0.0384	0.0382 ± 0.0002
E_g (eV)	1.4181	1.4180	1.4183	1.4181 ± 0.0001
E_u (meV)	8.81	8.75	8.84	8.80 ± 0.04
p_g	0.1500	0.1507	0.1507	0.1505 ± 0.0003
E_m (eV)	3.91	3.76	3.89	3.85 ± 0.07
imaginary dielectric function ε_2 fit to model	Sample A	Sample B	Sample C	Average ± Standard Deviation
Amplitude $\varepsilon_{2,g}$	0.280	0.278	0.281	0.280 ± 0.001
E_g (eV)	0.14181	0.14180	0.14183	1.4181 ± 0.0001
E_u (meV)	8.79	8.72	8.82	8.78 ± 0.04
p_g	0.1478	0.1485	0.1485	0.1483 ± 0.0003
E_m (eV)	3.62	3.50	3.61	3.58 ± 0.06

Agreement is observed for the best fit model (Eq. 26) parameters for the bandgap energy E_g and the Urbach energy E_u obtained from the three optical constants α, k, and ε_2. Agreement is also observed for the first derivative maximum obtained from the three

optical constants α, k, and ε_2, although the first derivative maximum values are about 2 meV less than the bandgap value determined from the fit of the model to the data. The best fit power law p_g values are within 4% across the 3 sets of optical constants. The characteristic energy E_m is larger for the optical constants k and ε_2, indicating a weaker energy dependence above the bandgap compared to the absorption coefficient α, as indicated in the relations of Eq. 30 where k and ε_2 are proportional to $\alpha/h\nu$.

The absorption amplitude is observed to increase with bandgap energy and is analyzed at the bandgap energy using the product of the optical density of states, the transition strength, and the Coulomb enhancement factor in Eqs. 21, 22, and 25, where

$$\alpha_A = \lim_{h\nu \to E_g} \rho(h\nu) S(h\nu) F(h\nu) = \frac{4\sqrt{2}\pi^2 e^2 \sqrt{m_e}}{c\varepsilon_0 h^2} \cdot \sqrt{E_{ex}} \left(\frac{m_c m_v}{m_c + m_v}\right)^{3/2} \frac{S_0(E_g)}{n(E_g)}. \qquad (32)$$

The exciton binding energy E_{ex} is a product of the band structure and can be expressed to first order in terms of the effective mass as[58]

$$E_{ex} = \frac{m_c m_v}{m_c + m_v} R_H / \varepsilon^2 \,, \qquad (33)$$

where ε is the dimensionless static dielectric constant and $R_H = 13.6$ eV is the hydrogen Ryberg constant. The four terms on the right-hand side of Eq. 32 vary with bandgap energy and their values and power law relation with bandgap energy are provided in Table 13. Experimentally measured exciton binding energies from the literature are used in the calculation of Eq. 32, as the values predicted by Eq. 35 are significantly larger for the smaller bandgap materials.

TABLE 13. Material parameters and calculated absorption amplitude at the bandgap energy. References listed in square brackets for values obtained from the literature, the other values are from this work. The power law relation of the parameters with bandgap energy and reduced effective mass are shown in rightmost two columns.

	GaAs	GaSb	InAs	InSb	Power laws vs E_g	Power laws vs $\frac{m_c m_v}{m_c+m_v}$
Measured bandgap energy E_g from Eq. 26 model fit (eV)	1.4179	0.7304	0.3552	0.1803	1	1.553
Experimental exciton binding energy E_{ex} values (meV)	4.0 [16]	2.1 [51]	1.0 [57]	0.4 [58]	1.110	1.554
Experimental static dielectric constant ε	12.9 [65]	15.7 [66]	15.2 [66]	16.8 [67]	-0.111	-0.157
Experimental reduced effective mass $\frac{m_c m_v}{m_c+m_v}$	0.0595 [16]	0.0364 [68]	0.0245 [69]	0.0131 [70]	0.717	1
Optical density of states effective mass $\left(\frac{m_c m_v}{m_c+m_v}\right)^{3/2}$	0.0145 [16]	0.0069 [68]	0.0038 [69]	0.0015 [70]	1.076	3/2
Theoretical transition strength values $S_0(E_g)$	18.1 [71]	33.8 [71]	60.0 [71]	134.8 [71]	-0.950	-1.415
Measured index of refraction values $n(E_g)$	3.632	3.990	3.607	3.929	-0.019	-0.079
Momentum matrix element $\frac{2}{m_e}\lvert\langle\psi_h\lvert\boldsymbol{p}\rvert\psi_h\rangle\rvert^2$ (eV)	25.6 [71]	24.7 [71]	21.3 [71]	24.3 [71]	0.050	0.195
Calculated absorption amplitude (Eq. 32) α_A (cm^{-1})	21423	12662	9466	4830	0.693	0.956

The experimental values of the joint optical density of states effective mass, the exciton binding energy E_{ex}, and the strength of the Coulomb interaction $\sqrt{E_{ex}}$ all increase with bandgap energy with power laws 1.08, 1.11, and 0.56 respectively. The transition strength S_0 decreases with bandgap energy with power law – 0.95. The index of refraction is about 9% larger for the antimonides and does not significantly vary with bandgap energy. The momentum matrix element $(2/m_e)\lvert\langle\psi_h\lvert\boldsymbol{p}\rvert\psi_e\rangle\rvert^2$ in units of eV and the subsequent transition strength is determined from values of the matrix element P provided in Ref. 71,

which are consistent with other published calculations.[72-74] The momentum matrix element at the Γ point does not significantly change with bandgap energy.

The theoretical absorption amplitude α_A (black circles) and the experimental absorption amplitudes α_g (red squares) and absorption knee α_k (blue diamonds) are compared in Fig. 18 for GaAs, GaSb, InAs, and InSb. The solid curves are fits of a power law to the results for GaAs, GaSb, and InAs (solid symbols), with the best fit expressions indicating a power law near 0.6 for all three measures of absorption strength. The values for InSb (open symbols) are excluded from the fit as the values for InSb do not consistently follow the bandgap dependence trend of the other three materials. The $k \cdot p$ perturbation method employed by E. O. Kane[75] indicates a non-parabolic nature in the InSb conduction band, however this nonparabolicity only becomes a significant correction at about 0.2 eV above the fundamental bandgap energy. The energy range analyzed in this work extends to 0.14 eV above the bandgap energy. The limited agreement between the InSb absorption amplitudes and the power law trend in Fig. 18 are attributed to a much weaker Coulomb interaction that results in a poorly defined knee in the spectrum rather than InSb band nonparabolicity.

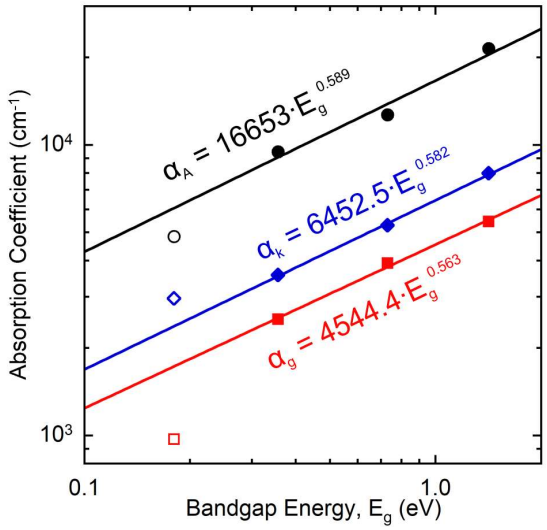

FIG. 18. The calculated absorption amplitude α_A (black circles) and the experimental absorption amplitudes α_g (red squares) and absorption knee α_k (blue diamonds) are compared for GaAs, GaSb, InAs, and InSb. The solid curves are power law fits to the GaAs, GaSb, and InAs results (solid circles), with best fit expressions shown. The results for InSb (open symbols) are excluded from the fits.

The Kramers-Kronig dispersion relation between the real and imaginary parts of the optical constants specifies that onset of absorption in the imaginary parts, k, or ε_2, is manifested as a peak in the real part, n or ε_1[64,76]. This small peak in the real part of the optical constants is denoted as Δn and $\Delta\varepsilon_1$ and is given by Kramers-Kronig relation[76] of the optical constants k and ε_2 evaluated over an integration range of $h\nu_1$ = 1.38 eV to $h\nu_2$ = 1.50 eV, with

$$\Delta n(h\nu) = \frac{2}{\pi}\mathcal{P}\int_{h\nu_1}^{h\nu_2}\frac{k(h\nu')h\nu'}{(h\nu')^2-(h\nu)^2}dh\nu' \tag{34a}$$

$$\Delta\varepsilon_1(h\nu) = \frac{2}{\pi}\mathcal{P}\int_{h\nu_1}^{h\nu_2} \frac{\varepsilon_2(h\nu')h\nu'}{(h\nu')^2 - (h\nu)^2}\, dh\nu' \tag{34b}$$

where $\mathcal{P}$ denotes the Cauchy principal value of the integral. The integration range of 1.38 eV to 1.50 eV is selected to yield the same amplitude of Δn as in the experiment. This integration range yields an amplitude for $\Delta\varepsilon_1$ that is within 5% of the experimental value. The experimental values for Δn and $\Delta\varepsilon_1$ are obtained from the measured data by subtracting off a linear background not attributed to the fundamental absorption edge, which is $n = 2.930 + 0.469 \cdot h\upsilon$ and $\varepsilon_1 = 8.178 + 3.352 \cdot h\upsilon$ for GaAs. It is necessary to subtract the linear background as it results in a blue shift of the peak values that is not attributable to the fundamental bandgap. Decreasing the lower limit of integration below 1.38 eV has no effect on the amplitude or peak position of Δn and $\Delta\varepsilon_1$ due to the rapid decrease in optical absorption below the fundamental absorption edge. However, increasing the upper limit of integration above 1.50 eV increases the amplitude and slightly blue-shifts the peaks in relation to the bandgap energy, which is as much as 0.9 meV for an upper integration limit of 2.50 eV. The integration range of 1.38 eV to 1.50 eV is in agreement with other analysis performed in the literature.[17]

The semi-insulating GaAs bandgap energies at 297 K determined by the various methods discussed in this work are compared in Fig. 19. The values determined from the fit of the model in Eq. 26 to the measured absorption data are indicated in blue and the values determined directly from the measured data are shown in red. The optical constants examined are listed on the horizontal axis, left to right: absorption coefficient α, extinction coefficient k, imaginary dielectric coefficient ε_2, refractive index n, real dielectric coefficient ε_1, refractive index change Δn, and real dielectric coefficient change $\Delta\varepsilon_1$. Error

bars indicate the standard deviation over the three samples measured. The various methods agree within a few meV of each other. The peak values of n and ε_1 are blue shifted by about 2 meV compared to the peak values of Δn and $\Delta\varepsilon_1$, which are blue shifted by about 1 meV compared to their values calculated from the Kramers-Kronig relation using both the model (blue) and the measurements (red). The bandgap energy identified by the first derivative maximum of the absorption coefficient α, extinction coefficient k, and imaginary dielectric function ε_2 is red shifted by about 1 meV using the model (blue) and by about 2 meV using the measured data (red) compared to E_g determined from the model.

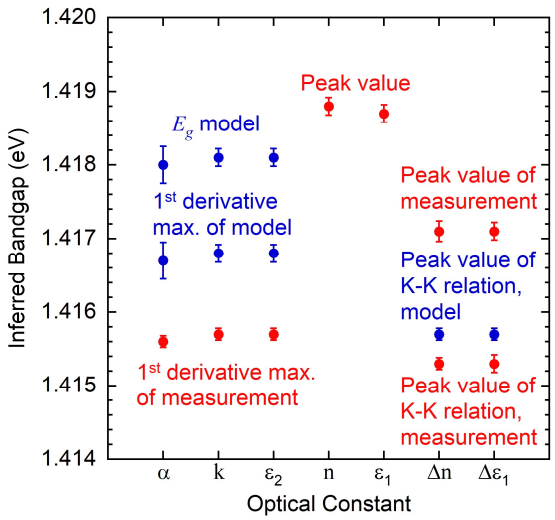

FIG. 19. Comparison of GaAs bandgap energies at 297 K determined from the absorption edge model in Eq. 26 (blue circles) and the measured data (red circles) for the various optical constants and analytical methods, including the positions of peak values and 1st derivative maxima. The error bars show the standard deviation in the measurements of three GaAs samples. The horizontal-axis labels, left to right, are absorption coefficient α, extinction coefficient k, imaginary dielectric coefficient ε_2, refractive index n, real dielectric coefficient ε_1, refractive index change Δn, and real dielectric coefficient change $\Delta\varepsilon_1$.

The energy position of the first derivative maximum E_p of the absorption model in Eq. 26 as a function of the power law parameter p_g is shown in Fig. 20. The first derivative maximum shift relative to the model bandgap energy E_g is shown using the GaAs Urbach energy E_u = 8.70 meV, GaSb E_u = 13.98 meV, InAs E_u = 14.05 meV, InSb E_u = 10.67 meV, and a hypothetical E_u = 1.00 meV. In general the first derivative maximum of the absorption edge model does not occur exactly at the fit parameter E_g except in the specific

cases where p_g is zero or 0.31 as illustrated in Fig. 20. In the case where there is little exponential broadening of the absorption edge, the Urbach energy becomes small, and the first derivative maximum energy approaches the bandgap energy E_g for all values of p_g, as illustrated by the grey curve. Relative to the bandgap parameter E_g the deviation of the first derivative maximum is less than one half of the Urbach energy E_u, and is slightly blue shifted for InSb that has a weak Coulomb interaction and is slightly red shifted for the larger bandgap III-Vs where the Coulomb interaction is more pronounced. The numerical first derivative maxima determined directly from the data for GaAs (1.4156 eV) and for GaSb (0.7272 eV) are also shown in Fig. 20. The values are redshifted by approximately 1.1 meV with respect to the first derivative maximum of the absorption model.

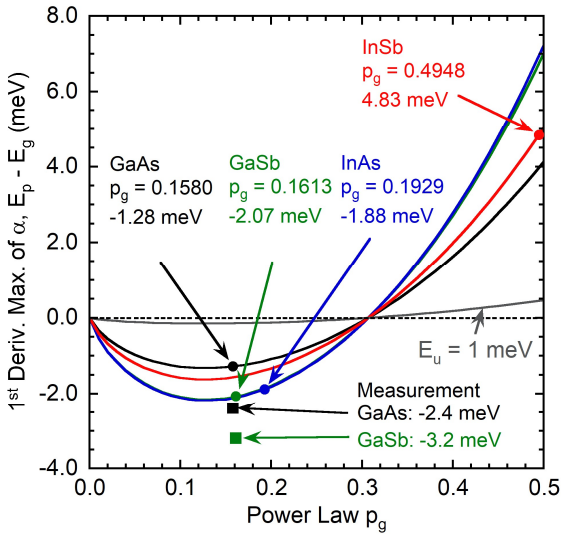

FIG. 20. Comparison of the position of the first derivative maximum to the model parameter $E_p - E_g$ as a function of power law p_g for GaAs (black) with Urbach energy E_u = 8.70 meV, GaSb (green) with E_u = 13.98 meV, InAs (blue) with E_u = 14.05 meV, InSb (red) with E_u = 10.67 meV, and for E_u = 1 meV (grey). The analytical first derivative maxima of the model for each material is shown as solid circles. The numerical first derivative maxima obtained directly from the GaAs and GaSb data is shown as solid squares for comparison.

The ratio of the model parameters E_m/E_g as a function of p_g is shown in red in Fig. 21 for GaAs, GaSb, InAs, and InSb. The ratio of E_m/E_{ex} as a function of p_g, where E_{ex} is the exciton binding energy from Table 13, is shown in blue in Fig. 21 for comparison. These results illustrate that p_g and E_m/E_g are correlated with a power law relation of about 2.2 as shown by the best fit equation in red. The absorption coefficient, bandgap energy, and exciton binding energy all scale with reduced effective mass, $m_c m_v/(m_c + m_v)$. Therefore the relation E_m/E_{ex} versus p_g exhibits a similar power law of about 2.4. The

power law p_g and the ratio E_m/E_g both decrease with increasing bandgap energy, reflecting the increasing strength of the Coulomb interaction between electrons and holes. As the bandgap energy decreases, the Coulomb enhancement of absorption becomes negligible for InSb. As a result the InSb absorption coefficient behaves like that predicted for a parabolic band density of states and a constant transition strength. Larger bandgap materials exhibit reduced dielectric screening by mobile charges due to their stronger atomic potentials, and hence the Coulomb interaction is more pronounced for GaAs, GaSb, and InAs.

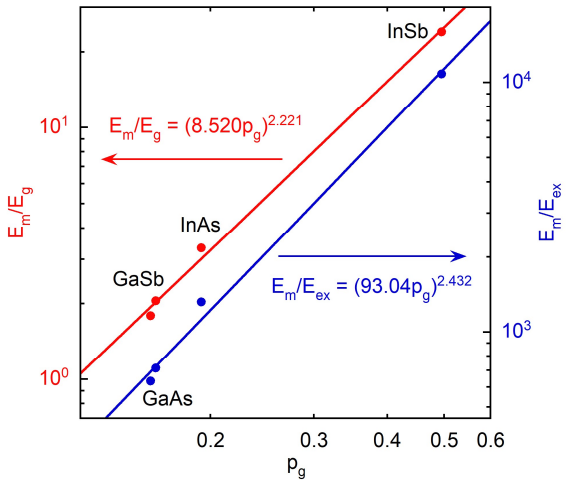

FIG. 21. The ratio of the model parameters E_m/E_g (red) and E_m/E_{ex} (blue) as a function of model parameter p_g for GaAs, GaSb, InAs, and InSb. The power law relation for each is shown.

The exciton binding energies in the III-V semiconductors examined in this work range from approximately 0.4 meV for InSb to 4.0 meV for GaAs, which are relatively small compared to the thermal energy of 25.6 meV at the 297 K measurement temperature.

Nevertheless, an exciton absorption peak is typically observed in high-purity GaAs up to room temperature.[17,60,77-79] However, the semi-insulating GaAs measured in this work has a very short carrier lifetime due to a high density of deep-levels in the material.[80] Therefore an excitonic absorption peak is not observed in the spectroscopic ellipsometry measurements in this work, although the Coulomb interaction is clearly present in the onset of absorption of GaAs, GaSb, and InAs.

For small bandgap InSb where the Coulomb enhancement of absorption is weak, it is straightforward to interpret the model parameters p_g = 0.495 and E_m = 4.33 eV. In the absence of a Coulomb interaction, the power law reduces to the dispersion relation between energy and momentum determined by band structure near the fundamental bandgap. In the nearly free carrier approximation this yields a value of one half corresponding to a parabolic band. Furthermore, the relatively large value of the characteristic energy E_m indicates that the optical transition strength S_0 is close to constant.

The Coulomb enhancement of absorption is significant for GaAs, GaSb, and InAs and complicates the physical interpretation of the model parameters p_g and E_m. Nevertheless, they provide insight to the relative strength of Coulomb interaction and the energy dependence of transition strength. The increase in the magnitude of the Coulomb interaction with bandgap is evident from the decrease in the power law p_g as the absorption at the bandgap energy is enhanced. Furthermore, a picture emerges where the photon energy dependence of the optical transition as a function of bandgap energy is clarified. The decrease in E_m/E_{ex} with bandgap energy associated with the optical transition indicates that as the Coulomb interaction increases, the photon energy dependence changes

from a constant transition strength (Eq. 24c) for small bandgap InSb to a constant dipole matrix element (Eq. 24b) for larger bandgap GaAs.

None of the experimental observations in these materials indicate that the momentum matrix element is independent of photon energy, which is expected to result in negative values for the characteristic energy E_m. However, in Table 13 the theoretical momentum matrix values at the Γ point are nearly constant across the materials examined, which is consistent with the experiment as illustrated by the similar power laws in the increase of absorption magnitude with bandgap energy observed in Fig. 18. Nevertheless, the fact that the momentum matrix element is nearly constant across bandgap energies does not necessarily imply that it should be independent of photon energy for interband optical transitions within a particular material.

A literature survey of the published values of the room-temperature (297 K) bandgap energy of GaAs finds a range of 1.422 to 1.436 eV,[12,77,78,81,82] with a widely accepted value of 1.424 eV.[82] The model in Eq. 26 used in this work identifies the 297 K GaAs bandgap energy at 1.418 eV, approximately 6 meV lower than the commonly-accepted value from literature. Much of the work in the literature identifies the bandgap energy by backing out the Coulomb interaction[82] from a measured feature in the optical constants or by extrapolating the below-bandgap Urbach edge to a known bandgap absorption coefficient.[12,81] On the other hand, in this work the bandgap is identified directly from onset of absorption in the measured optical constants, which may be better described as the optical bandgap.

When comparing the features in the GaAs optical constants measured in this work to those in the literature, the energy of the onset of absorption and the peak in the index of

refraction are at the same energy positions. This indicates that any discrepancy is not due to experimental measurement differences, such as temperature or doping level, but instead is a result of how the bandgap is determined from the optical constants, such as how the onset of absorption is impacted by the Coulomb interaction. There is a distinction between the single-electron bandgap, a theoretical construct based on the assumption of empty conduction band that neglects many-body effects, and the optical bandgap energy that includes the effects of electron-electron interactions and electron-hole interactions, encompassing excitonic absorption and the Coulomb interaction. These effects result in a smaller optical bandgap than that predicted from the single-electron model.

The optical bandgap energy is the most relevant consideration in the description and design of optoelectronic devices, as it is the energy of the onset of absorption and emission that determines how devices perform. For example, the bandgap energy is generally described as the cutoff of absorption in photodetectors and photovoltaic solar cells and as the cutoff of emission from light emitting diodes.

Somewhat closer agreement is found between the GaSb, InAs, and InSb bandgap energies measured in this work and those reported in the literature. A literature survey finds 297 K bandgap energies ranging from 0.724 to 0.728 eV for GaSb,[83-86] from 0.350 to 0.356 eV for InAs,[87-89] and from 0.169 to 0.180 eV for InSb.[89-93] The optical bandgap energies measured in this work are 0.730 eV, 0.357 eV, and 0.180 eV for GaSb, InAs, and InSb respectively, which are all on the upper end of the range measured in the literature. Many of these measurements are based on analysis of photoluminescence peak energy or extrapolations of absorption coefficient down to zero. There are complications in the

extraction of optical bandgap energy for each of these various methods which can make it difficult to exactly compare the room temperature bandgap energy.

Appendix D contains a detailed comparison and analysis of the bandgaps measured in this work and those reported in the literature. The measurements reported in the literature were all performed on undoped or non-degenerately doped material.

The absorption model presented is in principle applicable to any direct-gap semiconductor or material that exhibits an exponential absorption edge, such as III-V, II-VI, I-VII, and their alloys. Application to very small bandgap materials operating in the long-wave infrared would be subject to the typical challenges associated with narrow-bandgap materials, such as free carrier absorption and degenerate carrier levels. Furthermore, for materials with strong excitonic absorption, it would be necessary to add a term to capture the excitonic lineshape. This may become a significant effect for high purity materials with bandgaps wider than GaAs. Ionic materials and highly mismatched alloys are expected to exhibit a broader absorption edge and with a subsequent larger Urbach energy E_u.[94] Moreover, alloy-induced inhomogeneous broadening of the absorption edge will complicate the interpretation of the modeled bandgap energy.

3.2 Carrier Recombination Measurements of InAsSb

In addition to a semiconductor material's absorption spectrum and optical constants, its quantum efficiency is a key figure of merit for optical quality. The quantum efficiency is simply the ratio of radiative recombination rate to the total recombination rate; i.e. radiative plus nonradiative recombination. High quantum efficiency is desired for optoelectronic device design. It is important to measure and understand the nonradiative recombination processes in order to inform MBE growth conditions for improved optical quality.

Carrier recombination processes are typically examined by observing how spontaneous emission changes under either pulsed excitation or varying steady-state excitation. In time-resolved photoluminescence measurements, lifetime is determined by pumping semiconductor material with a picosecond-scale laser pulse and measuring luminescence decay rate.[95,96] By contrast, in steady-state photoluminescence measurements lifetime is inferred from how luminescence intensity responds to changes in the excitation rate.[97,98] The latter approach is attractive because unlike non-equilibrium measurement techniques, it is straightforward to perform and allows the examination of carrier lifetime over a wide range of carrier densities.

In this work, the nonradiative lifetime of bulk $InAs_{0.911}Sb_{0.089}$ grown by molecular beam epitaxy is examined using steady-state photoluminescence experiments that are analyzed via the so-called *ABC* power law relations for the various recombination processes observed in semiconductor materials.[97,99,100] During steady-state photoluminescence (PL) measurements of semiconductor active material, the laser pump power P_{PL} (mW) is proportional to the electron-hole pair generation/recombination rate G_{PL} ($cm^{-3}s^{-1}$). This

relationship is expressed in terms of a power series of carrier density n for the first, second, and third order recombination processes, with

$$\frac{\eta_l \cdot P_{PL}}{V_a \cdot h\nu_l} = G_{PL} = An + (1-\gamma_r)Bn^2 + Cn^3 \tag{35}$$

Where $h\nu_l$ is the pump photon energy, $V_a = \pi(d_l/2)^2 d_a$ is the active volume excited by the pump laser, and the recycling factor γ_r is the fraction of spontaneous emission reabsorbed in the active volume.[101] The injection efficiency $\eta_l = T_l(1-R_l)A_l$ is the fraction of total laser pump power absorbed in the active volume and is determined by the experimental setup and the temperature dependent optical properties of the sample measured. Of the total pump power, T_l is the fraction transmitted to and through the cryostat window; of that fraction $1-R_l$ is transmitted through the sample surface, and of that fraction A_l is absorbed in the active volume. The photo-excited active volume is a cylinder with laser beam diameter d_l and sample active layer thickness length d_a.

During photoluminescence measurements, the photogenerated electron Δn and hole Δp concentrations greatly exceed the intrinsic carrier concentration and contributions from unintentional and native donor/acceptors in high quality samples. Therefore the electron n and hole p populations are approximated as $n = p = \Delta n = \Delta p$. The three-recombination terms in Eq. 35 physically reflect, up to third order, the various recombination processes that the electron-hole population undergoes. These processes are designated as Shockley-Read-Hall (SRH) recombination for n, radiative recombination for n^2, and Auger recombination for n^3, with leading coefficients A, B, and C respectively.[41] The *ABC* model was developed to examine carrier recombination in solid-state materials[99,100] and has been successfully applied to III-V semiconductors.[100]

The integrated photoluminescence signal L_{PL} is proportional to the extracted spontaneous emission $\gamma_e Bn^2$ ($cm^{-3}s^{-1}$) observed from the sample, which is proportional to the net spontaneous emission rate $I_{PL} = (1-\gamma_r)Bn^2$ ($cm^{-3}s^{-1}$) within the sample. The following set of relations is obtained by introducing a constant of proportionality B_F that relates the spontaneous emission detected (L_{PL}) to that emitted:

$$B_F L_{PL} = \gamma_e Bn^2 = \eta_e(1-\gamma_r)Bn^2 = \eta_e I_{PL} \tag{36}$$

Where the photon extraction efficiency $\eta_e = \gamma_e/(1-\gamma_r)$ is expressed in terms of the extraction factor γ_e, which is the fraction of total spontaneous emission (Bn^2) extracted, and $1-\gamma_r$, which is the fraction lost (i.e. fraction not recycled).

Directly measuring or calculating the value of B_F is difficult and not practical. However, it can be determined from a measured data set where near unity internal quantum efficiency $\eta_i = I_{PL}/G_{PL}$ is observed, by noting that the external quantum efficiency $\eta_l\eta_e\eta_i$ is equal to the extracted number of photons divided by the total number of pump photons:

$$\eta_l\eta_e\eta_i = \frac{\gamma_e Bn^2 \cdot V_a}{P_{PL}/h\nu_l} \tag{37}$$

This results in an expression for the constant B_F over internal quantum efficiency in terms of experimental parameters and the measured pump power and integrated photoluminescence:

$$\frac{B_F}{\eta_i} = \frac{\eta_l\eta_e}{V_a h\nu_l} \cdot \frac{P_{PL}}{L_{PL}} \tag{38}$$

The internal quantum efficiency is a function of temperature and excitation that approaches unity whenever radiative recombination dominates, in which case the right-hand side of Eq. 38 provides a good estimate for the value of the unknown constant B_F.

With the constants of proportionality known for Eq. 35 and 36, the experimental measurements are described in terms of the rates of photo-generation G_{PL} and radiative recombination I_{PL}, with

$$G_{PL} = A_F \cdot (I_{PL})^{1/2} + I_{PL} + C_F \cdot (I_{PL})^{3/2} \tag{39}$$

The temperature dependent experimental SRH and Auger parameters A_F and C_F are determined by fitting Eq. 39 to the measured data set, where the SRH and Auger coefficients are given by

$$A = A_F\big(B(1-\gamma_r)\big)^{1/2}, \qquad C = C_F\big(B(1-\gamma_r)\big)^{3/2} \tag{40}$$

Once the nonradiative coefficients are known, the carrier density n can be determined from either the photoexcitation rate G_{PL}, the net radiative recombination rate I_{PL}, or the nonradiative recombination rate $G_{PL} - I_{PL}$. Of these, the photoexcitation rate offers the most robust estimate, as there are typically experimental measurement cases where either the radiative or nonradiative recombination rates are very small compared to the photoexcitation rate resulting in a potentially larger relative uncertainty in estimating carrier density using those rates. Therefore, solving the cubic Eq. 35 offers the most robust estimate of the carrier density with $n = f(G_{PL}, B)$.

Since the radiative coefficient B and the carrier concentration n appear as the product Bn^2 in the spontaneous emission term, it is not possible to obtain them independently from the data set. Therefore, the radiative coefficient is expressed in terms of the readily calculable black body emission rate within the active region:[97]

$$Bn_i^2 = \frac{8\pi c}{(hc)^3}\int_{E_g}^{\infty} \alpha_o(h\nu)\big(n_o(h\nu)\big)^2 \frac{(h\nu)^2 dh\nu}{e^{h\nu/kT}-1} \tag{41}$$

where n_i is the intrinsic carrier concentration. The bandgap energy is E_g, the photon energy is $h\nu$, and the thermal energy is kT. In Eq. 41, k is the Boltzmann constant, h is the Planck constant, and c is the speed of light. The integration is performed over energies above the bandgap using measured values of the absorption coefficient $\alpha_o(h\nu)$ and index of refraction $n_o(h\nu)$ that respectively vary strongly and weakly with energy near the bandgap. The intrinsic electron-hole concentration is accurately described[15,102] by the Boltzmann approximation as

$$n_i^2 = N_c N_v e^{-E_g/kT} = 32\pi^3 (m_c m_v)^{3/2} \left(\frac{m \cdot kT}{h^2}\right)^3 e^{-E_g/kT} \tag{42}$$

where m is the electron mass, $m_c = m_e^*/m$ and $m_v = m_h^*/m$ are dimensionless, and m_e^* and m_h^* are the electron and hole effective masses respectively.

The temperature-dependent shift in the bandgap energy and optical constants is described by an Einstein single oscillator model[11,43]

$$E_g(T) = E_g(0) - S_g \frac{kT_E}{e^{\frac{T_E}{T}} - 1} \tag{43}$$

where $E_g(0)$ is the zero temperature bandgap, S_g is a dimensionless coupling constant, T_E is the Einstein single oscillator temperature, and $kT_E/\left(e^{T_E/T} - 1\right)$ is the average thermal energy of the phonon population.[11]

The internal quantum efficiency η_i is an extrinsic property of the sample that, in addition to material performance, depends on photon recycling and hence sample geometry. A good figure of merit for the assessment of material performance that is independent of sample geometry is the spontaneous emission quantum efficiency η_q,

$$\eta_q = \frac{Bn^2}{An + Bn^2 + Cn^3} = \frac{I_{PL}}{G_{PL} - \gamma_r(G_{PL} - I_{PL})} \tag{44}$$

described in terms of the material dependent recombination coefficients and on the far right is ascertained from the experimentally determined net spontaneous emission rate I_{PL} and the excitation density G_{PL} with the effect of photon recycling backed out. It is interesting to note that the analysis shows that the presence of photon recycling affects performance through the loss of recycled carriers to nonradiative recombination.

The cross-section of the sample measured by photoluminescence spectroscopy is shown in Fig. 22 and consists of a 500 nm thick $InAs_{0.911}Sb_{0.089}$ active layer sandwiched between two 10 nm thick AlSb confinement layers and a 10 nm thick GaSb cap to prevent oxidation of the upper AlSb layer, all grown at a temperature of 430 °C on a GaSb substrate by molecular beam epitaxy.[5] The composition of the 500 nm $InAs_{0.911}Sb_{0.089}$ layer is determined by X-ray diffraction and shows the layer is lattice matched to the GaSb substrate. Application of Vegard's Law yields a Sb mole fraction of 0.089.

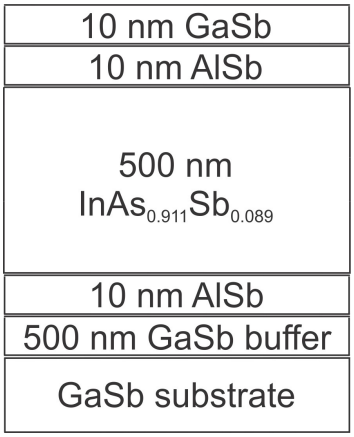

FIG. 22. Cross section of sample used for photoluminescence measurements of $InAs_{0.911}Sb_{0.089}$.

The measurements are performed using pump powers P_{PL} ranging from 0.4 mW to 200 mW and temperatures ranging from 15 K to 295 K. The sample is mounted in a closed-loop He-refrigerated cryostat, enabling measurement at cryogenic temperatures as low as 12 K. The infrared photoluminescence is collected by a Nicolet Magna-IR 760 Fourier Transform infrared spectrometer (FTIR) utilizing a liquid-nitrogen-cooled InSb detector (cutoff wavelength of ~5.5 μm). A spectral resolution of 16 cm^{-1} (2.0 meV) is utilized and is sufficient to resolve the photoluminescence line shape across the entire temperature and excitation range. The sample is optically pumped by an 808 nm laser diode at up to 200 mW incident intensity. The pump laser is modulated at 50 kHz and the detector signal is fed through a phase-locked loop amplifier for improved signal-to-noise ratio. The system optical throughput is measuring using a Mikron M305 black body source at 800 °C.

The measured spectra are normalized to correct for the optical throughput and the integrated photoluminescence signal L_{PL} is obtained by integrating the normalized spectra over energy. For practical purposes L_{PL} is regarded to be a dimensionless quantity in this analysis. This process determines the spontaneous emission I_{PL} (cm^{-3} s^{-1}) within the constant of proportionality B_F for the data set, which has dimensions of spontaneous emission.

The photon recycling and extraction factors γ_r and γ_e, injection efficiency η_l, and active region volume V_a are determined by the sample geometry, measurement set up, and material optical constants. The photon recycling and extraction factors γ_r and γ_e and extraction efficiency η_e are calculated by ray tracing over all solid angles for the InAsSb sample structure[97] and are shown as a function of temperature in Fig. 23. The temperature-dependent absorption coefficient α_g and refractive index n_g used in these calculations are

the effective values determined by averaging the measured $InAs_{0.911}Sb_{0.089}$ optical constants[5] over the measured photoluminescence spectra. The various parameter value ranges over temperature are provided in Table 14.

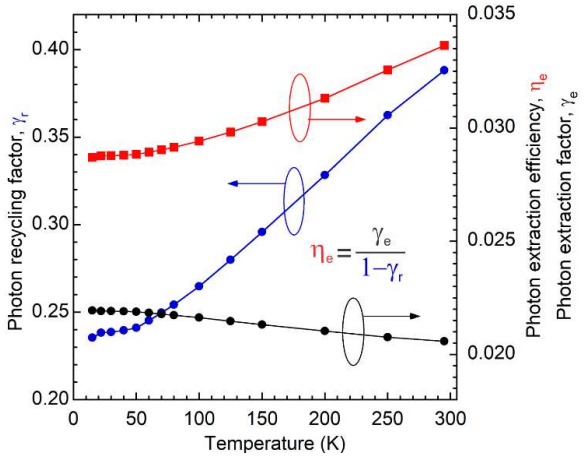

FIG. 23. Photon recycling factor (grey circles, blue online), photon extraction factor (black circles) and photon extraction quantum efficiency (grey squares, red online) for bulk InAsSb as functions of temperature.

TABLE 14. Sample and material parameters used in photoluminescence measurement analysis. Ranges are given for the parameters that vary with temperature; the first value at 15 K and second value at 295 K. Parameters are calculated using $InAs_{0.911}Sb_{0.089}$ optical constants from Ref. [5] and InAs, InSb, GaSb, and AlSb optical constants from Ref. [103].

Parameter	Value
Laser beam diameter d_l	258 μm
Active layer thickness d_a	500 nm
Active region volume V_a	2.61×10^{-8} cm^3
$InAs_{0.911}Sb_{0.089}$ absorption coefficient α_g	3260 - 6580 cm^{-1}
$InAs_{0.911}Sb_{0.089}$ index of refraction n_g	3.739 – 3.715
Pump power fraction at sample T_l	0.604
Reflected fraction R_l	0.399 – 0.398
Absorbed fraction A_l	0.910 – 0.908
Photon recycling factor γ_r	0.235 – 0.388
Photon extraction factor γ_e	0.0219 – 0.0206
Injection efficiency η_l	0.336 – 0.330
Extraction efficiency η_e	0.0287 – 0.0336

From Table 14 it is evident that some sample parameters are strongly temperature dependent, while others are nearly independent of measurement temperature. The slope of the $InAs_{0.911}Sb_{0.089}$ absorption spectrum in the vicinity of bandgap energy is high and hence the effective absorption coefficient α_g increases strongly with temperature; conversely, the slope of the refractive index is small and therefore the temperature dependence of the effective refractive index n_g is minimal. As a result, the reflected fraction R_l and photon extraction factor γ_e (which depend chiefly on refractive index) are also nearly constant. The photon recycling factor γ_r, and hence extraction efficiency η_e, shifts strongly as a direct result of the temperature dependent InAsSb absorption coefficient. The absorbed fraction A_l might therefore be expected to depend strongly on temperature, however, the increased absorption in the 500 nm InAsSb layer at elevated temperatures is

counterbalanced by increased absorption in the 10 nm GaSb cap, and hence A_l and the injection efficiency η_l are nearly constant.

The experimental values on the right hand side of Eq. 38, $\eta_l \eta_e P_{PL}/(V_a h\nu_l L_{PL})$, are plotted as a function of pump power in Fig. 24 on the left-hand vertical axis. The results converge to a minimum value at low temperature over a broad range of pump powers, indicating an asymptotic approach to unity internal quantum efficiency. The asymptotic approach to unity internal quantum efficiency η_i is observed at low temperatures over 4 to 10 mW pump powers. The minimum value provides a good estimate of the constant of proportionally, relating detected photoluminescence to active region spontaneous emission, with $B_F = 4.658\times10^{18}$ cm^{-3}·s^{-1}. The resulting internal quantum efficiency $\eta_i = B_F \cdot (V_a h\nu_l/\eta_l P_{PL}) \cdot (L_{PL}/\eta_e)$ is plotted on the right-hand vertical axis.

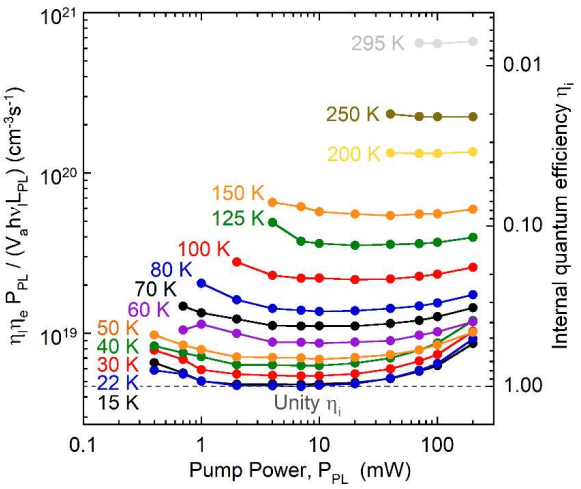

FIG. 24. Excitation density over detected spontaneous emission $(\eta_l P_{PL}/(V_a h\nu_l))/(L_{PL}/\eta_e)$ as function of pump power P_{PL} (solid circles). Each temperature is shown as a separate curve labeled by temperature. The minimum value provides an estimate of $B_F = 4.658\times10^{18}$ cm^{-3}s^{-1}. The corresponding internal quantum efficiency $\eta_i = B_F \cdot (\eta_l P_{PL}/(V_a h\nu_l))/(L_{PL}/\eta_e)$ is plotted on the right-hand vertical axis.

The results are shown in terms of internal excitation density G_{PL} versus internal radiative recombination rate I_{PL} in Fig. 25 as solid circles. The experimental parameters related to nonradiative recombination processes are extracted from plots of G_{PL} versus I_{PL} by fitting Eq. 38 to the data. The unity quantum efficiency line, shown as the dashed line in Fig. 25, provides the ideal reference case where only radiative recombination occurs. At low temperatures the curves approach unity quantum efficiency; as the temperature increases the curves move away from unity quantum efficiency, due mainly to a decrease in the radiative recombination rate with temperature. Furthermore, at low injection SRH recombination dominates and at high injection Auger recombination dominates. As is

typical with small bandgap materials there is only a small excitation and temperature range where radiative recombination dominates.

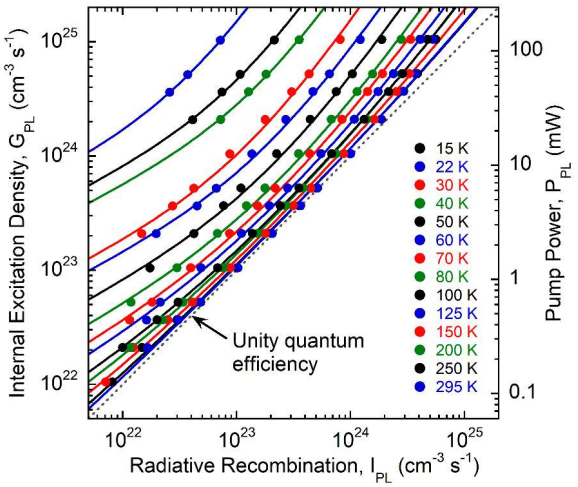

FIG. 25. Internal excitation density G_{PL} as a function of the internal radiative recombination rate I_{PL} at various temperatures. The solid curves are fits of power law recombination rate Eq. 39 to the data. The unity quantum efficiency line (dashed gray line) shows the radiative recombination limit. The SRH fit parameter A_F ranges from 2.4×10^{10} to 1.4×10^{13} $cm^{-3/2}$ $s^{-1/2}$ and the Auger fit parameter C_F ranges from 1.5×10^{-13} to 3.4×10^{-10} $cm^{3/2}$ $s^{1/2}$.

In order to determine the nonradiative recombination coefficients A and C from the fitted parameters A_F and C_F the radiative recombination coefficient B must be calculated using Eq. 41. The Einstein single oscillator model parameters are determined from the bandgap energy inferred from temperature dependent photoluminescence- measurements.[5] The model parameters characterize the shift in optical constants n_o and α_o in Eq. 41 with

temperature. These and other material parameters for InAsSb used in the calculation of Eq. 41 are summarized below in Table 15.

The integral in Eq. 41 spans all photon energies above the bandgap energy. For numerical analysis the upper limit of the integral may be safely truncated to approximately 0.8 eV, as the integrand $(h\nu)^2/\left(e^{h\nu/kT}-1\right)$ diminishes rapidly for photon energies above the bandgap. Eq. 41 is well-approximated by the numerical expression $B = 3.10 \times 10^{-6} \cdot T^{-1.80}$ cm^3 s^{-1}, where the power law -1.80 dependence of temperature is chiefly dominated by the $1/(kT)^2$ dependence of the chemical potential and is modulated slightly by the $\left(S_g kT_E\right)/\left(e^{T_E/T}-1\right)$ and temperature-dependent absorption $\alpha_o(h\nu)$ terms.

TABLE 15. Summary of material parameters used in calculation of radiative recombination coefficient B. Where ranges are given, the left-hand value corresponds to 15 K measurement temperature and the right-hand value to 295 K measurement temperature.

Parameter	Symbol	Value	Source
Dimensionless effective electron mass	m_c	0.02220	Ref. [9]
Dimensionless effective hole mass	m_v	0.41178	Ref. [9]
$InAs_{0.911}Sb_{0.089}$ zero temperature band gap	$E_g(0)$	324.7 meV	Ref. [5]
Einstein model coupling constant	S_g	2.855	Ref. [5]
Einstein temperature	T_E	230.7	Ref. [5]

The SRH and Auger recombination coefficients A and C are calculated using Eq. 40 and the calculated radiative recombination coefficients B given by Eq. 41; the recombination coefficients are summarized below in Table 16. The experimentally determined SRH and Auger coefficients as functions of sample temperature are plotted in Fig. 26. The SRH

lifetime of bulk InAsSb is shown on the right-hand axis of Fig. 26 (a) and decreases from 290 ns at 15 K to 8.5 ns at 295 K. The Auger coefficient is approximately constant over the 50 K to 250 K temperature range, with an average value of 5.1×10^{-26} cm^6s^{-1}. The increase in the Auger coefficient at low temperatures is likely due to an increase in carrier occupation as the effective density of states N_c and N_v rapidly decrease with temperature, proportional to $T^{3/2}$.

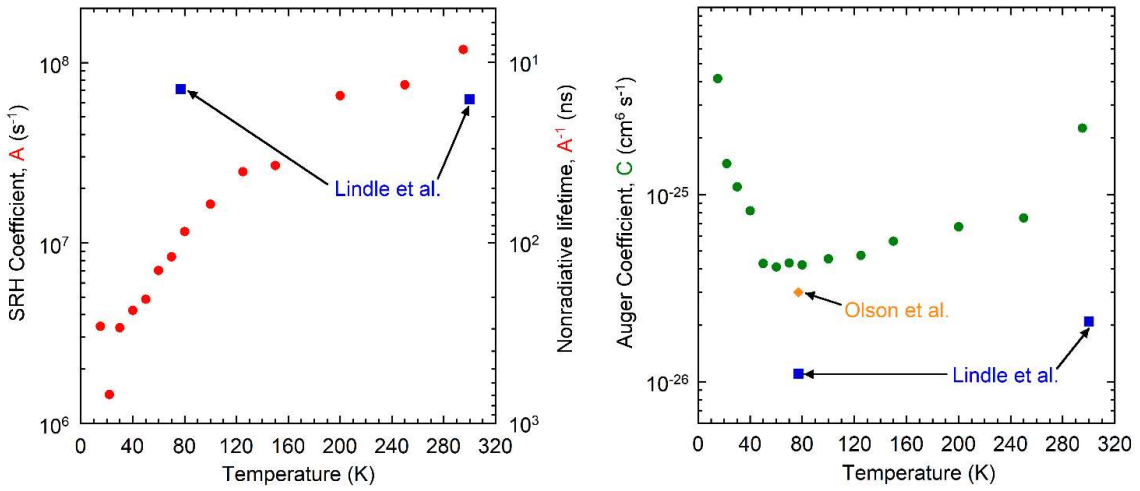

FIG. 26. SRH coefficient (solid black circles, red online) and Auger coefficient (solid gray circles, green online) for bulk InAsSb as functions of temperature. Values reported in the literature are also shown (solid gray squares and solid gray diamond, blue and orange online).[104,105]

TABLE 16. Experimental fitting parameters, SRH coefficients (A), radiative coefficients (B), and Auger coefficients (C). A and C are ascertained using experimental parameters and B is calculated theoretically. The integrated photoluminescence constant of proportionality $B_F = 4.658\times10^{18}$ cm$^{-3}\cdot$s^{-1}.

Temperature (K)	A_F (cm$^{-3/2}$ s$^{-1/2}$)	C_F (cm$^{3/2}$ s$^{1/2}$)	A (s^{-1})	B (cm^3 s^{-1})	C (cm^6 s^{-1})
15	2.430×10^{10}	1.454×10^{-13}	3.452×10^{6}	2.639×10^{-8}	4.168×10^{-25}
22	1.478×10^{10}	1.558×10^{-13}	1.446×10^{6}	1.257×10^{-8}	1.459×10^{-25}
30	4.658×10^{10}	2.850×10^{-13}	3.391×10^{6}	6.961×10^{-9}	1.100×10^{-25}
40	7.608×10^{10}	4.777×10^{-13}	4.225×10^{6}	4.055×10^{-9}	8.179×10^{-26}
50	1.079×10^{11}	4.668×10^{-13}	4.867×10^{6}	2.679×10^{-9}	4.279×10^{-26}
60	1.849×10^{11}	7.447×10^{-13}	7.032×10^{6}	1.916×10^{-9}	4.095×10^{-26}
70	2.543×10^{11}	1.205×10^{-12}	8.376×10^{6}	1.446×10^{-9}	4.306×10^{-26}
80	3.972×10^{11}	1.705×10^{-12}	1.156×10^{7}	1.135×10^{-9}	4.200×10^{-26}
100	6.940×10^{11}	3.413×10^{-12}	1.643×10^{7}	7.621×10^{-10}	4.525×10^{-26}
125	1.289×10^{12}	6.598×10^{-12}	2.484×10^{7}	5.162×10^{-10}	4.727×10^{-26}
150	1.646×10^{12}	1.295×10^{-11}	2.687×10^{7}	3.785×10^{-10}	5.636×10^{-26}
200	5.217×10^{12}	3.383×10^{-11}	6.561×10^{7}	2.354×10^{-10}	6.728×10^{-26}
250	7.369×10^{12}	7.035×10^{-11}	7.528×10^{7}	1.637×10^{-10}	7.501×10^{-26}
295	1.353×10^{12}	3.399×10^{-10}	1.181×10^{8}	1.246×10^{-10}	2.262×10^{-25}

The excess carrier concentration n is calculated from G_{PL} and the recombination parameters A, B, and C by solving Eq. 35 for n. This cubic relation is solved numerically and shown below in Fig. 27. Good agreement is found between these carrier concentrations and those calculated from the net spontaneous emission rate I_{PL} as discussed previously in the introduction. However, carrier concentrations calculated from the nonradiative recombination rate $G_{PL} - I_{PL}$ agree poorly at low measurement temperatures where the internal quantum efficiency is nearly unity and recombination by SRH and Auger processes is minimal.

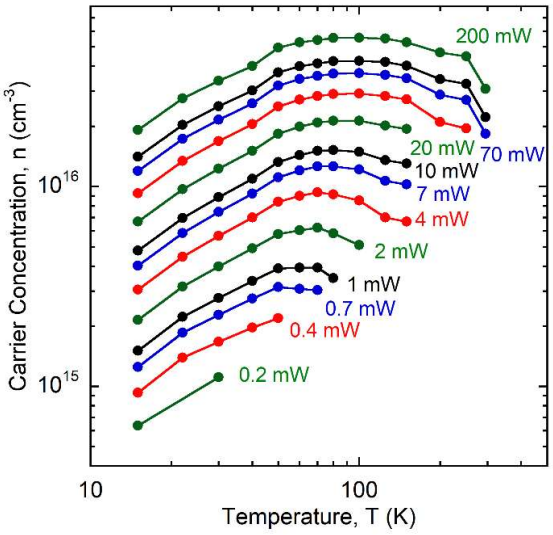

FIG. 27. Carrier concentration as a function of temperature at various excitation levels P_{PL} for bulk InAsSb. The data points are generated by using the fitted recombination rate parameters A, B, and C, and applying Eq. 35 at each measurement temperature.

As expected for steady-state photoluminescence measurements, where the total recombination rate equals the generation rate, the excess carrier concentration n in Fig. 27 increases linearly with laser pump power. Carrier concentration increases with temperature up to approximately 70 K. This is a consequence of the rapidly increasing total recombination lifetime which in the low temperature range is driven largely by the radiative recombination lifetime. The reduction in carrier concentration at elevated temperatures in Fig. 27 is conversely driven by a decrease in total lifetime for fixed excitation levels, due to the decreasing carrier occupation and rapidly increasing effective density of states at higher temperatures.

The rates and lifetimes for radiative, Auger, and total recombination are plotted as a function of carrier concentration in Fig. 28-30. The SRH recombination lifetime (shown

in Fig. 26(a) remains constant with carrier concentration, radiative recombination lifetime varies inversely as the carrier concentration, and Auger recombination lifetime varies inversely as the carrier concentration squared. This is because while a single carrier is involved in SRH recombination, an electron-hole pair must be present for radiative recombination, and three carriers must be present simultaneously for Auger recombination to take place.

Radiative recombination lifetime is highly dependent on both temperature and carrier concentration. The lifetimes range from 2.0 ns at low temperature and high carrier concentration to 309 ns at room temperature. Temperature is observed to be the dominant effect, with radiative lifetimes increasing more than 2 orders of magnitude from 15 K to 295 K. Conversely, the SRH recombination lifetime decreases by approximately one order of magnitude as temperature increases. The increase in radiative lifetime and decrease in SRH lifetime are responsible for the reduction in quantum efficiency (and hence photoluminescence intensity) with increasing temperature. By contrast, the multiple-carrier Auger recombination process is comparatively weakly dependent on temperature.

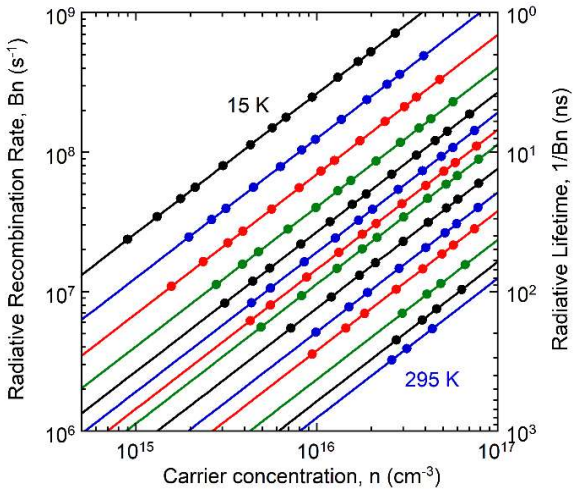

FIG. 28. Radiative recombination rate (solid circles) plotted versus carrier concentration at various temperatures for bulk InAsSb. Solid lines extend the recombination rate Bn to the axis limits. Radiative lifetime shown on right-hand axis.

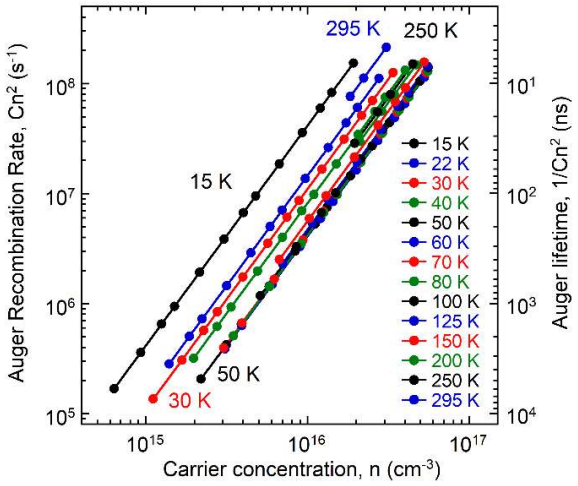

FIG. 29. Auger recombination rate (solid circles) plotted versus carrier concentration at various temperatures for bulk InAsSb. Auger lifetime shown on right-hand axis.

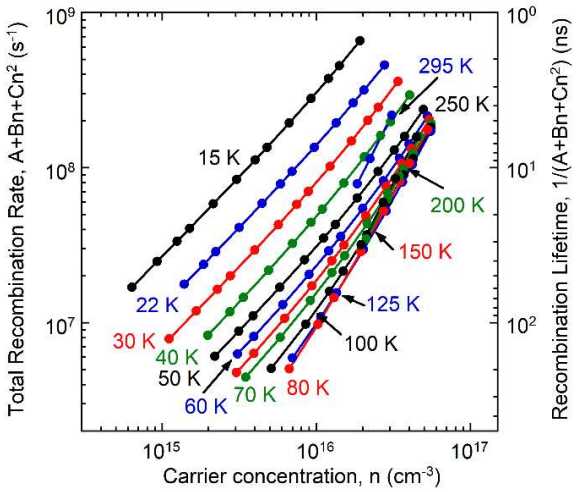

FIG. 30. Total recombination rate (solid circles) plotted versus carrier concentration at various temperatures for bulk InAsSb. Recombination lifetime shown on right-hand axis.

3.3 Optical Properties of InAsSbBi Measured by Photoluminescence Spectroscopy

Similarly to InAsSb discussed above, the InAsSbBi samples are examined using temperature and excitation dependent photoluminescence spectroscopy. The samples are mounted in a closed-loop He-refrigerated cryostat and optically pumped using a modulated 785 nm laser diode. The measurements are performed at various temperatures from 13 to 295 K using average pump powers from 0.100 to 100 mW that provide active layer excitation densities from 0.036 to 36 W/cm^2. The photoluminescence is collected using a Nicolet Magna-IR 760 Fourier Transform infrared spectrometer with an InSb detector with a cutoff wavelength of 5.5 μm. The pump laser is modulated at 50 kHz and the detector signal is fed through a phase-locked loop amplifier for improved signal-to-noise. The system optical throughput is measured and corrected using the spectrum from a Mikron M305 black body source at 800 °C.

The photoluminescence spectra for InAsSbBi samples A, H, and R, and InAsSb reference sample R_1 all measured at 70 K under a 100 mW (120 W/cm^2) excitation are shown in Fig. 31. The InAsSbBi samples exhibit a single well-defined photoluminescence peak energy labeled E_p. The InAsSbBi bandgap energy, labeled E_g, is determined from the first derivative maximum of the photoluminescence energy spectrum,[4,5] which is a measure of the onset of direct optical transitions involving the valence and conduction continuum bands. For the InAsSbBi quantum well samples, this method identifies the ground state transition energy, from which the bandgap energy is found by subtracting the quantum confinement energy shift[15] due to the InAsSb barriers, whose mole fraction is obtained from X-ray diffraction measurements.

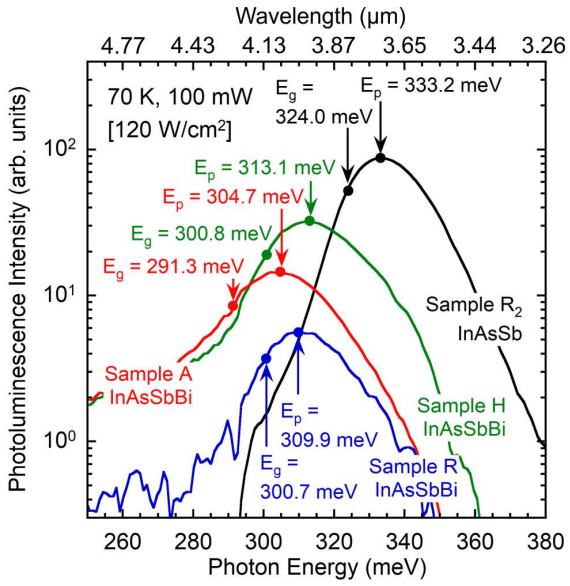

FIG. 31. Photoluminescence spectra measured at 70 K with a 100 mW (120 W/cm^2) excitation for InAsSb reference sample R_2 (black line), 430 °C grown InAsSbBi sample R (blue line), 420 °C grown sample H (green line), and 400 °C grown sample A (red line). The peak energy E_p given by the maximum intensity and bandgap energy E_g given by the first derivative maximum are shown as solid circles and labeled with arrows.

Since the InAsSbBi layers are coherently strained, the unstrained bandgaps are identified by backing out the energy shift due to strain using the Pikus-Bir Hamiltonian.[15] The unstrained bandgap energy as a function of temperature for InAsSbBi samples A through G, H, and R and for the InAs and InAsSb reference samples are shown in Fig. 32. The measured spectra from the one or lowest two excitation densities that provide decent photoluminescence are used in the analysis. This minimizes spurious shifts and broadening of the spectra that can occur with excessively high excitations. The excitation densities therefore vary depending on temperature and material lifetime and range from 7 to 36

W/cm^2 for the InAsSbBi samples and from 0.04 to 36 W/cm^2 for the reference samples, with lower excitation at low temperature and higher excitation at room temperature.

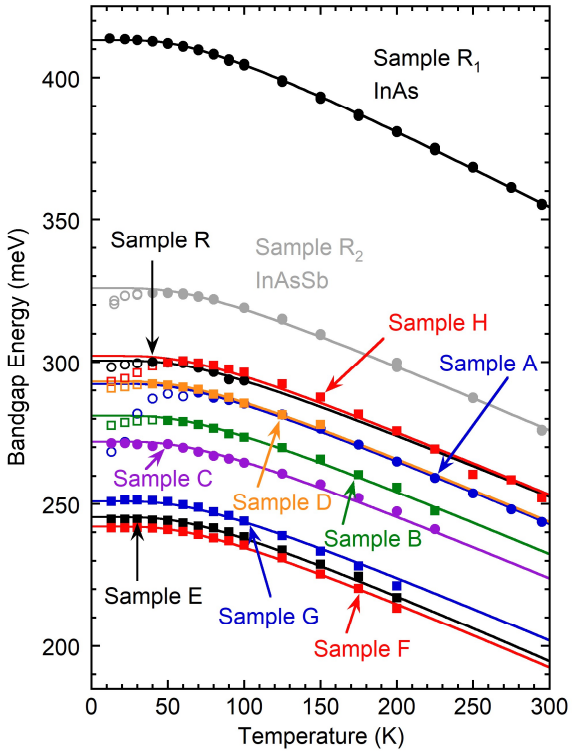

FIG. 32. Bandgap energy as a function of temperature for unstrained InAs, InAsSb, and InAsSbBi. The sample names are indicated for each. The solid symbols indicate the data points fit to the Einstein single-oscillator model (solid curves) and the open symbols indicate the data points not used in the fit as they are indicative of low temperature luminescence from tail states.

Under photoexcitation at low temperatures, the continuum bands are not always populated in alloyed materials where alloy fluctuations and clustering lead to greater densities of localized tail states near the band edges. In this case, the photoluminescence does not always identify bandgap emission, but primarily reflects radiative recombination

from tail states. This is exacerbated in highly mismatched alloys where a characteristic "S-bend" is commonly observed in the position of photoluminescence spectra as function of temperature at low temperatures.[51,106-108] The S-bend shape has been explained using phonon-assisted hopping[109] of carriers within the tail states that form in alloys such as GaAsBi with random crystal disorder and Bi pairing and clustering on adjacent group V lattice sites.[110] A similar temperature dependence of the photoluminescence is observed for InAsSbBi in Fig. 32, where the photoluminescence shifts to lower energies at low temperatures and is most evident for sample A.

The temperature dependence of the bandgap energies is modeled with an Einstein single oscillator[5,11,43] equation of the form

$$E_g(x,y,T) = E_g(x,y,0) - \frac{S_0(x,y)kT_E}{e^{T_E/T} - 1}, \tag{45}$$

where $E_g(x,y,0)$ is the InAsSbBi bandgap energy at 0 K, $S_0(x,y)$ is a dimensionless coupling parameter, k is Boltzmann's constant, T_E is the Einstein temperature, and kT_E is the Einstein energy. The physical Einstein single oscillator equation is chosen over the empirical Varshni equation[9] as it realistically describes the influence of the zero-point motion and the temperature dependence of the phonon occupation on the bandgap energy. The coupling parameter is a measure of the strength of the electron-phonon interaction[11,43] where the linear high-temperature bandgap slope is S_0k. The Einstein temperature and energy are a measure of the average phonon vibration frequency of the lattice[11] that determines the bandgap roll over due to lattice zero-point motion, and in particular provides the temperature $T_E/2$ at which the low and high temperature bandgap asymptotes intersect. The model is fit to the data over the temperatures indicated by the solid symbols in Fig. 32.

The low temperature photoluminescence that appears to originate from localized tail states within the bandgap are indicated by open symbols and are not included in the fit to the model.

The bandgap data sets are fit with the zero temperature bandgap $E_g(x, y, 0)$ as a free parameter for each curve and T_E is treated as a global parameter fixed at 200 K that anchors the fits, works well for InAs and the data set, and is physically expected to be roughly constant over this bandgap range. The coupling parameter $S_0(x, y)$ is assumed to be linear in Bi and Sb mole fraction with

$$S_0(x, y) = S_{0,InAs} - y/y_0 - x/x_0 \,, \tag{46}$$

where $S_{0,InAs}$ = 3.231 is the coupling parameter for InAs, x and y are the Bi and Sb mole fractions, and x_0 and y_0 are constants determined from the data set. This assumption stabilizes the fits using a global coupling parameter that is linear in composition thus reducing the sensitivity of the model to noise in the bandgap data set. The parameter $y_0 = y_{InAsSb}/\left(S_{0,InAs} - S_{0,InAsSb}\right)$ = 0.183 provides a linear interpolation between InAs and InAsSb, where y_{InAsSb} = 0.089 is the Sb mole fraction and $S_{0,InAsSb}$ = 2.744 is the coupling parameter for the InAsSb sample. The parameter x_0 = 0.254 is a global fit parameter whose value is given by the best fit of Eqs. 45 and 46 to the entire data set. The mole fraction dependent zero-temperature unstrained bandgap, depicted in Eq. 47, along with its temperature dependence, depicted in Eqs. 45 and 46, provides a comprehensive description of the bandgap energy of InAsSbBi as function of temperature and composition over the dilute Bi mole fractions examined. The resulting bandgap model is expressed as

$$E_{g,InAsSbBi}(x,y,T) = (1-x-y)E_{g,InAs} + yE_{g,InSb} + xE_{g,InBi} - y(1-y)b_{g,InAsSb} - x(1-x)b_{g,InAsBi,0}e^{-x/x_a} - \left(S_{0,InAs} - y/y_0 - x/x_0\right)\cdot kT_E/\left(e^{T_E/T}-1\right), \quad (47)$$

where the last term describes the temperature dependence and the other terms describe the zero-temperature bandgap. The parameter values are summarized in Table 17.

TABLE 17. Parameter values for the InAsSbBi bandgap model in Eq. 47 as function of Sb and Bi mole fraction and temperature.

Parameter	Value	References
$E_{g,InAs}$ (eV)	0.4135	This work
$E_{g,InSb}$ (eV)	0.235	[15]
$E_{g,InBi}$ (eV)	-1.63	[111]
$b_{g,InAsSb}$ (eV)	0.901	This work
$b_{g,InAsBi,0}$ (eV)	3.629	This work
x_a	0.229	This work
$S_{0,InAs}$	3.231	This work
x_0	0.254	This work
y_0	0.183	This work
T_E (K)	200.0	This work

The Bi and Sb mole fractions are ascertained from the unstrained zero-temperature bandgap determined by photoluminescence and the lattice constant determined by X-ray diffraction. Photoluminescence measurements are sensitive to small changes in bandgap energy, making them highly sensitive to the dilute Bi mole fractions present in the InAsSbBi layers. The Sb mole fraction, $y(x)$ in Eq. 4, is expressed in terms of Bi mole fraction and lattice constant, from which the zero-temperature bandgap, $E_{g,InAsSbBi}(x,y(x),0)$, Eq. 47 with T = 0, is expressed in terms of the Bi mole fraction, x. The InAsSbBi mole fractions obtained from the solution of these equations are listed in Table 1. The zero-temperature bandgap $E_g(x,y,0)$, coupling parameter $S_0(x,y)$, and Bi

and Sb mole fractions for each sample are provided in Table 18, with the samples listed in order of decreasing bandgap.

TABLE 18. Einstein single oscillator model parameters, photoluminescence width parameters, and Bi and Sb mole fractions for each sample listed in the order of decreasing bandgap energy.

Sample	Mole Fraction (%) Bi, x	Sb, y	$E_g(x,y,0)$ (meV)	$S_0(x,y)$	Slope, m_w	Intercept, b_w (meV)
R_1	-	-	413.2	3.231	0.377	0.75
R_2	-	8.91	325.9	2.744	0.596	3.04
H	0.29	9.70	302.2	2.690	0.249	11.08
R	0.18	10.76	300.5	2.636	0.421	9.45
D	0.58	8.92	293.1	2.721	0.319	12.47
A	0.58	9.06	292.3	2.713	0.219	13.18
B	0.71	9.61	281.1	2.678	0.507	13.10
C	0.81	10.05	272.0	2.650	0.431	12.56
G	1.35	8.90	250.9	2.692	0.295	6.11
E	1.86	6.85	245.3	2.784	0.379	6.87
F	1.67	8.17	242.0	2.719	0.428	6.51

The photoluminescence spectra from the InAsSb and InAsSbBi samples exhibit alloy induced broadening.[112,113] The spectra from the InAsSb reference sample and the InAsSbBi sample H are compared to the InAs reference sample in Fig. 33 at four temperatures 70 (a), 150 (b), 200 (c), and 295 K (d). The spectra are normalized to a peak intensity of one and shifted in energy so that the bandgaps, given by the first derivative maximum, are aligned. Spectra for two different excitation levels are shown for each, indicating the spectral width is independent of the excitation density at these temperatures. Compared to InAs, the spectra are broadened by the addition of 8.9% Sb and further broadened by the addition of 0.3% Bi.

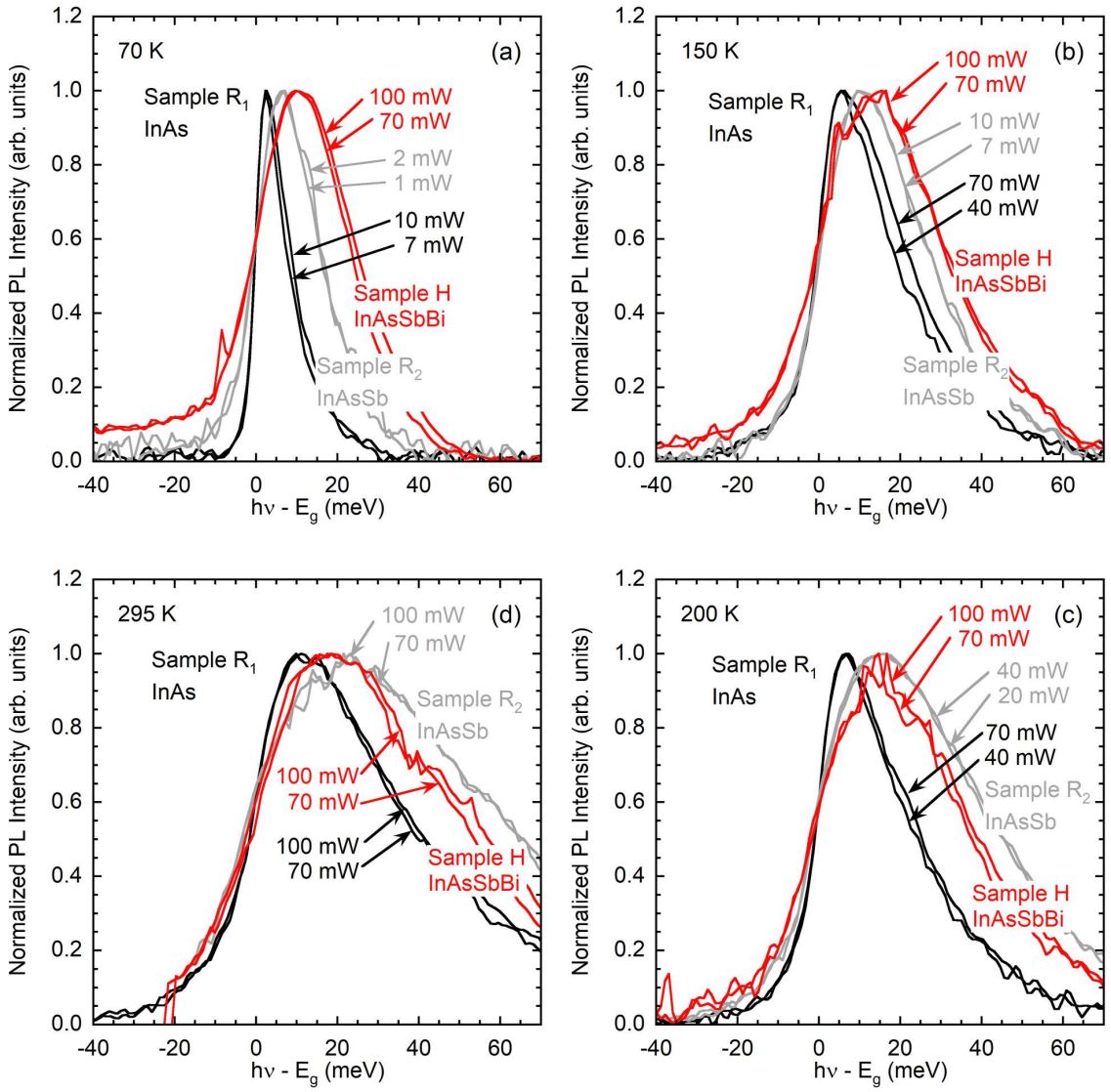

FIG. 33. Photoluminescence spectra from bulk InAs, $InAs_{0.911}Sb_{0.089}$, and $InAs_{0.900}Sb_{0.097}Bi_{0.003}$ (sample H) at (a) 70 K, (b) 150 K, (c) 200 K, and (d) 295 K. Measured spectra are normalized to unity peak amplitude and are shifted by the bandgap energy E_g to illustrate the effects of broadening due to Sb and Bi alloying.

The energy separation between the photoluminescence peak, E_p, and the bandgap, E_g, defines the width of the photoluminescence spectra as $E_p - E_g$, which is plotted as a

function of thermal energy kT in Fig. 34. Linear fits to the width in the form of $m_w \cdot kT + b_w$ provide the dimensionless slope m_w of the temperature dependence and a measure of the "built-in" broadening given by the zero temperature intercept b_w. The best fit parameters are summarized in Table 18. InAs approaches the ideal case where the separation of the bandgap and peak energies approach zero at low temperature, with a built-in broadening of only 0.75 meV, due to the presence of tail states that arise from the zero-point motion of the lattice. InAsSb has a built-in broadening of about 3 meV due to an increase in the density of tail states due to Sb alloying in InAs, and has a stronger temperature dependence due to inhomogeneous broadening. The InAsSbBi material exhibits a larger built-in broadening of approximately 6 meV for quantum wells and 13 meV for bulk samples. The narrower photoluminescence from the quantum wells is likely due to less variation in the both the vertical and lateral Bi composition, which is observed to increase as the growth progresses.[34] The slope of the temperature-dependent photoluminescence width is smaller in InAsSbBi, ranging from about 0.2 to 0.5.

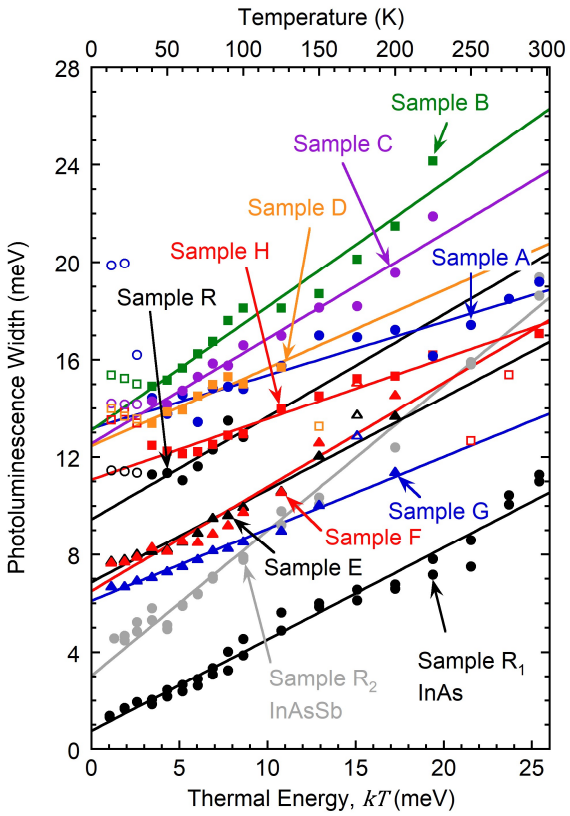

FIG. 34. Photoluminescence width versus thermal energy kT for InAs, $InAs_{0.911}Sb_{0.089}$, InAsSbBi bulk samples A through D, H, and R, and InAsSbBi quantum well samples E through G. Solid symbols indicate data points fit to a linear equation shown by the solid lines, and the open symbols indicate the data points not fit as they are indicative of low temperature luminescence from well within the tail states that further broaden the spectra.

The difference in the width of the photoluminescence between bulk InAsSbBi and bulk InAsSb is the portion of the broadening that the Bi alloy introduces. This broadening is likely a result of lateral composition modulation[34] and an increase in the density of localized tail states due to the size and electronic mismatch of Bi atoms, pairs, and clusters[44,45,113] and possibly point defects due to below optimal growth temperatures.[11,114] By contrast, deep level defect states or traps do not yield observable photoluminescence

and hence do not contribute to the broadening. In particular the presence of lateral composition variations result in microscopic regions of differing electronic band structure that broaden the observed photoluminescence. Inhomogeneous broadening complicates the measurement of the bandgap energy of the InAsSbBi alloy, as the first derivative maximum method and the extrapolation of the temperature dependent measurements to zero-temperature typically identifies the onset of emission from a lower range of the bandgap energies, rather than the exact average of all bandgaps present, which can result in an overestimation of the average Bi mole fraction.

The zero-temperature strained bandgap of InAsSbBi on GaSb as a function of strain is shown in Fig. 35 with contours of constant Sb and constant Bi mole fraction. The zero-temperature strained bandgap energies for each sample are shown as solid symbols. The Bi mole fractions range from 0.18% to 1.86% and all samples are compressively strained with values from -0.025% to -0.142%, corresponding to critical thicknesses from 1700 nm to 240 nm. The net compressive strain is a result of the incorporation of too much Sb (0.4% to 2.2%), indicating that the Sb/In flux ratio should be reduced by about 0.005 to 0.027 for these growth conditions.

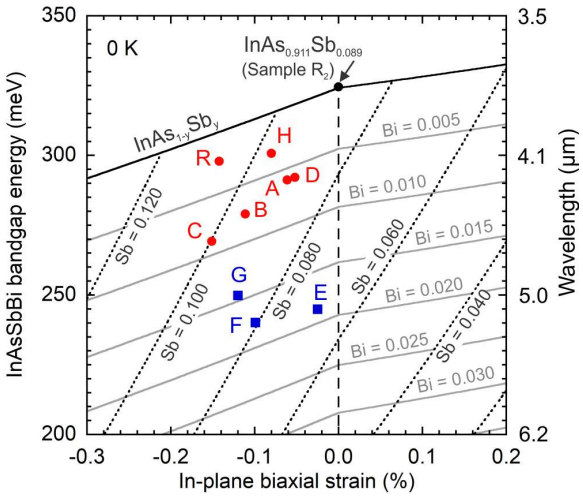

FIG. 35. Low-temperature strained bandgap energy of InAsSbBi as a function of strain with contours of constant Sb (dashed black curves) and constant Bi (solid grey curves). The strained bandgap energies of the bulk samples are overlaid as red circles and the quantum well samples as blue squares. The sample names are provided for each.

In this work, a combination of X-ray diffraction and photoluminescence is utilized to determine the average composition of the InAsSbBi active layers. X-ray diffraction provides accurate measurements of the InAsSbBi layer lattice constant and distinguishes the strain of the InAsSbBi layer from the strain of the other layers, while photoluminescence provides the average bandgap energy of the InAsSbBi layer. The combination of these two measurements is sensitive to small variations in the Sb and Bi mole fractions. Alternate methods include absorption measurements to determine bandgap energy and Rutherford back-scattering spectrometry or secondary ion mass spectroscopy measurements to determine Bi mole fraction. Although absorption measurements accurately determine the bandgap energy of thick bulk layers, in these samples they are subject to parasitic absorption from the presence of Bi-rich surface features and thin film

interference from the presence of thin barrier layers, both of which distort the location of the absorption edge. Rutherford back-scattering is strongly influenced by the presence of Bi-rich surface features, and hence overestimates the average Bi mole fractions in many of these samples.[34] Secondary ion mass spectroscopy is insensitive to the low Bi ion yield in dilute Bi layers at typical milling rates.

The determination of the unstrained bandgap energy of InAsSbBi is limited by how accurately the first derivative of the photoluminescence represents the average bandgap and by the uncertainty in determining the energy shift due to strain, and in the case of quantum well samples, also by the uncertainty in determining the quantum confinement shift. Although the average bandgap may not be perfectly represented, the first derivative method is systematically applied to the experimental measurements employed in the bandgap model making the extraction of average Bi mole fraction consistent and reasonably accurate compared to the inhomogeneous broadening of the spectra. This broadening indicates that the bandgap varies by several meV within the InAsSbBi layer. The InAsSb spectra are inhomogeneously broadened due to alloying Sb with As on the group-V sublattice and spectra of InAsSbBi spectra are further broadened when Bi is alloyed with As and Sb. For example, adding about 9% Sb to InAs roughly doubles the width of the spectra, while adding about 0.5% Bi roughly doubles the width of spectra over that of InAsSb.

The modification in bandgap energy due to strain is small and varies from 1 to 3 meV for this sample set. The bandgap shift due to strain is specified by the deformation potentials that are assumed to be linear functions of composition and that are not known for InBi. Nevertheless, the uncertainty in the InBi values contributes little uncertainty to

the InAsSbBi deformation potentials for dilute amounts of Bi. For example, if the deformation potential of InBi varies by a factor of ten from its assumed nominal value, the impact on the inferred bandgap energy is less than 0.1 meV. As a comparison, if the InAs deformation potentials vary by ± 20%, the impact is ≤ 0.5 meV. In the case of the quantum confinement shift, if the band offsets between the InAsSb barriers and the InAsSbBi quantum wells vary by ± 20%, the inferred bandgap varies by ≤ 3 meV. The bandgap inferred from quantum well emission typically has a larger uncertainty compared to that of bulk material, because band offsets are comparatively difficult to determine.

Assuming the broadening is entirely due to fluctuations in mole fraction, the relative variation in the Sb mole fraction is about ± 7% or 0.089 ± 0.006 for the bulk InAsSb sample, while the relative fluctuations in the Bi mole fraction are observed to be about ± 20% for the bulk InAsSbBi samples and about ± 10% for the quantum well samples. In addition to composition variation, the broadening mechanisms comprise local bandgap differences due to the configuration of the Bi atoms on the group-V sublattice, which includes isolated Bi atoms, pairing and clustering, and quasi random distributions.[110] Theoretical work[110,115] indicates that even for dilute amounts of Bi the local bandgaps of GaAsBi and InPBi are expected to vary by tens of meV depending on Bi atom configuration, and hence is expected to be a large contributor to broadening in dilute Bi III-Vs.

The spatial variation of the Bi mole fraction in samples A, B, H, and R has been measured using chemically sensitive (200) dark field transmission electron microscopy and reported in reference 35. The average Bi mole fraction and standard deviation is determined to be 0.00516 ± 0.00033, 0.00777 ± 0.00020, 0.00364 ± 0.00006, and 0.00144 ± 0.00007 for samples A, B, H, and R respectively. These results compare reasonably well

to the 0.0058, 0.0071, 0.0029, and 0.0018 values obtained from the photoluminescence analysis. The Bi composition variation is observed to occur on a lateral length scale of about 30 nm[34] with relative fluctuations ranging from ± 2% to 6%, which accounts for only part of the observed inhomogeneous broadening. Therefore variations in the Bi atom configuration are likely play a dominant role in the spectral broadening of the emission from InAsSbBi. Broad photoluminescence is a source of uncertainty in determining the average bandgap energy and the subsequent average mole fractions of InAsSbBi, as is the ability of the bandgap model to relate mole fraction to bandgap energy. Nevertheless, the near agreement between the average Bi mole fractions determined by structural examination using electron microscopy and those determined by photoluminescence, indicate that the overall approach of the analyses is reasonably accurate. The large amount of time and resources required for sample preparation and imaging limits this comparison to a few samples.

4: BANDGAP AND BAND OFFSETS IN III-V-Bi SEMICONDUCTOR ALLOYS

The bandgap energy and band edge offsets of III-V bismide alloys including InAsSbBi and GaAsSbBi is a key parameter determining the material's wavelength and optical performance. Accurate knowledge of the conduction and valence band offsets and their strain dependence is necessary to design practical heterostructures for use as active regions in optoelectronic devices including lasers, photodetectors, and light emitting diodes.

The unstrained bulk bandgap of $InAs_{1-x-y}Sb_yBi_x$ as a function of Bi and Sb mole fractions, x and y, can be described as a linear combination of the three constituent binary bandgaps, E_g, and the three constituent ternary bowing terms, b_g,[2,4,5] where

$$E_{g,InAsSbBi}(x,y) = (1-x-y)E_{g,InAs} + yE_{g,InSb} + xE_{g,InBi} - \left[y(1-x-y)b_{g,InAsSb} + x(1-x-y)b_{g,InAsBi} + xyb_{g,InSbBi}\right]. \quad (48)$$

The binary bandgaps of the III-V materials typically decrease with temperature and the temperature dependence is known for InAs and InSb, but not InBi. The conduction and valence band edge energies E_c and E_v are also described using the same form with band edge bowing parameters b_c and b_v. The relation between the band edges and the bandgap is $E_g = E_c - E_v$ and $b_g = b_c - b_v$.

In the dilute Bi regime, the bandgap bowing in InAsBi is experimentally observed[4,116,117] to obey a band anti-crossing model[6,118,119] where the Bi 6p orbital interacts resonantly with the host valence band edge. The conduction band edge is assumed to be linear with the interaction only occurring at the valence band edge, which is given by

$$E_{v,InAsBi}(x) = \frac{(1-x)}{2}\left(x\Delta E_v + E_{Bi} + \sqrt{(x\Delta E_v - E_{Bi})^2 + 4{C_{Bi}}^2 x}\right) + x^2\Delta E_v + E_{v,InAs}\,. \quad (49)$$

The parameter $\Delta E_v = E_{v,InBi} - E_{v,InAs}$ = 0.81 eV is the separation of the binary valence band edges and E_{Bi} = -0.606 eV is the impurity energy level[4,6] of the Bi 6p orbital relative to the InAs valence band edge $E_{v,InAs}$. The Bi coupling coefficient C_{Bi} describes the strength of the bowing due to the band anti-crossing interaction and is determined to be C_{Bi} =1.518 eV using the valence band edges of InAs[9], InBi,[111] and $InAs_{0.936}Bi_{0.064}$, with the latter determined from its bandgap energy of 0.063 eV.[2] The relevant binary band edges and bandgaps are summarized in Table 19, where experimental room temperature (295 K) values are available for InAs[9] and InSb[9], and theoretical (temperature not included) values are available for semimetallic InBi.[111] The InAs conduction band edge is given by the valence band edge plus the bandgap measured in this work.

Since experimental measurements of zinc-blende InBi are not available, the material parameters used are based on theoretical calculations and extrapolated experimental values. Calculations using the local density approximation yield a semimetallic InBi bandgap energy of -1.63 eV.[111] The lattice constant is extrapolated from experimental measurements of InAsBi.[26] Poisson's ratio is estimated using extrapolated elastic constants from the other In-V binaries.[26] The valence band offset is determined using a similar extrapolation.[4] The deformation potentials are assumed equal to those of InAs, as experimental or theoretical values are not available.[4] The limited knowledge of the InBi material parameters is a source of uncertainty, however for the dilute Bi compositions considered in this work, this uncertainty has minimal impact.

Since the band anti-crossing model is not described by a constant bowing, a variable valence band edge bowing parameter $b_{v,InAsBi}(x) = b_{v,InAsBi,0}e^{-x/x_a}$ is introduced for InAsBi. The best fit values for x_a and $b_{v,InAsBi,0}$ are determined by fitting the valence band bowing term to the valence band anti-crossing curve over the Bi mole fraction range $0 \leq x \leq 6.4\%$, with $b_{v,InAsBi,0}$ = 3.629 eV and x_a = 0.229. This variable bowing parameter estimates the bowing behavior of Eq. 49 within ± 0.7 meV over this Bi mole fraction range. Since the conduction band edge is assumed to be linear, the bandgap bowing $b_{g,InAsBi}(x) = -b_{v,InAsBi,0}e^{-x/x_a}$.

The InSbBi bowing parameters b_{InSbBi} are not known and as a simplification are assumed to equal the sum of the InAsSb and InAsBi bowing parameters,[2] with $b_{InSbBi} = b_{InAsSb} + b_{InAsBi}$. This assumption reduces the sum of the three bowing terms in Eq. 48 to $y(1-y)b_{g,InAsSb} + x(1-x)b_{g,InAsBi}(x)$, which is valid for nearly lattice matched InAsSbBi, as the relatively small Sb and Bi mole fractions result in an insubstantial contribution from the InSbBi bowing term. The InAsBi bowing parameters are assumed to be temperature independent, since only room temperature values are available. The room and low temperature InAsSb bowing parameters measured in this work differ by about 0.12 eV. The InAsSbBi bowing coefficients are given in Table 19.

TABLE 19. Material parameters for the constituent binary and ternary alloys of InAsSbBi used to model the unstrained and strained band edge and bandgap energies. Values are shown for both low and room temperature when known, otherwise they are assumed to be independent of temperature. The source for each value is indicated in square brackets, with [tw] used for this work.

	Temperature	InAs	InSb	InBi
Bandgap energy E_g (eV)	0 K	0.4135 [tw]	0.235 [9]	-1.63 [111]
	295 K	0.3559 [tw]	0.172 [9]	-1.63 [111]
Conduction band edge E_c (eV)	0 K	-0.1765 [tw]	0.235 [9]	-1.41 [4]
	295 K	-0.2341 [tw]	0.172 [9]	-1.41 [4]
Valence band edge E_v (eV)		-0.5900 [9]	0.000 [9]	0.22 [26]
Lattice constant a (Å)		6.0583 [9]	6.4794 [9]	6.6108 [26]
Poisson's Ratio ν		0.3521 [9]	0.3530 [9]	0.3503 [26]
Hydrostatic deformation potential a_c (eV)		-5.08 [9]	-6.94 [9]	-5.08 [4]
Hydrostatic deformation potential a_v (eV)		-1.00 [9]	-0.36 [9]	-1.00 [4]
Shear deformation potential b (eV)		-1.80 [9]	-2.00 [9]	-1.80 [4]
	Temperature	InAsSb	InAsBi	InSbBi
Bandgap bowing b_g (eV)	0 K	0.901 [tw]	$3.629e^{-x/0.229}$ [tw]	$b_{InSbBi} = b_{InAsSb} + b_{InAsBi}$ [2]
	295 K	0.783 [tw]		
Valence bowing b_v (eV)	0 K	-0.380 [5]	$-3.629e^{-x/0.229}$ [tw]	
	295 K	-0.367 [5]		
Conduction bowing b_c (eV)	0 K	0.521 [tw]	0.000 [tw]	
	295 K	0.416 [tw]		

The complementary Ga-containing quaternary alloy $GaAs_{1-x-y}Sb_yBi_x$ is treated in a parallel manner to $InAs_{1-x-y}Sb_yBi_x$. The unstrained bulk bandgap energy of GaAsSbBi is described by Eq. 48 with the In-containing compounds replaced by their Ga-containing counterparts. Likewise, the GaAsBi and GaSbBi valence band edges are described by the band anti-crossing Eq. 49. For GaAsBi, the band anti-crossing parameters are $\Delta E_v = E_{v,GaBi} - E_{v,GaAs}$ = 1.229 eV, the separation of the binary valence band edges[9,111], E_{Bi} = -0.40 eV is the impurity energy level[120] of the Bi 6p orbital relative to the GaAs valence band edge $E_{v,GaAs}$, and C_{Bi} = 1.55 eV is the Bi coupling coefficient.[120] Fitting a variable

GaAsBi bowing coefficient to the valence band anti-crossing expression over the Bi mole fraction $0 \leq x \leq 20.0\%$ yields $b_{v,GaAsBi}(x) = -4.251e^{-x/0.290}$. The maximum error of this expression is 13 meV over the fitted Bi mole fraction range. Because the GaAsBi ternary alloy forms a relatively small fraction of the overall composition of nearly lattice matched GaAsSbBi alloys, this error may be safely neglected.

The GaSbBi ternary alloy is also treated by a valence band anti-crossing expression. Unlike InSbBi, which forms a small fraction of the overall InAsSbBi composition for practical alloys, the GaSbBi bowing cannot be neglected or simplified as a sum of the other bowing parameters, as was assumed for InSbBi. The GaSbBi band anti-crossing parameters are $\Delta E_v = E_{v,GaBi} - E_{v,GaSb}$ = 0.459 eV, the separation of the binary valence band edges[9,111], E_{Bi} = -1.17 eV is the impurity energy level[120] of the Bi 6p orbital relative to the GaSb valence band edge $E_{v,GaSb}$, and C_{Bi} = 1.263 eV is the Bi coupling coefficient. Fitting a variable GaSbBi bowing coefficient to the valence band anti-crossing expression over the Bi mole fraction $0 \leq x \leq 20.0\%$ yields $b_{v,GaSbBi}(x) = -1.331e^{-x/0.937}$. The maximum error of this expression is 0.7 meV over the fitted Bi mole fraction range. The bowing parameters are assumed to be temperature independent, since only low temperature values are available. The Ga-containing binary band edges, bandgaps, and GaAsSbBi bowing coefficients are given in Table 20.

TABLE 20. Material parameters for the constituent binary and ternary alloys of GaAsSbBi used to model the unstrained and strained band edge and bandgap energies. Values are shown for both low and room temperature when known, otherwise they are assumed to be independent of temperature. The source for each value is indicated in square brackets, with [tw] used for this work.

	Temperature	GaAs	GaSb	GaBi
Bandgap energy E_g (eV)	0 K	1.519 [9]	0.812 [9]	-1.45 [111]
	295 K	1.425 [9]	0.729 [9]	-1.45 [111]
Conduction band edge E_c (eV)	0 K	0.719 [9]	0.782 [9]	-1.021 [111]
	295 K	0.625 [9]	0.699 [9]	-1.021 [111]
Valence band edge E_v (eV)		-0.800 [9]	-0.030 [9]	0.429 [tw]
Lattice constant a (Å)		5.65325 [9]	6.0959 [9]	6.33 [121]
Poisson's Ratio ν		0.3167 [9]	0.3129 [9]	0.3186 [120]
Hydrostatic deformation potential a_c (eV)		-7.17 [9]	-7.5 [9]	-7.5 [9]
Hydrostatic deformation potential a_v (eV)		-1.16 [9]	-0.8 [9]	-0.8 [9]
Shear deformation potential b (eV)		-2.00 [9]	-2.0 [9]	-2.0 [9]
	Temperature	GaAsSb	GaAsBi	GaSbBi
Bandgap bowing b_g (eV)	0 K 295 K	1.43 [9]	$4.251e^{-x/0.290}$ [tw]	$1.331e^{-x/0.937}$ [tw]
Valence bowing b_v (eV)	0 K 295 K	-1.06 [9]	$-4.251e^{-x/0.290}$ [tw]	$-1.331e^{-x/0.937}$ [tw]
Conduction bowing b_c (eV)	0 K 295 K	0.37 [9]	0.000 [tw]	0.000 [tw]

In pratice, quaternary materials are rarely grown lattice matched to the extent that strain does not significantly impact the optical properties or that the residual strain cannot be differentiated by X-ray diffraction. Therefore the layers typically have measureable levels of strain with optical properties that depend on both mole fraction and strain. For example, 0.1% tensile strain in InAsSbBi increases the bandgap by about 5 meV. The pseudomorphic strained band edge and subsequent bandgap energies are determined by modifying the unstrained band edge positions using the Pikus-Bir Hamiltonian,[15] where the binary deformation potentials and elastic constants, given in Table 19 and Table 20, are linearly interpolated. The bandgap of strained InAsSbBi is

$$E'_{g,InAsSbBi}(x,y,\varepsilon_{xx}) = (1-x-y)E_{g,InAs} + yE_{g,InSb} + xE_{g,InBi} - y(1-y)b_{g,InAsSb} - x(1-x)b_{g,InAsBi,0}e^{-x/x_a} + \Delta E_g(x,y,\varepsilon_{xx}) \,, \quad (50)$$

where $\Delta E_g(x,y,\varepsilon_{xx})$ is the change in bandgap energy due to strain. The strained bandgap energy of the complementary alloy GaAsSbBi obeys the same Eq. 50.

The low temperature (0 K) strained bandgap of InAsSbBi is shown as a function of Sb mole fraction in Fig. 36 with contours of constant strain and Bi mole fraction. The quaternary bandgap bowing model and ternary bowing coefficients summarized in Table 19 are anchored by experimental measurements of the bandgap energy of InAs, lattice matched InAsSb,[5] and nearly lattice matched $InAs_{0.936}Bi_{0.064}$.[4] For InAsSbBi lattice matched to GaSb, the bandgap ranges from 0.324 eV (3.8 μm) for $InAs_{0.911}Sb_{0.089}$ to 0.104 eV (11.9 μm) for $InAs_{0.932}Bi_{0.068}$ at low temperature, and from 0.277 eV (4.5 μm) to 0.048 eV (25.8 μm) at room temperature (not shown), which is about a 50 meV reduction in bandgap energy at room temperature. For GaAsSbBi lattice matched to GaSb, the bandgap ranges from 0.812 eV (1.5 μm) for GaSb to 0.147 eV (8.4 μm) for $GaAs_{0.106}Sb_{0.694}Bi_{0.200}$ at low temperature, and from 0.729 eV (1.7 μm) to 0.079 eV (15.6 μm) at room temperature (not shown).

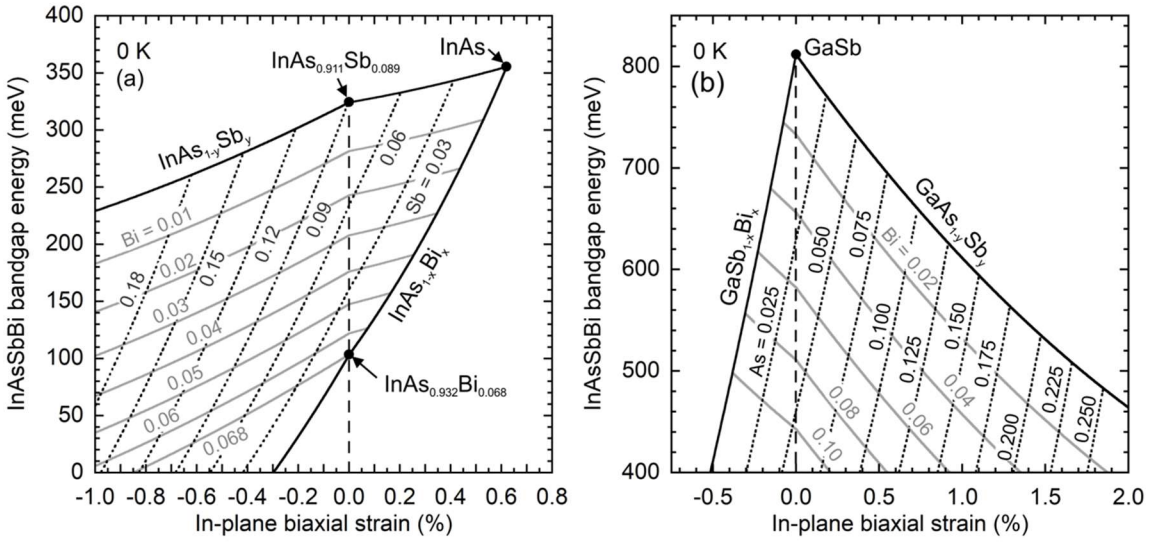

FIG. 36. Low-temperature bandgap of (a) InAsSbBi on GaSb and (b) GaAsSbBi on GaSb versus in-plane biaxial strain. Constant Bi mole fraction contours are shown as solid grey lines and constant in-plane strain contours as black dashed lines. The heavy dashed line indicates lattice matched material. The InAsSb, InAsBi, GaAsSb, and GaSbBi ternary boundaries are shown as solid black lines.

Design of devices such as IR detectors and lasers requires both electrical (i.e. carrier) and optical confinement. Electrical confinement in turn is a product of the conduction and valence band lineup between materials in heterostructure devices. InAs strained to the GaSb lattice constant suffers from a disadvantageous broken type-II band alignment with most III-V compounds, including the GaSb substrate.[9] Strain lifts the valence band degeneracy and the heavy (light) hole band edge offset of biaxially strained InAs is 0.578 eV (0.531 eV) below the GaSb valence band edge. Likewise, lattice matched InAsSb exhibits a valence band edge offset of -0.477 eV relative to GaSb.[9] Achievement of adequate hole confinement is the chief challenge for device designs utilizing InAsSbBi as

an infrared active layer, a fact illustrated by the band alignments of lattice matched InAsSbBi, GaAsSbBi, AlGaAsSb, and InGaAsSb in Fig. 37. Bi incorporation tends to push the valence band edges of both InAsSbBi and GaAsSbBi upwards in energy due to the band anti-crossing interaction between localized Bi 6p orbitals and the host band structure.[6] However Bi incorporation in lattice matched InAsSbBi is insufficient to achieve a type-I band alignment with other lattice matched quaternary alloys. The type-II band alignment persists even for a hypothetical heterostructure of endpoint ternary compounds $InAs_{0.932}Bi_{0.068}$ / $AlAs_{0.084}Sb_{0.916}$.

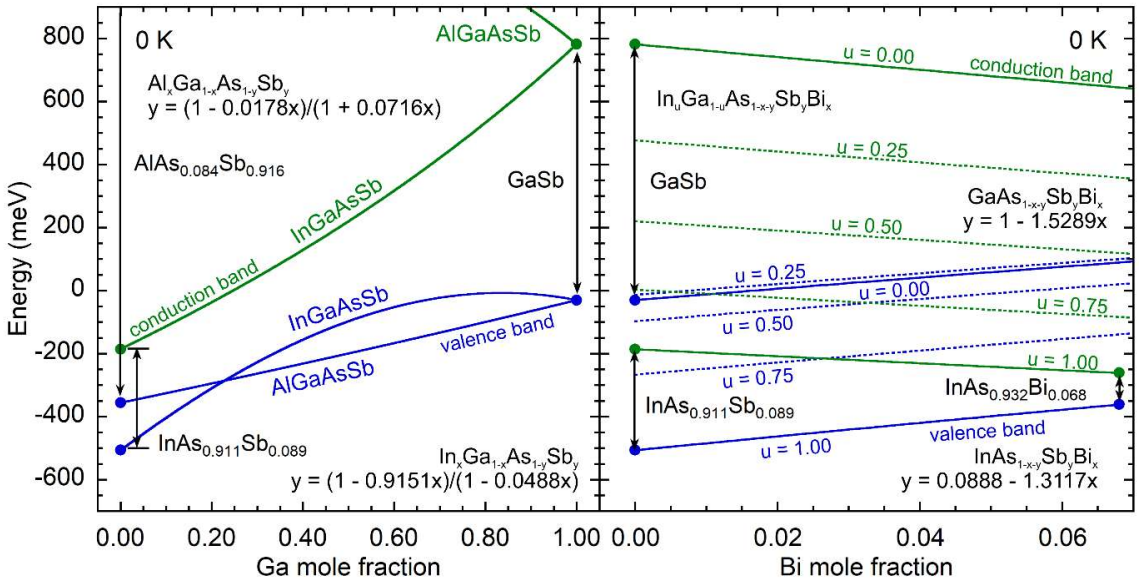

FIG. 37. Conduction band edge (green) and valence band edge (blue) as a function of Ga mole fraction in GaInAsSb/AlGaAsSb (left) and Bi mole fraction in GaInAsSbBi (right). All compounds are lattice matched to GaSb. Inspection of the GaInAsSbBi valence band offsets relative to suitable optical cladding layers such as AlGaAsSb reveals that type-I band alignments are achieved by incorporating both Bi and Ga in the quinary alloy.

One method to achieve adequate hole confinement for mid/long wave IR heterostructure designs at the GaSb lattice constant is to utilize the quinary alloy GaInAsSbBi. Fig. 37 shows the band offsets of lattice matched GaInAsSbBi and illustrates the importance of incorporating both Bi and Ga to achieve a type-I band alignment with GaSb. Incorporation of both elements adds an additional degree of design freedom and raises the InAsSb valence band offset higher in energy with respect to the AlGaAsSb or InGaAsSb barriers, indicated by the constant-Ga contours and Bi mole fraction dependence at right. Ga mole fraction provides a coarse control over band offsets while Bi mole fraction allows the designer to fine-tune the band structure and optimize electron-hole wavefunction overlap to unity in the quantum well, thereby maximizing the radiative recombination rate. By incorporating Al in the barriers it is possible to move the valence band edge lower in energy and thus achieve type-I band alignment with InAsSb-based alloys using smaller Ga and Bi mole fractions.

The bandgap energy of $Ga_{1-u}In_uAs_{1-x-y}Sb_yBi_x$ is modeled by linearly interpolating the six constituent binary compounds with the bowing terms of each of the nine possible ternary compounds:

$$E_g(u,x,y) = uzE_{g,InAs} + uyE_{g,InSb} + uxE_{g,InBi} + vzE_{g,GaAs} + vyE_{g,GaSb} + vxE_{g,GaBi} - uzyb_{g,InAsSb} - uzxb_{g,InAsBi} - uxyb_{g,InSbBi} - vzyb_{g,GaAsSb} - vzxb_{g,GaAsBi} - vxyb_{g,GaSbBi} - uvzb_{g,InGaAs} - uvyb_{g,InGaSb} - uvxb_{g,InGaBi}, \quad (51)$$

where $v = 1 - u$ and $z = 1 - x - y$. The bandgap and band edge energy shift due to strain is modeled by linearly interpolating the binary deformation potentials. The bandgap bowing for pseudomorphic GaInAsSbBi lattice matched to GaSb is shown below in Fig. 38.

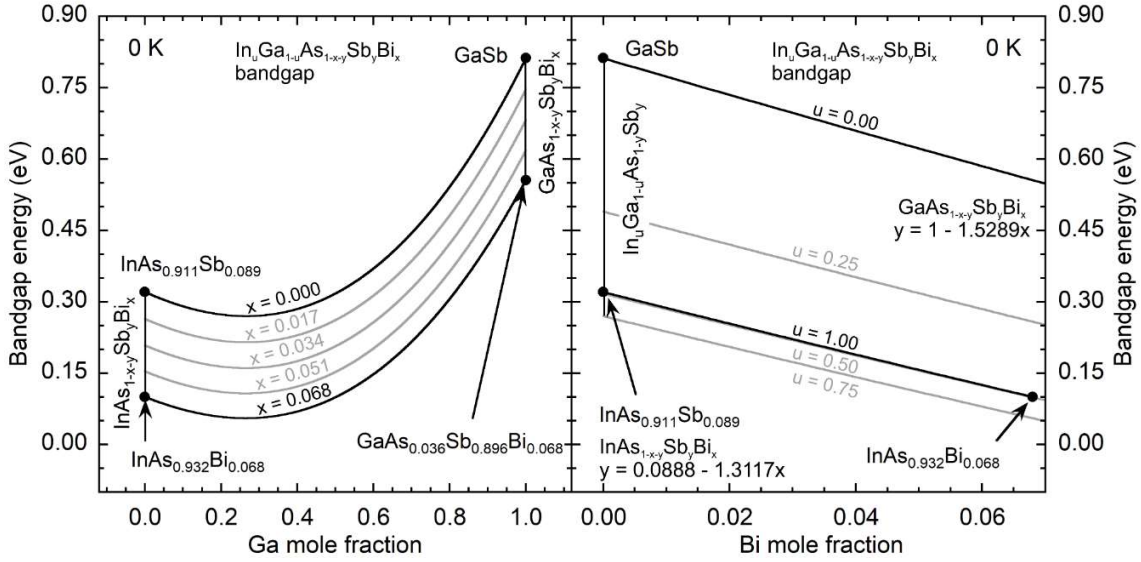

FIG. 38. Bandgap energy of lattice matched GaInAsSbBi as a function of Ga mole fraction (left) and Bi mole fraction (right). Composition equations for lattice matched bismide quaternaries InAsSbBi and GaAsSbBi are shown at right. There is little bowing with Bi over the range $0 \leq x \leq 6.8\%$ and strong bandgap bowing is observed for the group III mole fraction.

5: III-V-Bi ACTIVE LAYER DESIGN FOR MID-IR LASERS

The III-V-bismide alloys are suitable candidates for the active region of mid-IR lasers operating in the 3-5 μm wavelength range and beyond. Different laser designs exist including edge-emitting lasers and vertical cavity surface-emitting lasers (VCSELs), however all share the requirement for a high quantum efficiency gain medium emitting at the desired laser wavelength. An effective semiconductor laser design must meet four basic requirements:

1. An active region or gain medium where carriers recombine radiatively by stimulated emission. The nonradiative losses (e.g. Shockley-Read Hall and Auger recombination) in this layer must be held to a minimum in order to maximize internal quantum efficiency of the device.[122] This active region often takes the form of a multiple quantum well, where the individual wells do not interact with each other.
2. Electrical confinement for the electrons and holes injected into the active region. Suitable barrier materials at the GaSb lattice constant include AlGaAsSb, InGaAsSb, or simply GaSb. A type-I band alignment between the active region prevents carriers from diffusing from the active region and recombining in the barriers.
3. Optical confinement for the stimulated emission from the laser. Practically this means that the refractive index of the active region must be lower than the refractive index of the barrier regions to ensure total internal reflection and high rates of stimulated emission.

4. Doped n-type and p-type regions to inject carriers into the active region under external electrical bias.

As discussed in Chapter 1, the quinary alloy GaInAsSbBi is suitable as the well material in mid-IR quantum wells as it is possible to achieve the required type-I band alignment with common barrier materials such as AlGaAsSb or GaSb. Further, the three degrees of design freedom afforded by a quinary alloy permits the designer to manipulate the conduction and valence band offsets independently of the desired bandgap energy and strain. It is thereby possible to design quantum wells in which the electron and hole wavefunctions for bound states in the well overlap completely. The radiative recombination rate is directly proportional to the electron-hole wavefunction overlap integral squared.[15] Unity wavefunction overlap represents a design with the maximum achievable radiative recombination rate and is therefore termed an "optimal" quantum well. Lattice matched GaInAsSbBi / AlGaAsSb optimal quantum wells as laser active region/gain medium are designed using the following algorithm:

1. Select desired quantum well strain/lattice mismatch.
2. Select desired AlGaAsSb barrier composition ($Al_{0.35}Ga_{0.65}As_{0.03}Sb_{0.97}$ or GaSb considered here).
3. Select Ga mole fraction to achieve preferred hole confinement.
4. Select desired quantum well emission wavelength (ground state transition energy) by adjusting the Bi mole fraction.
5. Iterate steps 3 and 4 until desired emission wavelength and unity electron-hole confinement (wavefunction overlap) is achieved.

Compressive strain in the GaInAsSbBi quantum well can aid the task of achieving a type-I band alignment with the AlGaAsSb barrier. As illustrated in Fig. 39, in a compressively strained GaInAsSbBi layer the conduction and heavy hole band edge both move up in energy, making it possible to achieve type-I band alignments with smaller Ga and Bi mole fractions than if only lattice matched material is considered. Compressive strain as high as 2%, corresponding to a Matthews-Blakeslee critical thickness of 9.5 nm, is considered for practical quantum well designs.

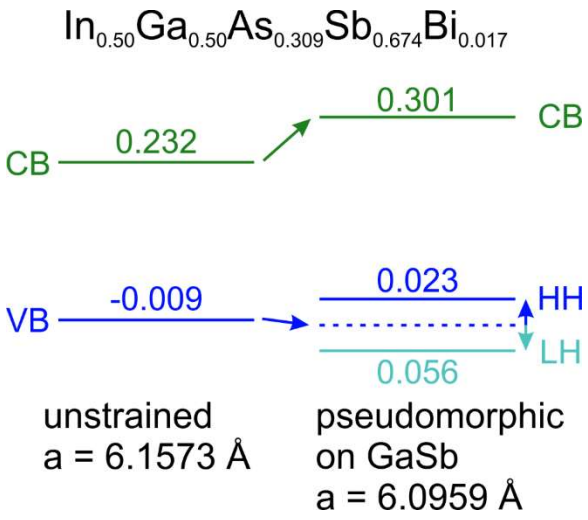

FIG. 39. Effect of 1% compressive biaxial strain on the band edge position of GaInAsSbBi.

Several practical edge-emitting mid-IR laser active layer designs are proposed. The designs cover the wavelength range of 3.5 – 5.0 µm at low temperature (4.0 – 5.9 µm at room temperature) and employ the same basic structure with a GaInAsSbBi quantum well gain medium and AlGaAsSb cladding layers.

In the 3.5 µm laser active region designs, a typical edge emitter laser cross-section[122] is selected with 2000 nm thick AlGaAsSb cladding layers with 200 nm thick graded index

layers on either side, and a 600 nm thick wave guide region. The graded layers offer improved conductivity with lower doping in the waveguide region. These layer thicknesses are typical for this type of mid IR laser and can be adjusted for optimal optical confinement to a given active region via simulations. The active region consists of three quantum wells designed for an emission wavelength of 3.50 μm at low temperature; the resulting longer room-temperature emission wavelength varies slightly with design and is found to be a little over 4 μm. The quantum well barriers are chosen to be 20 nm thick, for which there is no coupling between the quantum wells. Uncoupled wells can suffer from non-uniform electron and hole injection, and while reducing the barrier thickness improves injection uniformity, it also results in broadening of the emission levels. The barrier thickness may be optimized experimentally.

Laser Design A with lattice matched $Al_{0.35}Ga_{0.65}As_{0.03}Sb_{0.97}$/ $Ga_{0.55}In_{0.45}As_{0.407}Sb_{0.573}Bi_{0.020}$/ $Al_{0.35}Ga_{0.65}As_{0.03}Sb_{0.97}$ quantum wells is shown below in Fig. 40. The index of refraction profile is shown along with the band edge cross-section. Details of the quantum well band offsets, the quantum-confined energy states, and the electron and heavy hole wavefunctions are shown at low temperature in Fig. 41. The room temperature emission wavelength for Laser Design A is 4.23 μm.

The band offsets are chosen so that electron and heavy hole wavefunctions have equal confinement and hence near unity wavefunction overlap. The confinement is determined by the well potential profile and the carrier effective mass. Since the heavy hole mass is about an order of magnitude greater than the electron, its potential well can be much smaller for the same confinement. Additionally, while the emission wavelength changes significantly with temperature, the electron-hole wavefunction overlap does not.

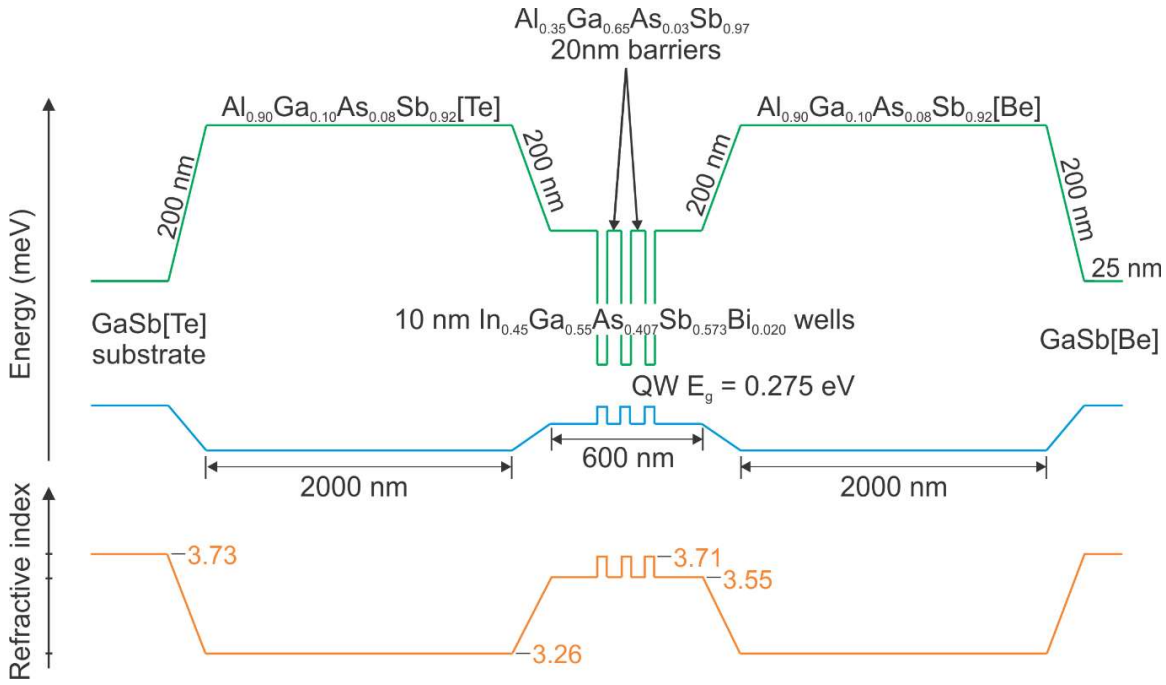

FIG. 40. Laser Design A band offsets (upper) and refractive index (lower).

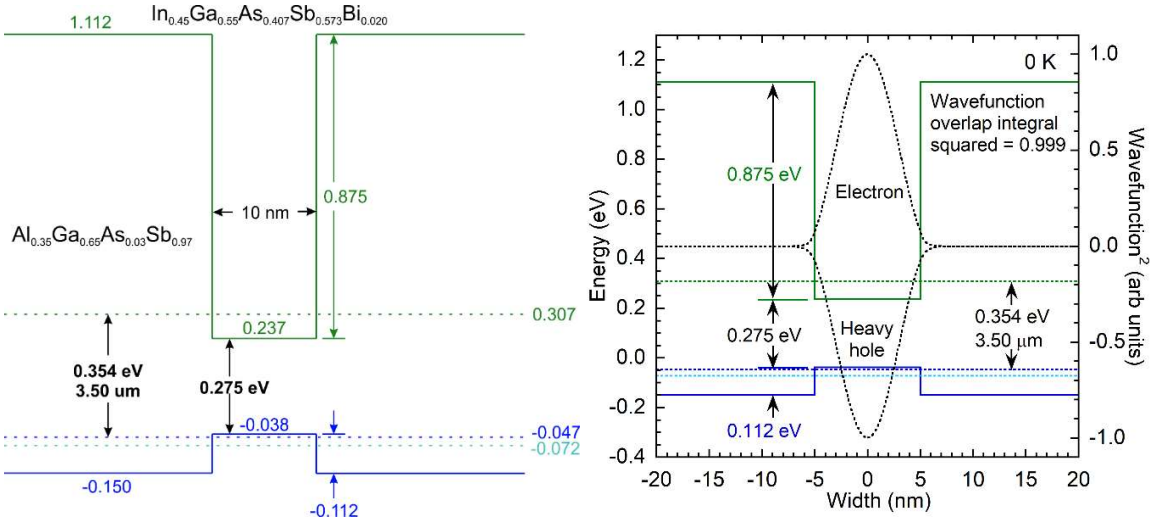

FIG. 41. Laser Design A quantum well at low temperature with 0.354 eV (3.50 um) ground state transition energy and 0.999 wavefunction overlap integral squared.

Laser Design B utilizes GaSb/$Ga_{0.35}In_{0.65}As_{0.293}Sb_{0.704}Bi_{0.003}$/GaSb quantum wells that have 2% compressive strain. By increasing the Ga mole fraction and compressive strain in the well, a type-I band alignment with GaSb is achieved. Hole confinement is sufficient for unity wavefunction overlap at 3.5 μm emission wavelength. Optical performance is equivalent to Laser Design A which utilized AlGaAsSb quantum well barriers rather than simply GaSb. It is attractive to use binary compounds wherever possible in III-V device design due to the relaxed growth constraints and higher material quality. This laser design demonstrates the flexibility and value that the bismide quinary alloy InGaAsSbBi offers to the device designer.

The band edge cross-section and index of refraction profile of Laser Design B is shown below in Fig. 42. Details of the quantum well band offsets, the quantum-confined energy levels, and the electron and heavy hole wavefunctions are shown at low temperature in Fig. 43. The room temperature emission wavelength is 4.02 μm.

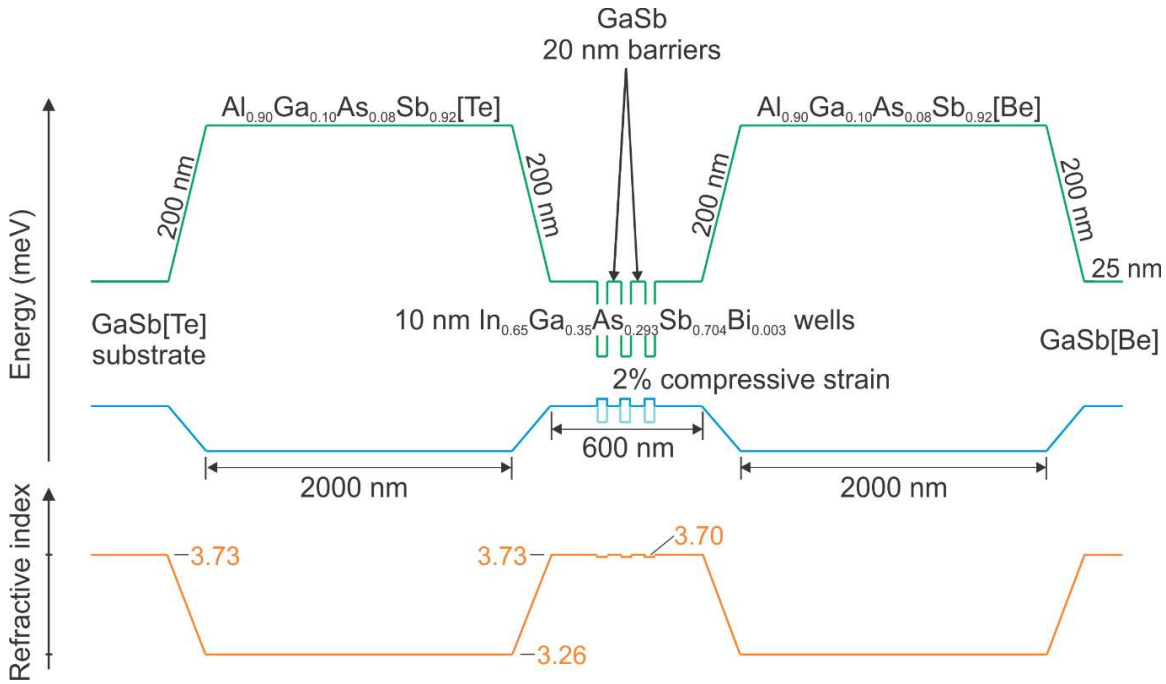

FIG. 42. Laser Design B band offsets (upper) and refractive index (lower).

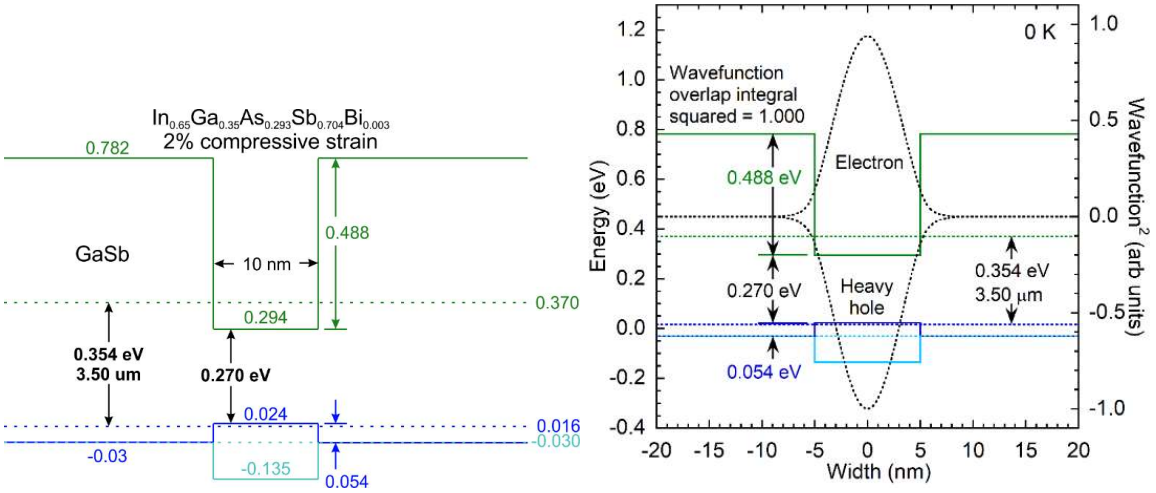

FIG. 43. Laser Design B quantum well at low temperature with 0.354 eV (3.50 um) ground state transition energy and 0.999 wavefunction overlap integral squared.

Laser Design C is a 5 μm laser utilizing GaSb/$Ga_{0.3}In_{0.7}As_{0.347}Sb_{0.627}Bi_{0.026}$/GaSb quantum wells that have 2% compressive strain. This laser design is an adaption of Laser

Design B to a longer emission wavelength of 5 μm, the long wavelength limit of the mid-IR atmospheric transmittance window.[123] Adjustment of the Ga and Bi mole fractions changes the emission wavelength while maintaining proper electron and hole confinement for unity wavefunction overlap. This is an attractive feature for growth of GaInAsSbBi lasers as devices with widely varying emission wavelengths can be fabricated under identical MBE growth conditions simply by varying the atomic fluxes during well growth.

The band edge cross-section and index of refraction profile of Laser Design C is shown below in Fig. 44. Details of the quantum well band offsets, the quantum-confined energy levels, and the electron and heavy hole wavefunctions are shown at low temperature in Fig. 45. The room temperature emission wavelength is 5.94 μm

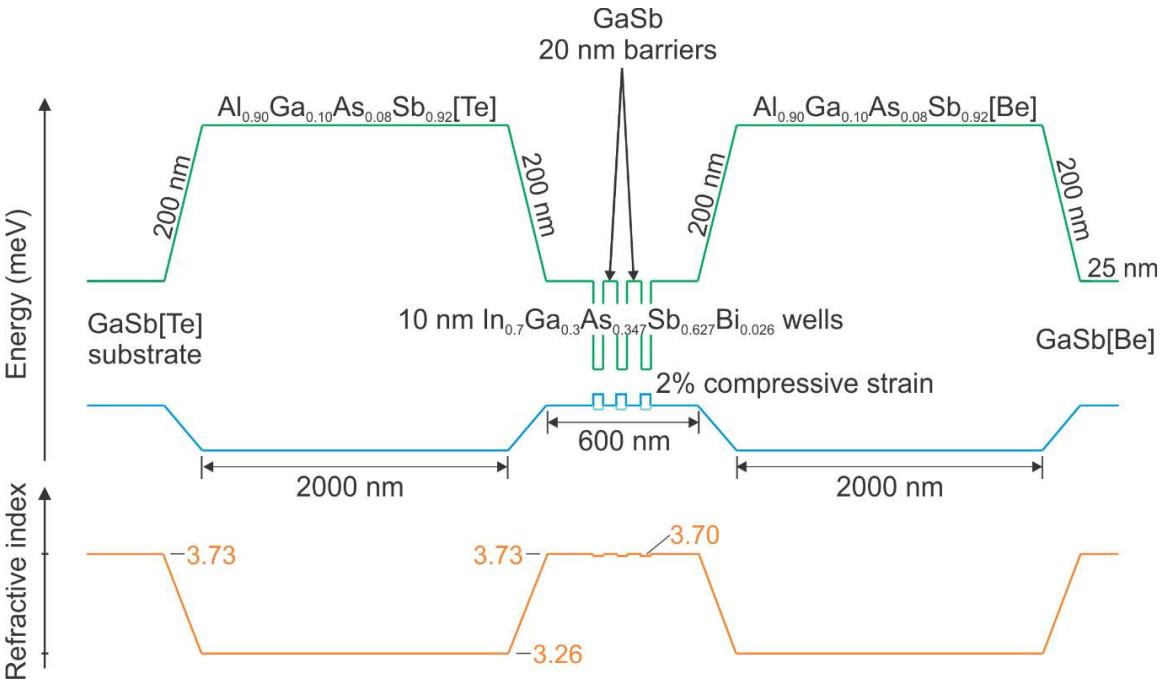

FIG. 44. Laser Design C band offsets (upper) and refractive index (lower).

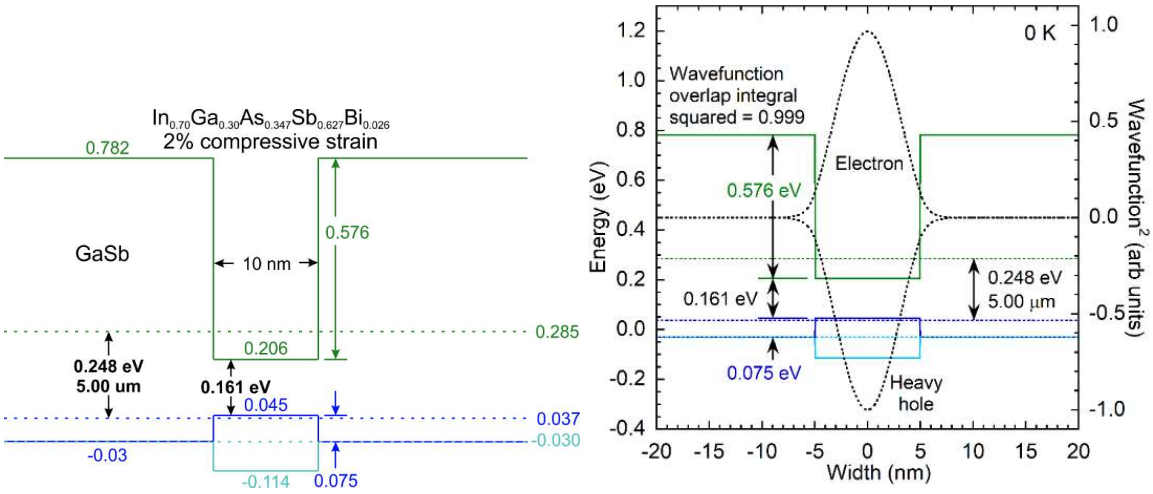

FIG. 45. Laser Design C quantum well at low temperature with 0.248 eV (5.00 um) ground state transition energy and 0.999 wavefunction overlap integral squared.

6: CONCLUSIONS

Optoelectronic devices such as LEDs, lasers, and photodetectors operating in the infrared are required for medical imaging and diagnostics, autonomous vehicle sensors, telecommunications, and gas sensing among other applications. Extending the performance of III-V semiconductors into the mid-wave and long-wave infrared is expected to yield improvements to the performance, manufacturing cost, and sustainability of the compound semiconductors that compose these optoelectronic devices. III-V alloys incorporating bismuth are attractive materials due to their highly tunable bandgap energies and the availability of large area lattice matched substrates such as GaSb and InAs. Utilizing quaternary or even quinary III-V-bismide alloys provides materials designers with additional degrees of freedom which may be used to tune band alignments for desired optical and electrical properties.

Bulk and quantum well InAsSbBi samples are grown on on-axis and offcut (100) GaSb substrates by molecular beam epitaxy at growth temperatures ranging from 400 to 430 °C. The molecular beam epitaxy growth of InAsSbBi is strongly influenced by growth temperature and the As flux. For growth temperatures above 360 °C, Bi incorporation decreases exponentially with a characteristic temperature of about 21 °C. The presence of a Bi flux changes the (2×3) Sb-terminated surface to a (2×4) or (2×1) Bi-mediated surface, confirming the highly surface-active nature of Bi. Near stoichiometric As fluxes are employed to aid Bi incorporation, but result in the accumulation of Bi on the surface that coalesces into Bi-rich surface droplets. Arsenic fluxes a few percent greater than stoichiometry result in smooth droplet-free surfaces, indicating that excess As aids in the desorption of excess Bi from the growth surface.

A molecular beam epitaxy growth model based on the kinetics of Bi adsorption, desorption, incorporation, surface accumulation, and droplet formation is applied to the growth of nearly lattice matched InAsSbBi on GaSb. A solution for steady state growth is derived and the model parameters are fit to experimentally measured Bi, Sb, and As mole fractions for bulk and quantum well samples grown at 400 °C and 420 °C. The Bi mole fractions predicted by the model agree to within uncertainty with the measured mole fractions. As the growth temperature is increased from 400 °C to 420 °C, the Bi incorporation rate decreases by a factor of 3.8 and the Bi self-desorption rate increases by a factor of 1.7. The characteristic temperatures for Bi incorporation, desorption, and droplet uptake are 14.9 °C, 36.8 °C, and 7.9 °C respectively. The net result is a reduction of Bi mole fraction for growth at higher temperature. The model indicates that the Bi surface coverage is directly proportional to the Bi/In flux and decreases as As/In flux increases.

The removal of surface Bi by surface As and the exchange of incorporated Bi with surface As dominates the growth process with associated probabilities of 70% and 78% respectively. The reverse processes involving As and Bi are negligible with associated probabilities of 3.3% and 0.15% respectively. The As-assisted removal of Bi from the surface results in a reduced fraction of Bi on the surface and a reduced likelihood of Bi-rich droplet formation. Furthermore, a growth temperature dependent threshold for the excess As flux required for droplet-free InAsSbBi growth is identified as $\geq$ 2.0% and $\geq$ 1.2% for growth at 400 °C and 420 °C, respectively.

The removal of surface Bi by surface Sb and the exchange of incorporated Bi with surface Sb is smaller with probabilities of 44% and 20% respectively. The reverse

processes involving Sb and Bi are similar in size with associated probabilities of 45% and 12% respectively. As such, Sb plays a much smaller role in limiting the incorporation of Bi. The removal of surface Sb by surface As and the exchange of incorporated Sb with surface As is also significant in the growth process with associated probabilities of 66% and 21% respectively. The reverse processes involving As and Sb are smaller with associated probabilities of 7.3% and 2.7% respectively.

The model predicts that the ultimate achievable Bi mole fractions for growth of InAsSbBi lattice-matched to GaSb are 1.43% and 0.30% for growth at 400 °C and 420 °C respectively. The characteristic temperature of this ultimate Bi mole fraction limit is 12.9 °C, indicating that the growth temperature must be reduced to ≤ 385 °C to obtain the lattice-matched ternary alloy $InAs_{0.932}Bi_{0.068}$ on GaSb. The growth model provides a useful tool for the design and implementation of optimized molecular beam epitaxial growth conditions for Bi-containing III-V alloys with a desired chemical composition and high optical quality.

The intrinsic absorption edge of binary compounds GaAs, GaSb, InAs, and InSb is examined and a model is developed to describe the experimentally observed features, such as the Urbach tail, the bandgap energy, and the magnitude of the absorption at the bandgap. The description includes the Urbach parameter that depicts exponentially decreasing absorption due to localized tail states, the bandgap energy extrapolated from the above-bandgap absorption, and the enhancement of the absorption strength at the bandgap due to the Coulomb interaction. GaAs, GaSb, and InAs exhibit behavior consistent with approximately parabolic band structure and constant dipole matrix element; by contrast, InSb indicates approximately constant transition strength.

The room-temperature (297 K) bandgap energy and Urbach energy bandgap energy is measured as 1.4179 ± 0.0002 eV and 8.69 ± 0.06 meV for GaAs, 0.7304 eV and 13.98 meV for GaSb, 0.3552 eV and 12.91 meV for InAs, and 0.1803 eV and 10.70 meV for InSb. The GaAs bandgap energy obtained from model fitting is compared with band gap energy obtained by the first derivative maximum method. The bandgap energy obtained from model fitting is more consistent than the first derivative maximum energy, with smaller relative error. The GaAs bandgap energy fitted by the absorption model agrees closely with the peak values of the refractive index and real dielectric function, suggesting that these peak values are more accurate for determining bandgap energy than first derivative maximum.

The nonradiative lifetime of the lattice matched ternary alloy $InAs_{0.911}Sb_{0.089}$ is determined from temperature and excitation density dependent photoluminescence measurements. This experimental approach provides an absolute measurement of all three recombination mechanisms (SRH, radiative, and Auger) from only photoluminescence measurements. The radiative recombination lifetime of bulk $InAs_{0.911}Sb_{0.089}$ is 2.0 - 309 ns in the temperature range 15 K to 295 K, a variation of over 2 orders of magnitude. This reduction in the radiative recombination coefficient is a consequence of the decreasing chemical potential and is the dominant mechanism contributing to reduced photoluminescence intensity at elevated temperatures. The SRH lifetime of bulk $InAs_{0.911}Sb_{0.089}$ is 8.5 – 290 ns in the temperature range 15 K to 295 K and the Auger recombination coefficient is 5.1×10^{-26} cm^6 s^{-1} in the temperature range 50 K to 250 K. It is apparent that the temperature dependence of the SRH lifetime is the dominant nonradiative effect leading to the reduction in quantum efficiency at elevated temperatures.

The Auger recombination coefficient C increases only for temperatures below 50 K and above 250 K, while the SRH recombination coefficient A increases over two orders of magnitude across the temperature range 15 K – 295 K. The increase in the Auger coefficient at low temperatures is likely due to an increase in carrier concentration while the increase at high temperatures may be due to the smaller bandgap energy. The increase in SRH recombination rates with temperature may be attributed to the higher thermal energy of carriers and attendant increase in carrier diffusion to SRH recombination centers.

The total recombination lifetime, which relates the photoexcitation rate to the carrier concentration in this steady-state measurement, decreases rapidly with temperature up to approximately 70 K. This decrease is driven primarily by the radiative lifetime. Conversely, the increase in total lifetime for elevated temperatures is a consequence of decreasing carrier occupation due to the rapidly increasing effective density of states.

The quaternary alloy InAsSbBi samples are examined using temperature and excitation dependent photoluminescence measurements. The low-temperature bandgap energy determined from photoluminescence and the in-plane strain determined from X-ray diffraction are used to determine the InAsSbBi alloy composition of each sample. The Bi mole fractions range from about 0.2% to 1.9% and are largely independent of surface morphology. The effects of alloy broadening are quantified by the width of the photoluminescence lineshape. The temperature dependence of the width is approximately linear, with a constant offset corresponding to a "frozen-in" low-temperature value of about 2 meV due to Sb alloy broadening and larger component of about 3 to 10 meV due to Bi alloy broadening as a result of Bi mole fraction fluctuations and localized states near the band edges arising from Bi pairing and clustering.

A bandgap and band edge model as a function of Sb and Bi mole fraction and temperature is established for InAsSbBi and GaAsSbBi. The overall bandgap bowing and individual band edge bowing is based on the constituent ternary bowing parameters, where the InAsBi bowing is modeled using a Bi mole fraction dependent bowing coefficient that approximates the valence band anti-crossing expression for the InAsBi valence band edge up to 6.4% Bi. The InSbBi bandgap bowing coefficient is assumed to be equal to the sum of InAsSb and InAsBi bowing coefficients for these dilute Bi mole fractions. The temperature dependence of the InAsSbBi bandgap is modeled using an Einstein single oscillator equation fit to the temperature dependent bandgaps of the InAsSbBi samples.

The extra degrees of design freedom afforded by quinary III-V-bismide alloys such as GaInAsSbBi are used to design optimal type-I quantum wells with unity electron-hole wavefunction overlap. Such optimal quantum wells are expected to yield improved radiative recombination rates and quantum efficiency. A quantum well design algorithm for arbitrarily selected wavelength, well thickness, and strain is presented. This algorithm is used to design GaInAsSbBi/AlGaAsSb quantum wells operating in the 3-5 μm range. Practical edge-emitting mid-IR laser active layer designs based on the optimal quantum well designs are presented.

REFERENCES

1 S. T. Schaefer, R. R. Kosireddy, P. T. Webster, and S. R. Johnson, "Molecular beam epitaxy growth and optical properties of InAsSbBi", J. Appl. Phys. **126**, 083101 (2019).

2 P. T. Webster, A. J. Shalindar, S. T. Schaefer, and S. R. Johnson, "Bandgap and composition of bulk InAsSbBi grown by molecular beam epitaxy", Appl. Phys. Lett. **111**, 082104 (2017).

3 J. W. Matthews and A. E. Blakeslee, "Defects in epitaxial multilayers: I. Misfit dislocations", J. Crystal Growth **27**, 18-125 (1974).

4 P. T. Webster, A. J. Shalindar, N. A. Riordan, C. Gogineni, H. Liang, A. R. Sharma, and S. R. Johnson, "Optical properties of InAsBi and optimal designs of lattice-matched and strain balanced III-V semiconductor superlattices", J. of Appl. Phys. **119**, 225701 (2016).

5 P. T. Webster, N. A. Riordan, S. Liu, E. H. Steenbergen, R. A. Synowicki, Y.-H. Zhang, and S. R. Johnson, "Measurement of InAsSb bandgap energy and InAs/InAsSb band edge positions using spectroscopic ellipsometry and photoluminescence spectroscopy", J. of Appl. Phys. **118**, 245706 (2015).

6 K. Alberi, J. Wu, W. Walukiewicz, K. M. Yu, O. D. Dubon, S. P. Watkins, C. X. Wang, X. Liu, Y.-J. Cho, and J. Furdyna, "Valence-band anticrossing in mismatched III-V semiconductor alloys", Phys. Rev. B **75**, 045203 (2007).

7 M. K. Rajpalke, W. M. Linhart, K. M. Yu, T. S. Jones, M. J. Ashwin, and T. D. Veal, "Bi flux-dependent MBE growth of GaSbBi alloys", J. Cryst. Growth **425**, 241 (2015).

8 A. P. Roth, W. J. Keeler, and E. Fortin, "Photovoltaic effect and temperature dependence of the energy gap in the $In_{1-x}Ga_xSb$ alloy system", Can. J. Phys. **58**, 560 (1980).

9 I. Vurgaftman, J. R. Meyer, and L. R. Ram-Mohan, J. Appl. Phys., "Band parameters for III–V compound semiconductors and their alloys", Vol. 89, No. 11 (2001).

10 M. V. Kurik, "Urbach Rule", Phys. Status Solidi A **8**, 9 (1971).

11 S. R. Johnson and T. Tiedje, "Temperature dependence of the Urbach edge in GaAs", J. Appl. Phys. **78**, 5609 (1995).

12 M. Beaudoin, A. J. G. DeVries, S. R. Johnson, H. Laman, and T. Tiedje, "Optical absorption edge of semi-insulating GaAs and InP at high temperatures", Appl. Phys. Lett. **70**, 26 (1997).

13 V. K. Malyutenko and V. I. Chernyakhovsky, "Thermal emission of InAs induced by band tails", Semicond. Sci. Technol. **9**, 1047-1049 (1994).

14 R. J. Elliott, "Intensity of Optical Absorption by Excitons", Phys. Rev. **108**, 1384 (1957).

15 S. L. Chuang, Physics of Optoelectronic Devices (John Wiley & Sons, Inc, New York, 1995).

16 J. S. Blakemore, "Semiconducting and other major properties of gallium arsenide", J. Appl. Phys. **53**, R123 (1982).

17 Y. H. Lee, A. Chavez-Pirson, S. W. Koch, H. M. Gibbs, S. H. Park, J. Morhange, A. Jeffery, and N. Peyghambarian, "Room-temperature optical nonlinearities in GaAs", Phys. Rev. Lett. **57**, 2446 – 2449 (1986).

18 A. R. Beattie and P. T. Landsberg, "Auger Effect in Semiconductors", Proc. R. Soc. A **249**, 16-29 (1958).

19 A. Haug, "Auger recombination in direct-gap semiconductors: band-structure effects", J. Phys. C: Solid State Phys. **16**, 4159 (1983).

20 W.-X. Ni, W. M. Chen, I. A. Buyanova, A. Henry, G. V. Hansson, B. Monemar, "Some critical issues on growth of high quality Si and SiGe films using a solid-source molecular beam epitaxy system", J. Cryst. Growth **157**, 242 (1995).

21 M. H. Chan, S. K. So, K. T. Chan, F. G. Kellert, "Defect density measurements of low temperature grown molecular beam epitaxial GaAs by photothermal deflection spectroscopy", Appl. Phys. Lett. **67**, 834 (1995).

22 L. L. Anisimova, A. K. Gutakovskii, I. V. Ivonin, V. V. Preobrazhenskii, M. A. Putyato, B. R. Semyagin, and S. V. Subach, "Defect formation in LT MBE InGaAs and GaAs", J. Struct. Chem. **45**, Supplement, pp. S96-S102, (2004).

23 Y. Horikoshi, M. Kawashima, and H. Yamaguchi, "Migration-enhanced epitaxy of GaAs and AlGaAs", Jap. J. Appl. Phys. **27**, 169-179 (1988).

24 A. Y. Cho, "Growth of III-V semiconductors by molecular beam epitaxy and their properties", Thin Film Solids **100**, 291-317 (1983).

25 C. B. Alcock, V. P. Itkin, and M. K. Horrigan, "Vapour pressure equations for the metallic elements: 298-2500K", Canadian Metallurgical Quarterly **23**, 309 (1984).

26 A. J. Shalindar, P. T. Webster, B. J. Wilkens, T. L. Alford, and S. R. Johnson, "Measurement of InAsBi mole fraction and InBi lattice constant using Rutherford

backscattering spectrometry and X-ray diffraction", J. Appl. Phys. **120**, 145704 (2016).

27 P. T. Webster, N. A. Riordan, C. Gogineni, S. Liu, J. Lu, X.-H. Zhao, D. J. Smith, Y.-H. Zhang, and S. R. Johnson, "Molecular beam epitaxy using bismuth as a constituent in InAs and a surfactant in InAs/InAsSb superlattices", J. Vac. Sci. Technol. B **32**(2) (2014).

28 P. T. Webster, S. T. Schaefer, E. H. Steenbergen, and S. R. Johnson, "Optical quality in strain-balanced InAs/InAsSb superlattices grown with and without Bi surfactant", Proc. SPIE 10540, Quantum Sensing and Nano Electronics and Photonics XV, 105401E (2018).

29 C. H. Macgillavry and G. D. Rieck, International Tables for Crystallography (The Kynoch Press, Birmingham, England, 1968).

30 Z. R. Wasilewski, M. M. Dion, D. J. Lockwood, P. Poole, R. W. Streater, and A. J. SpringThorpe, "Composition of AlGaAs", J. Appl. Phys. **81**, 1683 (1997).

31 L. Vegard, "Die Konstitution der Mischkristalle und die Raumfüllung der Atome," Z. Phys. **5**, 17–26 (1921).

32 Rutherford Backscattering Spectrometry Analysis Package, Genplot, Cortland, OH.

33 L. J. van IJzendoorn, M.J.A. de Voigt, and J.W. Niemantsverdriet, "Materials analysis with Rutherford Backscattering Spectrometry: Application to catalysts", React. Kinet. Catal. Lett. **50**, 1-2, 131-137 (1993).

34 R. R. Kosireddy, S. T. Schaefer, A. J. Shalindar, and S. R. Johnson, "Microstructure and surface morphology of InAsSbBi grown by molecular beam epitaxy", J. Appl. Phys. **126**, 095108 (2019).

35 C. R. Tait and J. M. Millunchick, "Kinetics of droplet formation and Bi incorporation in GaSbBi alloys", J. Appl. Phys. **119**, 215302 (2016).

36 S. Tixier, M. Adamcyk, T. Tiedje, S. Francoeur, A. Mascarenhas, P. Wei, and F. Schiettekatte, "Molecular beam epitaxy growth of GaAs(1-x)Bi(x)", Appl. Phys. Lett. **82**, 2245 (2003).

37 K. Y. Ma, Z. M. Fang, R. M. Cohen, and G. B. Stringfellow, "OMVPE growth and characterization of Bi-containing III-V alloys", J. Cryst. Growth **107**, 416-421 (1991).

38 X. Lu, D. A. Beaton, R. B. Lewis, T. Tiedje, and M. B. Whitwick, "Effect of molecular beam epitaxy growth conditions on the Bi content of GaAs(1-x)Bi(x)," Appl. Phys. Lett. **92**(19), 192110 (2008).

39 E. C. Young, S. Tixier, and T. Tiedje, "Bismuth surfactant growth of the dilute nitride GaN(x)As(1-x)", J. Cryst. Growth **279**, 316 (2005).

40 R. B. Lewis, M. Masnadi-Shirazi, and T. Tiedje, "Growth of high Bi concentration GaAs(1-x)Bi(x) by molecular beam epitaxy," Appl. Phys. Lett. **101**(8), 082112 (2012).

41 P. T. Webster, N. A. Riordan, S. Liu, E. H. Steenbergen, R. A. Synowicki, Y.-H. Zhang, and S. R. Johnson, "Absorption properties of type-II InAs/InAsSb superlattices measured by spectroscopic ellipsometry", Appl. Phys. Lett. **106**, 061907 (2015).

42 D. Souri and Z. E. Tahan, "A new method for the determination of optical band gap and the nature of optical transitions in semiconductors", Appl. Phys. B **119**, 273–279 (2015).

43 L. Viña, S. Logothetidis, and M. Cardona, "Temperature dependence of the dielectric function of germanium," Phys. Rev. B **30**, 1979 (1984).

44 T. M. Christian, K. Alberi, D. A. Beaton, B. Fluegel, and A. Mascarenhas, "Spectrally resolved localized states in $GaAs_{1-x}Bi_x$", Japanese J. Appl. Phys. **56**, 035801 (2017).

45 S. Francoeur, S. Tixier, E. Young, T. Tiedje, and A. Mascarenhas, "Bi isoelectronic impurities in GaAs", Phys. Rev. B **77**, 085209 (2008).

46 R. N. Kini, A. J. Ptak, B. Fluegel, R. France, R. C. Reedy, and A. Mascarenhas, "Effect of Bi alloying on the hole transport in the dilute bismide alloy $GaAs_{1-x}Bi_x$", Phys. Rev. B **83**, 075307 (2011).

47 Gwyddion, version 2.56, GNU General Public License.

48 G. Vardar, S. W. Paleg, M. V. Warren, M. Kang, S. Jeon, and R. S. Goldman, "Mechanisms of droplet formation and Bi incorporation during molecular beam epitaxy of GaAsBi", Appl. Phys. Lett. **102**, 042106 (2013).

49 MATLAB, version 2020a, Natick, MA, USA.

50 M. K. Rajpalke, W. M. Linhart, M. Birkett, K. M. Yu, J. Alaria, J. Kopaczek, R. Kudrawiec, T. S. Jones, M. J. Ashwin, and T. D. Veal, "High Bi content GaSbBi alloys", J. Appl. Phys. **116**, 043511 (2014).

51 P. P. Paskov, "Optical absorption and refraction spectra in highly excited GaSb", IEEE J. Quantum Elec. **30**, 12 (1994).

52 P. K. Basu, Theory of Optical Processes in Semiconductors (Clarendon Press, Oxford, 1997), p. 87.

53 A. R. Hassan, “On the estimation of matrix elements for optical transitions in semiconductors”, Optics Communications **98**, 80-85 (1993).

54 W. B. Jackson, S. M. Kelso, C. C. Tsai, J. W. Allen, and S.-J. Oh, “Energy dependence of the optical matrix element in hydrogenated amorphous and crystalline silicon”, Phys. Rev. B **31**, 5187 (1985).

55 M. Rohlfing and S. G. Louie, “Electron-Hole Excitations in Semiconductors and Insulators”, Phys. Rev. Lett. **81**, 2312 (1998).

56 T. Ogawa and T. Takagahara, “Optical absorption and Sommerfeld factors of one-dimensional semiconductors: An exact treatment of excitonic effects”, Phys. Rev. B **44**, 8138 (1991).

57 P. J. P. Tang, M. J. Pullin, and C. C. Phillips, “Binding energy of the free exciton in indium arsenide”, Phys. Rev. B **55**, 7 (1996).

58 I. Pelant and J. Valenta, Luminescence Spectroscopy of Semiconductors (Oxford University Press, Oxford UK, 2016), p. 163.

59 A. Gray, E. Abbena, and S. Salamon, Modern differential geometry of curves and surfaces with Mathematica (Chapman & Hall CRC, Boca Raton, FL, 2006), p. 14.

60 P. Y. Yu and M. Cardona, Fundamentals of Semiconductors (Springer-Verlag, Berlin Heidelberg, 2010), p. 276.

61 W. H. Press, S. A. Teukolsky, W. T. Vetterling, and B. P. Flannery, Numerical Recipes in Fortran 77: The Art of Scientific Computing (Press Syndicate, University of Cambridge, 1986), p. 180.

62 Wafer Technology Company, 34 Maryland Road, Milton Keynes, MK15 8HJ, UK.

63 WVASE32, version 3.774, Lincoln, NE, USA.

64 F. Stern, “Dispersion of the Index of Refraction Near the Absorption Edge of Semiconductors”, Phys. Rev. B **133**, A1653 (1964).

65 G. E. Stillman, C. M. Wolfe, and J. O. Dimmock, in Semiconductors and Semimetals (Academic, New York), Vol. 12, p. 169 (1977).

66 M. Hass and B. W. Henvis, "Infrared lattice reflection spectra of III-V compound semiconductors", J. Phys. Chem. Solids **23**, 1099 (1962).

67 J. R. Dixon and J. K. Furdyna, "Measurement of the static dielectric constant of the InSb lattice via gyrotropic sphere resonances", Solid State Communications **35**, 195 (1980).

68 M. W. Heller, and R. G. Hamerly, “Hole transport in gallium antimonide”, J. Appl. Phys. **57**, 10, 4626 (1985).

69 F. P. Kesamanly, Yu. Matsev, D. N. Nasledov, L. A. Nikolaeva, M. N. Pivovarov, V. A. Skripkin, and Yu. I. Uvanov, Fiz. Tekhn. Poluprr. **3**, 8, p. 1182-1187 (1969).

70 W. Zawadski, “Electron transport phenomena in small-gap semiconductors”, Advances in Phys. **23**, p. 435-522 (1974).

71 J.-M. Jancu, R. Scholz, E. A. de Andrada e Silva, and G. C. La Rocca, “Atomistic spin-orbit coupling and k·p parameters in III-V semiconductors”, Phys. Rev. B **72**, 193201 (2005).

72 M. Merian and A. K. Bhattacharjee, “Momentum Matrix Elements in III-V Semiconductor Alloys”, Solid State Communications **55**, 12, p. 1071-1073 (1985).

73 C. Hermann and C. Weisbuch, “k $\vec{}$·p $\vec{}$ perturbation theory in III-V compounds and alloys: a reexamination”, Phys. Rev. B **15**, 2, p. 823-833 (1977).

74 P. Pfeffer and W. Zawadzki, “Five-level k–p model for the conduction and valence bands of GaAs and InP”, Phys. Rev. B **53**, 19, p. 12813-12828 (1996).

75 E. O. Kane, “Band Structure of Indium Antimonide”, J. Phys. Chem. Solids **1**, 249 (1957).

76 V. Lucarini, J. J. Saarinen, K. -E. Peiponen, E.M. Vartiainen, Kramers-Kronig Relations in Optical Materials Research (Springer, Berlin, 2005), p. 35.

77 M. D. Sturge, "Optical Absorption of Gallium Arsenide between 0.6 and 2.75 eV", Phys. Rev. **127**, 768 (1962).

78 P. Lautenschlager, M. Garriga, S. Logothetidis, and M. Cardona, "Interband critical points of GaAs and their temperature dependence", Phys. Rev. B **35**, 9174 (1987).

79 H. C. Casey, D. D. Sell, and K. W. Wecht, “Concentration dependence of the absorption coefficient for n− and p−type GaAs between 1.3 and 1.6 eV”, J. Appl. Phys. **46**, 250 (1975).

80 G. M. Martin, “Optical assessment of the main electron trap in bulk semi-insulating GaAs”, Appl. Phys. Lett. **39**, 747 (1981).

81 M. B. Panish and H. C. Casey, Jr, "Temperature Dependence of the Energy Gap in GaAs and GaP", J. Appl. Phys. **40**, 163 (1969).

82 D. D. Sell, H. C. Casey Jr., and K. W. Wecht, "Concentration dependence of the refractive index for n - and p -type GaAs between 1.2 and 1.8 eV", J. Appl. Phys. **45**, 2650 (1974).

83 M.-C. Wu and C.-C. Chen, "Photoluminescence of high-quality GaSb grown from Ga- and Sb rich solutions by liquid-phase epitaxy", J. Appl. Phys. **72**, 4275 (1992).

84 V. Bellani, S. Di Lemia, M. Geddo, G. Guizzetti, A. Bosacchi, S. Franchi and R. Magnanini, "Thermoreflectance Study of the direct energy gap of GaSb", Solid State Comm. **104**, 81 (1997).

85 C. Ghezzi, R. Magnanini, A. Parisini, B. Rotelli, L. Tarricone, A. Bosacchi, and S. Franchi, "Optical absorption near the fundamental absorption edge in Gasb", Phys. Rev. B **52,** 1463 (1995).

86 A. Joullié, A. Zein Eddin, and B. Girault, "Temperature dependence of the L_6^c-Γ_6^c energy gap in gallium antimonide", Phys. Rev. B **23**, 928 (1981).

87 E. Adachi, "Energy band parameters of InAs at various temperatures", J. Phys. Soc. Jpn. **24**, 1178 (1968).

88 J. R. Dixon and J. M. Ellis, "Optical properties of n-Type Indium Arsenide in the fundamental absorption edge region", Phys. Rev. **123**, 1560 (1961).

89 Z. M. Fang, K. Y. Ma, D. H. Jaw, R. M. Cohen, and G. B. Stringfellow, "Photoluminescence of InSb, InAs, and InAsSb grown by organometallic vapor phase epitaxy", J. Appl. Phys. **67**, 7034 (1990).

90 Y. J. Jung, M. K. Park, S. I. Tae, K. H. Lee, and H. J. Lee, "Electron transport and energy-band structure of InSb", J. Appl. Phys. **69**, 3109 (1991).

91 C. L. Littler and D. G. Seiler, "Temperature dependence of the energy gap of InSb using nonlinear optical techniques", Appl. Phys. Lett. **46**, 986 (1985).

92 D. Auvergne, J. Camassel, H. Mathieu, and M. Cardona, "Temperature dependence of the band structure of germanium and zinc-blende-type semiconductors", Phys. Rev. B **9**, 5168 (1974).

93 J. Camassel and D. Auvergne, "Temperature dependence of the fundamental edge of germanium and zinc-blende-type semiconductors", Phys. Rev. B **12**, 3258 (1975).

94 K. L. Chopra and S. K. Bahl, "Exponential tail of the optical absorption edge of amorphous semiconductors", Thin Solid Films **II**, 377 (1972).

95 W. K. Metzger, R.K. Ahrenkiel, P. Dippo, J. Geisz, M.W. Wanlass, and S. Kurtz, "Time-Resolved Photoluminescence and Photovoltaics", NREL/CP-520-37028 (2005).

96 B. C. Connelly, G. D. Metcalfe, H. Shen, and M. Wraback, "Direct minority carrier lifetime measurements and recombination mechanisms in long-wave infrared type II superlattices using time-resolved photoluminescence", Appl. Phys. Lett. **97**, 251117 (2010).

97 S. R. Johnson, D. Ding, J.-B. Wang, S.-Q. Yu, and Y.-H. Zhang, "Excitation dependent photoluminescence measurements of the nonradiative lifetime and quantum efficiency in GaAs", J. Vac. Sci. Technol. B, **25**, 1077 (2007).

98 J. S. Bhosale, J. E. Moore, X. Wang, P. Bermel, and M. S. Lundstrom, "Steady-state photoluminescent excitation characterization of semiconductor carrier recombination", Review of Scientific Instruments 87, 013104 (2016).

99 N. F. Mott, "Recombination: a survey", Solid State Electronics **21**, 1275-1280 (1978).

100 D. K. Schroder, Semiconductor Material and Device Characterization (Wiley, New Jersey, 2006), Chap. 7.

101 J.-B. Wang, S. R. Johnson, D. Ding, S.-Q. Yu, and Y.-H. Zhang, "Influence of photon recycling on semiconductor luminescence refrigeration", J. Appl. Phys. **100**, 043502 (2006).

102 Q. Dai, Q. Shan, J. Wang, S. Chhajed, J. Cho, E. F. Schubert, M. H. Crawford, D. D. Koleske, M.-H. Kim, and Y. Park, "Carrier recombination mechanisms and efficiency droop in GaInN/GaN light-emitting diodes", Appl. Phys. Lett. **97**, 133507 (2010).

103 E. D. Palik, Handbook of Optical Constants of Solids (Academic, New York, 1985).

104 J. R. Lindle, J. R. Meyer, C. A. Hoffman, F. J. Bartoli, G. W. Turner, and H. K. Choi, "Auger lifetime in InAs, InAsSb, and InAsSb-InAlAsSb quantum wells", Appl. Phys. Lett. **67**, 3153 (1995).

105 B. V. Olson, E. A. Shaner, J. K. Kim, J. F. Klem, S. D. Hawkins, L. M. Murray, J. P. Prineas, M. E. Flatté, and T. F. Boggess, "Time-resolved optical measurements of minority carrier recombination in a mid-wave infrared InAsSb alloy and InAs/InAsSb superlattice", Appl. Phys. Lett. **101**, 092109 (2012).

106 N. A. Riordan, C. Gogineni, S. R. Johnson, X. Lu, T. Tiedje, D. Ding, Y.-H. Zhang, R. Fritz, K. Kolata, S. Chatterjee, K. Volz, and S. W. Koch, “Temperature and pump power dependent, photoluminescence characterization of MBE grown GaAsBi on GaAs”, J Mater Sci: Mater Electron **23**, 1799-1804 (2012).

107 A. R. Mohmad, F. Bastiman, C. J. Hunter, R. Richards, S. J. Sweeney, J. S. Ng, and J. P. R. David, “Effects of rapid thermal annealing on GaAs1-xBix alloys”, Appl. Phys. Lett. **101**, 012106 (2012).

108 G. Pettinari, A. Polimeni, M. Capizzi, J. H. Blokland, P. C. M. Christianen, J. C. Maan, E. C. Young, and T. Tiedje, “Influence of bismuth incorporation on the valence and conduction band edges of GaAs1-xBix”, Appl. Phys. Lett. **92**, 262105 (2008).

109 S. Imhof, A. Thränhardt, A. Chernikov, M. Koch, N. S. Köster, K. Kolata, S. Chatterjee, S. W. Koch, X. Lu, S. R. Johnson, D. A. Beaton, T. Tiedje, and O. Rubel, “Clustering effects in Ga(AsBi)”, Appl. Phys. Lett. **96**, 131115 (2010).

110 L. C. Bannow, O. Rubel, S. C. Badescu, P. Rosenow, J. Hader, J. V. Moloney, R. Tonner, and S. W. Koch, “Configuration Dependence of Band Gap Narrowing and Localization in Dilute GaAs{1-x}Bix Alloys”, Phys. Rev. B **93**, 205202 (2016).

111 A. Janotti, S.-H. Wei, and S. B. Zhang, “Theoretical study of the effects of isovalent coalloying of Bi and N in GaAs”, Phys. Rev. B **65**, 115203 (2002).

112 J. V. D. Veliadis, J. B. Khurgin, Y. J. Ding, A. G. Cui, and D. S. Katzer, “Investigation of the photoluminescence-linewidth broadening in periodic multiple narrow asymmetric coupled quantum wells”, Phys. Rev. B **50**, 4463 (1994).

113 T. R. Ravindran, A. K. Arora, B. Balamurugan, and B. R. Mehta, “Inhomogeneous broadening in the photoluminescence spectrum of CdS nanoparticles”, Nanostructured Materials **11**, 603 (1999).

114 G. D. Cody, T. Tiedje, B. Abeles, B. Brooks, and Y. Goldstein, “Disorder and the Optical-Absorption Edge of Hydrogenated Amorphous Silicon”, Phys. Rev. Lett. **47**, 1480 (1981).

115 X. Chen, W. Shen, D. Liang, R. Quhe, S. Wang, P. Guan, and P. Lu, "Effects of Bi on band gap bowing in $InP_{1-x}Bi_x$ alloys", Opt. Mat. Express **8**, 1184 (2018).

116 S. P. Svensson, H. Hier, W. L. Sarney, D. Donetsky, D. Wang, and G. Belenky, “Molecular beam epitaxy control and photoluminescence properties of InAsBi”, J. Vac. Sci. Technol. B **30**, 02B109 (2012).

117 Z. M. Fang, K. Y. Ma, R. M. Cohen, and G. B. Stringfellow, “Photoluminescence of InAsBi and InAsSbBi grown by organometallic vapor phase epitaxy”, J. Appl. Phys. **68**, 1187 (1990).

118 J. Wu, W. Shan, and W. Walukiewicz, “Band anticrossing in highly mismatched III-V semiconductor alloys”, Semicond. Sci. Technol. **17** 860–869 (2002).

119 J. Wu, W. Walukiewicz, K. M. Yu, J. W. Ager III, E. E. Haller, I. Miotkowski, A. K. Ramdas, Ching-Hua Su, I. K. Sou, R. C. C. Perera, and J. D. Denlinger, “Origin of the

large band-gap bowing in highly mismatched semiconductor alloys", Phys. Rev. B **67**, 035207 (2003).

120 K. Alberi, O. D. Dubon, W. Walukiewicz, K. M. Yu, K. Bertulis, and A. Krotkus, "Valence band anticrossing in GaBiAs", Appl. Phys. Lett. **91**, 051909 (2007).

121 M. Ferhat and A. Zaoui, "Structural and electronic properties of III-V bismuth compounds", Phys. Rev. B **73**, 115107 (2006).

122 A. Joullié, P. Christol, "GaSb-based mid-infrared 2-5μm laser diodes", C. R. Physique **4**, 621–637 (2003).

123 H. W. Yates and J. H. Taylor, Infrared Transmission of the Atmosphere, U.S. Naval Research Laboratory, NRL Report 5453 (1960).

124 PANalytical X'Pert Epitaxy, version 4.2, Almelo, The Netherlands.

125 J. Meija, T. B. Coplen, M. Berglund, W. A. Brand, P. D. Bievre, M. Groning, N. E. Holden, J. Irrgeher, R. D. Loss, T. Walczyk, and T. Prohaska, "Atomic weights of the elements 2013 (IUPAC Technical Report)", Pure Appl. Chem. **88**(3), 265–291 (2016).

126 J. R. Rumble, ed., "CRC Handbook of Chemistry and Physics", CRC Press/Taylor and Francis, Boca Raton, FL, 101st Edition, internet version 2020.

127 Y.P.Varshni, "Temperature dependence of the energy gap in semiconductors", Physica **34**, 149 (1967).

128 C. D. Thurmond, "The Standard Thermodynamic Functions for the Formation of Electrons and Holes in Ge, Si, GaAs, and GaP", J. Electrochem. Soc. **122**, 1133 (1975).

APPENDIX A

CALCULATION OF Bi MOLE FRACTION UNCERTAINTY

The mole fractions of the InAsSbBi samples are measured by photoluminescence spectroscopy measurements of bandgap energy and X-ray diffraction measurements of InAsSbBi layer lattice constant, each of which contributes to the mole fraction uncertainty. The uncertainty in the bandgap energy measurement is estimated from the low temperature width of the InAsSbBi photoluminescence spectra used to determine the bandgap energy. The significant amount of photoluminescence broadening observed in this material is primarily a result of lateral modulation in the Bi mole fraction[37] and pairing and clustering[110] of Bi atoms on the group-V sublattice sites. Therefore the uncertainty given by the spectral width is also a measure of the range of Bi mole fractions found in the material. The bandgap measurement uncertainty σ_g in the Bi, Sb, and As mole fractions x_i, y_i, and z_i is given by

$$\sigma_{g,Bi} = \frac{b_w(x_i) - 3.04\ meV}{51\ meV/\%\ Bi}, \tag{52a}$$

$$\sigma_{g,Sb} = \frac{3.04 - 0.75\ meV}{9.3\ meV/\%\ Sb} \tag{52b}$$

$$\sigma_{g,As} = \sigma_{g,Bi} + \sigma_{g,Sb} \tag{52c}$$

where $b_w(x_i)$ is the Bi mole fraction dependent low temperature width of photoluminescence spectra in the *i*-th sample due to Bi incorporation. The widths of the photoluminescence spectra are quantified by the difference between the photoluminescence peak energy E_p and bandgap energy E_g determined from the first-derivative maximum,[1] which is provided in Table V in Ref. 1 for InAsSbBi samples grown between 400 and 430 °C. The low-temperature width of the photoluminescence spectrum for Bi-free lattice matched InAsSb grown at 430 °C is 3.04 meV,[1] which is subtracted from the larger width $b_w(x_i)$ observed when Bi mole fraction x_i is present in the material. This

difference is that portion of bandgap energy uncertainty due to Bi incorporation and is divided by 51 meV/% Bi,[4] which is the shift in the bandgap energy per percent Bi mole fraction. The photoluminescence width[1] of the 210 nm bulk samples and 10 nm quantum well samples are shown in Fig. 46 as a function of Bi mole fraction. A power law relation with amplitude of 10.87 meV and power law 0.268 is fit to the bulk samples while a linear relation with slope 2.11 meV/% Bi is fit to the quantum well samples. These fits provide the functional form for the photoluminescence width versus Bi mole fraction, $b_w(x_i)$, that is applied to the InAsSbBi samples examined in this work.

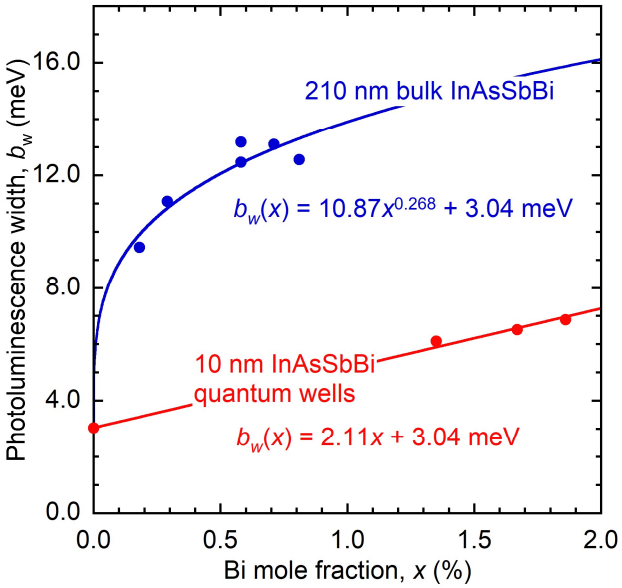

FIG. 46. Low-temperature photoluminescence width for 210 nm thick bulk InAsSbBi (blue circles) and 10 nm thick InAsSbBi quantum wells (red circles) from Table V in Ref. 1. Power law fit (blue curve) to the bulk samples and linear fit (red curve) to the quantum well samples are shown.

By similar logic the low-temperature photoluminescence width of 0.75 meV[1] for InAs grown on InAs at 450 °C is subtracted from the width observed when Sb mole fraction y_i is present in the material. Since the Sb mole fractions examined in this work do not deviate greatly from lattice matched material, the InAsSb width is assumed to be constant at 3.04 meV, yielding a constant Sb mole fraction uncertainty of $\sigma_{g,Sb}$ = 0.25 % when divided by 9.3 meV/% Sb,[5] which is the shift in the bandgap energy per percent Sb mole fraction. Finally, the As mole fraction uncertainty due to bandgap energy measurement is simply given by the sum of the Bi and Sb mole fraction uncertainties.

The mole fraction uncertainty due to lattice constant measurement, σ_a, is determined by the dynamical simulation of the coupled $\omega - 2\theta$ X-ray diffraction scans of the (400) crystal plane using the PANalytical X'Pert Epitaxy software package.[124] This uncertainty is independent of Bi mole fraction and depends only on the sample structure. For example, even InAsSb bulk samples[5] with zero Bi content exhibit a degree of uncertainty in the lattice constant. The Bi mole fraction uncertainty due to lattice constant measurement is determined by varying the Bi mole fraction in the dynamical simulation of the X-ray diffraction scan until the minimum resolvable change in the InAsSbBi layer peak position is observed. This uncertainty $\sigma_{a,Bi}$ is 0.1% Bi mole fraction in the 210 nm bulk InAsSbBi samples and 0.3% Bi mole fraction in the 10 nm InAsSbBi quantum well samples.

The Sb and As mole fraction uncertainties $\sigma_{a,Sb}$ and $\sigma_{a,As}$ are related to the Bi mole fraction uncertainties $\sigma_{a,Bi}$ by Vegard's Law, which relates the Bi and Sb mole fractions x and y:[1]

$$y = \frac{a_{InAsSbBi} - a_{InAs}}{a_{InSb} - a_{InAs}} - x\frac{a_{InBi} - a_{InAs}}{a_{InSb} - a_{InAs}}, \tag{53a}$$

$$\left|\frac{dy}{dx}\right| = \frac{a_{InBi} - a_{InAs}}{a_{InSb} - a_{InAs}}. \tag{53b}$$

The Sb mole fraction uncertainty is given by:

$$\sigma_{a,Sb} = \sigma_{a,Bi}\left|\frac{dy}{dx}\right| \cong 1.31\sigma_{a,Bi}. \tag{54}$$

The As mole fraction uncertainty is given by the sum of the Sb and Bi mole fraction uncertainties:

$$\sigma_{a,As} \cong \sigma_{a,Bi} + \sigma_{a,Sb} = \sigma_{a,Bi} + \sigma_{a,Bi}\left|\frac{dy}{dx}\right| \cong 2.31\sigma_{a,Bi} \tag{55}$$

The Bi, Sb, and As mole fraction uncertainties due to X-ray diffraction measurement of the lattice constant are summarized as:

$$\sigma_{a,Bi} = \begin{cases} 0.10\% \text{ for bulk samples} \\ 0.30\% \text{ for quantum well samples} \end{cases} \tag{56a}$$

$$\sigma_{a,Sb} = 1.31\sigma_{a,Bi} \tag{56b}$$

$$\sigma_{a,As} = 2.31\sigma_{a,Bi} \tag{56c}$$

The total uncertainty σ in the Bi, Sb, and As mole fractions is given by the squared sum of the bandgap energy and lattice constant measurement uncertainties:

$$\sigma^2 = {\sigma_g}^2 + {\sigma_a}^2. \tag{57}$$

Here it is assumed that the two uncertainties are uncorrelated such that the covariance of σ_a and σ_g is zero. The mole fraction uncertainties due to bandgap energy measurement, lattice constant measurement, and total uncertainty are listed below in Table 21. The total mole fraction uncertainties for all three group V species are also reported in Table 4.

TABLE 21. Bi, Sb, and As mole fraction uncertainties due to bandgap energy and lattice constant measurement uncertainty.

Sample	Cross section	Growth temperature (°C)	Mole fraction uncertainties (%) from bandgap measurement, σ_g			from lattice constant measurement, σ_a			Total uncertainty, σ		
			Bi	Sb	As	Bi	Sb	As	Bi	Sb	As
A	Bulk	400	0.18	0.25	0.43	0.10	0.13	0.23	0.21	0.28	0.49
B	Bulk	400	0.19	0.25	0.44	0.10	0.13	0.23	0.22	0.28	0.50
C	Bulk	400	0.20	0.25	0.45	0.10	0.13	0.23	0.22	0.28	0.51
D	Bulk	400	0.18	0.25	0.43	0.10	0.13	0.23	0.21	0.28	0.49
E	QW	400	0.08	0.25	0.33	0.30	0.39	0.69	0.31	0.47	0.77
F	QW	400	0.07	0.25	0.32	0.30	0.39	0.69	0.31	0.47	0.76
G	QW	400	0.06	0.25	0.31	0.30	0.39	0.69	0.31	0.47	0.76
H	Bulk	420	0.15	0.25	0.40	0.10	0.13	0.23	0.18	0.28	0.46
I	Bulk	420	0.14	0.25	0.39	0.10	0.13	0.23	0.17	0.28	0.46
J	Bulk	420	0.14	0.25	0.39	0.10	0.13	0.23	0.17	0.28	0.45
K	Bulk	420	0.14	0.25	0.39	0.10	0.13	0.23	0.17	0.28	0.45
L	Bulk	420	0.14	0.25	0.39	0.10	0.13	0.23	0.18	0.28	0.46
M	Bulk	420	0.14	0.25	0.39	0.10	0.13	0.23	0.17	0.28	0.45
N	Bulk	420	0.12	0.25	0.37	0.10	0.13	0.23	0.16	0.28	0.44
O	Bulk	420	0.14	0.25	0.39	0.10	0.13	0.23	0.17	0.28	0.45
P	Bulk	420	0.15	0.25	0.40	0.10	0.13	0.23	0.18	0.28	0.46
Q	Bulk	420	0.16	0.25	0.41	0.10	0.13	0.23	0.19	0.28	0.47

APPENDIX B

AFM FLATTENING PROCEDURE

The 100 μm by 100 μm images acquired by atomic force microscopy (AFM) exhibit several sources of noise including 1/f noise and row streaking due to rastering of the comparatively small AFM probe tip over the large image area. A flattening procedure is implemented in the Gwyddion software[47] to convert the noisy sample surface into a uniform plane on which the droplet features reside. First, row correction is performed to remove horizontal streaking. The "align rows using various methods" tool is used and the "median" method is specified. Next, a two-dimensional polynomial function of 4^{th} order in both image axes (x and y) is fitted to the AFM image using the "Remove polynomial background" tool. After row correction and polynomial background fitting, the "Level data by fitting a plane through three points" tool is used to correct for any residual tilt of the sample surface in the image. This procedure results in a flat, uniform background plane with typical tolerances of ± 15 nm for the 400 °C grown samples and ± 1.5 nm for the 420 °C grown samples. Detailed Fourier analysis indicates that the magnitude distortion due to the highpass filtering performed by row correction and 4^{th} order polynomial background flattening is negligible above 0.1 μm^{-1} in frequency, or 10 μm in real space. Therefore the amplitude of the droplet features, with average diameters of approximately 2 μm or less, is unaffected by the flattening procedure. Fig 47 shows the flattening procedure including the row correction and polynomial background for 400 °C grown sample B.

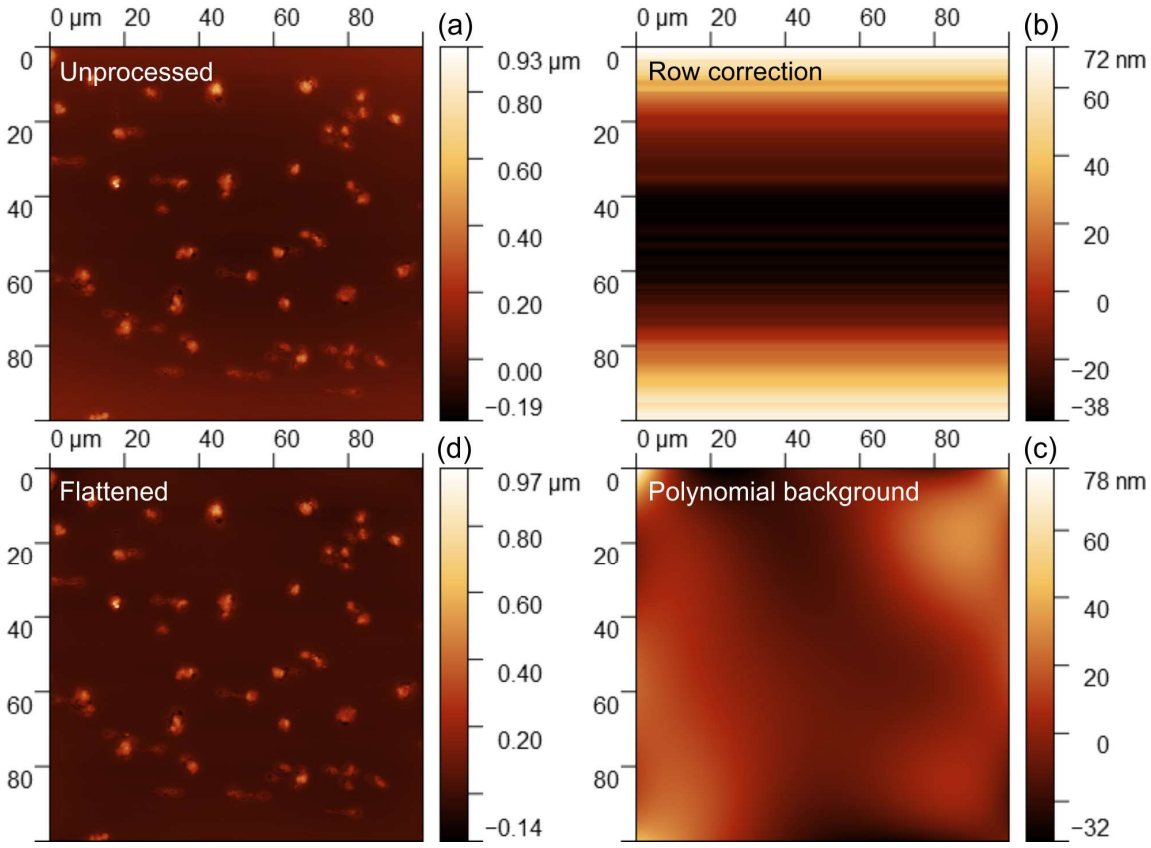

FIG. 47. Background flattening procedure for 100 µm by 100 µm atomic force microscopy images of 400 °C grown sample B with Bi/In = 0.050, Sb/In = 0.120, and As/In = 0.911. Clockwise from upper left: (a) unprocessed AFM image, (b) row correction using "median" method, (c) 4th order polynomial background, and (d) resulting AFM image with flattened background. The planar surface of the image is uniform to within ± 15 nm.

APPENDIX C

CALCULATION OF DROPLET ACCUMULATION RATE

The total amount of In per unit area, N_{In}, accumulated in the surface droplets is calculated from the difference between the target and measured InAsSbBi layer thickness, h_{diff}:

$$N_{In} = 4\frac{h_{diff}}{a_{InAsSbBi}^3} \tag{58}$$

Where $a_{InAsSbBi}$ is the lattice constant of the zinc-blende InAsSbBi unit cell. The volume per unit area of metallic In, h_{In}, contained within the droplets is then given by the product of the In per unit area and the metallic volume associated with each In atom, V_{In}:

$$h_{In} = N_{In}V_{In} = N_{In}\frac{m_{In}}{\rho_{In}N_A} \tag{59}$$

Where m_{In} = 114.82 g/mol is the atomic mass of In,[125] ρ_{In} = 7.31 g/cm^3 is the density of metallic In,[126] and N_A = 6.0221×10^{23} is Avogadro's number. Conceptually, h_{In} is the thickness of a uniform layer of metallic In equal to the amount of In contained within the droplet features. The corresponding amount of metallic Bi per unit area, N_{Bi}, contained within the droplets is given from difference between the total droplet volume per unit area, $h_{droplet}$, and the metallic In volume per unit area h_{In}:

$$N_{Bi} = \frac{h_{droplet} - h_{In}}{V_{Bi}} = \left(h_{droplet} - h_{In}\right)\frac{\rho_{Bi}N_A}{m_{Bi}} \tag{60}$$

Where m_{Bi} = 208.98 g/mol is the atomic mass of Bi[125] and ρ_{Bi} = 9.78 g/cm^3 is the density of metallic Bi.[126] Finally, the measured rate of Bi accumulation in droplets, $\theta_{Bi}R_{dro}$, normalized to the In flux is given as:

$$\theta_{Bi}R_{dro} = \frac{N_{Bi}}{F_{In}T} = \frac{N_{Bi}}{3.696 \times 10^{17}\ \text{cm}^{-2}} \tag{61}$$

The product $F_{In}T$ is 3.696×10^{17} cm^{-2} for all the 210 nm thick samples grown for a duration of 840 seconds at a constant In flux of 4.4×10^{14} cm^{-2} s^{-1}. Table 6 summarizes the droplet composition analysis and Bi droplet accumulation rates for the six droplet covered samples B, C, D, M, O, and Q.

APPENDIX D

LITERATURE COMPARISON OF BANDGAP ENERGIES

Sell *et al*[82] examined the refractive index of a large number of n-type and p-type melt-grown GaAs samples, as well as GaAs samples grown by liquid- and vapor-phase epitaxy. The refractive index was measured by double-beam reflectance spectroscopy, and a model based on the work of Elliott[14] including exciton absorption and Coulomb screening was fitted to the reflectance spectrum. The ground state exciton peak was identified from the fit at 1.420 eV, and with the addition of the binding energy of approximately 4 meV the bandgap energy at 297 K was identified as 1.424 ± 0.001 eV. Panish and Casey[81] measured the bandgap energy of an undoped, boat-grown GaAs sample using transmission spectroscopy at temperatures ranging from 300-973 K. Combining these high-temperature measurements with low-temperature bandgap measurements performed by Sturge[77], the Varshni equation[127] is fitted to determine a bandgap energy of 1.436 ± 0.003 eV at 297 K. Thurmond[128] combined the high-temperature measurements of Panish and Casey with the 297 K measurement by D.D. Sell to refine the Varshni equation fit; however the resulting bandgap energy uncertainty of 4 meV is comparatively large. Lautenschlager *et al*[78] measured an undoped n-type GaAs wafer by spectroscopic ellipsometry at temperatures ranging from 20 to 750 K. Fits to the second derivative of the complex dielectric function yield a bandgap energy of 1.4241 eV at 297 K. More recently, Beaudoin *et al*[12] measured semi-insulating GaAs from room temperature to 1178 K by transmission spectroscopy; fits to the Urbach edge of absorption yield a bandgap energy of 1.4220 ± 0.0007 eV at 297 K. These literature results are summarized in Table 22. It is evident that many publications on the room-temperature bandgap of GaAs are based on the pioneering work of Sell *et al*, Panish and Casey, and Sturge.

TABLE 22. Comparison of GaAs bandgap energies measured in this work with those from the literature.

Reference	GaAs bandgap energy, E_g (eV)	Temperature (K)	Physical quantity measured	Method of analysis
This work	1.4180 ± 0.0002	297	Absorption coefficient	Absorption model Eq. 26 fit
This work	1.4182 ± 0.0001	297	Refractive index	Peak location
D. D. Sell *et al*, J. Appl. Phys. **45**, 2650 (1974).[82]	1.424 ± 0.001	297	Reflectance and refractive index	Elliott absorption model fit to reflectance data. Identify exciton location, then add binding energy ~4 meV
M. B. Panish and H. C. Casey, J. Appl. Phys. **40**, 163 (1969).[81]	1.436 ± 0.003	297	Absorption coefficient	Energy shift of the Urbach edge at a constant absorption coefficient of 40 cm^{-1} relative to Sturge's 294 K measurement[38]
P. Lautenschlager *et al*, Phy. Rev. B **35**, 9174 (1987).[78]	1.4241	297	Complex dielectric function	Standard lineshape fits to the complex dielectric function which identify interband critical points
M. Beaudoin *et al*, Appl. Phys. Lett. **70**, 26 (1997).[12]	1.4220 ± 0.0007	297	Absorption coefficient	Fits to the Urbach edge of absorption, with fit amplitude of 8000 cm^{-1} at the bandgap
M. D. Sturge, Phys. Rev. **127**, 786 (1962).[77]	1.435	294	Absorption coefficient	Elliott absorption model fit to absorption data

Applying the Urbach edge analysis performed by M. Beaudoin *et al*[12] to the GaAs measurements in this work results in a similar energy position of the extrapolated 8000 cm^{-1} absorption coefficient. The value from this work is 1.4213 eV, which is within 1 meV of their 1.4220 eV reported value.

A. Joullié *et al*[86] performed low-field electroreflectance measurements on p-type GaSb samples grown by the Bridgman method and determined a fundamental bandgap energy of 0.724 eV at 300 K. M-C. Wu and C.-C. Chen[83] performed temperature-dependent photoluminescence measurements on both p- and n-type GaSb samples grown by liquid phase epitaxy. Varshni equation fits to the photoluminescence peak energy yielded a

bandgap energy of 0.728 eV at 297 K. C. Ghezzi *et al*[85] measured undoped, residually p-type GaSb layers grown by molecular beam epitaxy by optical transmission in the 1.2 – 2.0 μm spectrum. The absorption coefficient is calculated from the transmission spectra and Elliott's absorption model[14] is fit to the data to determine a bandgap energy of 0.728 eV at 297 K. V. Bellani *et al*[84] measured 6 μm thick undoped GaSb layers also grown by molecular beam epitaxy using thermoreflectance spectroscopy; the imaginary dielectric constant ε_2 is calculated from the reflectance ratio, and the first-derivative maximum of ε_2 at the fundamental absorption edge yields a bandgap energy of 0.724 eV at 300 K. These literature results are summarized below in Table 23. The bandgap energy obtained by analysis of the absorption edge in this work, 0.7304 eV, agrees to within less than 5 meV with literature at 297 K.

TABLE 23. Comparison of GaSb bandgap energies measured in this work with those from the literature.

Reference	GaSb bandgap energy, E_g (eV)	Temperature (K)	Physical quantity measured	Method of analysis
This work	0.7304	297	Absorption coefficient	Absorption model Eq. 26 fit
A. Joullié *et al*, Phys. Rev. B **23**, 928 (1981).[86]	0.724	300	Reflectance	Analysis of electroreflectance spectra and theoretical Franz-Keldysh oscillations
M.-C. Wu and C.-C. Chen, J. Appl. Phys. **72**, 4275 (1992).[83]	0.728	297	Photoluminescence	Varshni equation fit to PL peak energy measured from 16 – 250 K
C. Ghezzi *et al*, Phys. Rev. B **52**, 1463 (1995).[85]	0.728	297	Transmission	Fits of Elliot's absorption model to measured data between 9 - 300 K, Varshni equation fit
V. Bellani *et al*, Solid State Comm. **104**, 81 (1997).[84]	0.724	300	Reflectance	First derivative maximum of ε_2 calculated from the reflectance ratio $\Delta R/R$

One of the earliest measurements of bandgap energy of InAs was performed by J. R. Dixon and M. Ellis[88] on 3 μm to 1 mm thick n-type InAs samples. Transmission measurements yield the absorption coefficient, from which plots of α^2 vs $h\nu$ are extrapolated down to zero absorption to yield the bandgap energy of 0.35 eV at 300 K. E. Adachi[87] performed magneto-absorption measurements on an 8 μm thick n-type InAs sample and determined a bandgap energy of 0.356 eV at 298 K from the first minimum of the transmission spectrum. Z. M. Fang *et al*[89] measured photoluminescence from undoped n-type InAs substrates and epilayers grown by metalorganic vapor phase epitaxy; the energy of the photoluminescence peak minus one-half the thermal energy $kT/2$ yields a bandgap energy of 0.351 eV at 300 K. These literature results are summarized below in

Table 24. The bandgap energy obtained by analysis of the absorption edge in this work, 0.3565 eV, agrees very closely with commonly-cited literature at 297 K.

TABLE 24. Comparison of InAs bandgap energies measured in this work with those from the literature.

Reference	InAs bandgap energy, E_g (eV)	Temperature (K)	Physical quantity measured	Method of analysis
This work	0.3565	297	Absorption coefficient	Absorption model Eq. 26 fit
J. R. Dixon and J. M. Ellis, Phys. Rev. **123**, 1560 (1961).[88]	0.35	300	Transmission	Extrapolations of α^2 vs $h\nu$ plots down to zero absorption
E. Adachi, J. Phys. Soc. Jpn. **24**, 1178 (1968).[87]	0.356	298	Transmission	First transmission minimum of magneto-absorption spectrum
Z. M. Fang *et al*, J. Appl. Phys. **67**, 7024 (1990).[89]	0.351	300	Photoluminescence	Varshni equation fit to PL peak energy less kT/2

D. Auvergne *et al*[92] analyzed the temperature dependence of piezoreflectance spectra from InSb and measured a bandgap energy of 0.175 eV at 310 K. J. Camassel and D. Auvergne[93] further refined this work with the addition of pseudopotential calculations of band structure and arrived at an InSb bandgap energy of 0.172 eV at 300 K. C. L. Littler and D. G. Seiler[91] performed two-photon Hall effect measurements on single-crystal, n-type InSb and obtained bandgap energies as a function of both temperature and magnetic field; extrapolation down to zero field yields the InSb bandgap energy versus temperature. Fitting the Varshni equation to this data yields a bandgap energy of 0.169 eV at 297 K. As was done for InAs, Z. M. Fang *et al*[89] measured photoluminescence from undoped n-type InSb substrates and epilayers grown by metalorganic vapor phase epitaxy; the energy of

the photoluminescence peak minus one-half the thermal energy $kT/2$ yields a bandgap energy of 0.176 eV at 300 K. Y. J. Yung *et al*[90] grew n-type InSb samples by the zone-melting or zone-refining technique and measured the conductivity and Hall coefficient at temperatures ranging from 90 to 470 K. By numerically solving the Boltzmann transport equation and relating the effective mass to the bandgap energy, the temperature dependence of bandgap energy is established yielding a value of 0.180 eV at 297 K. These literature results are summarized below in Table 25. Considering the relatively wide error between measurements in literature, as great as 10 meV, the InSb bandgap energy of 0.1802 eV at 297 K established in this work agrees well with values reported in literature.

TABLE 25. Comparison of InSb bandgap energies measured in this work with those from the literature.

Reference	InSb bandgap energy, E_g (eV)	Temperature (K)	Physical quantity measured	Method of analysis
This work	0.1802	297	Absorption coefficient	Absorption model Eq. 26 fit
D. Auvergne *et al*, Phys. Rev. B **9**, 5168 (1974).[92]	0.175	310	Reflectance	Analysis of piezoreflectance spectra
J. Camassel and D. Auvergne, Phys. Rev. B **12**, 3258 (1975).[93]	0.172	300	Reflectance / pseudopotential calculations	Refinement of analysis of piezoreflectance spectra
C. L. Littler and D. G. Seiler, Appl. Phys. Lett. **46**, 986 (1985).[91]	0.169	297	Photo-Hall response	Fits to two-photon photo-Hall response data acquired between 20-210 K. Varshni equation is fit to temperature dependence
Z. M. Fang *et al*, J. Appl. Phys. **67**, 7024 (1990).[89]	0.176	297	Photoluminescence	Varshni equation fit to PL peak less kT/2
Y. J. Yung *et al*, J. Appl. Phys. **69**, 3109 (1991).[90]	0.180	297	Conductivity/Hall coefficient	Analysis of effective mass variation from conductivity and Hall effect measurements, and Varshni equation fit to calculated bandgap energies

APPENDIX E

MATLAB CODE FOR MBE GROWTH MODEL FITTING ROUTINE

fit_model_params.m

```
clear all;

%%%%%%%%%%%%%%%%%%%%%%%%%%%%%%%%%%%%%%%%%%%%%%%%%%%%%%%%%%%%%%%%%%%%%%%%%%%%

% Import the experimental data.
% B2511, B2561, B2562, B2563, B2566, B2567, B2568, B2509, B2513, B2514,
B2515, B2518, B2519, B2523, B2524, B2526, B2527
T = transpose(xlsread('C:\Users\steph\Documents\ASU
Documents\Research\Papers\InAsSbBi MBE growth model Spring
2020\Analysis\Sample table 20200902.xlsx', 1, 'D3:D19'));
F = transpose(xlsread('C:\Users\steph\Documents\ASU
Documents\Research\Papers\InAsSbBi MBE growth model Spring
2020\Analysis\Sample table 20200902.xlsx', 1, 'H3:J19'));
MF = 0.01*transpose(xlsread('C:\Users\steph\Documents\ASU
Documents\Research\Papers\InAsSbBi MBE growth model Spring
2020\Analysis\Sample table 20200902.xlsx', 1, 'K3:M19'));
sigmax = 0.01*transpose(xlsread('C:\Users\steph\Documents\ASU
Documents\Research\Papers\InAsSbBi MBE growth model Spring
2020\Analysis\Sample table 20200902.xlsx', 1, 'Q3:Q19'));
S = transpose(xlsread('C:\Users\steph\Documents\ASU
Documents\Research\Papers\InAsSbBi MBE growth model Spring
2020\Analysis\Sample table 20200902.xlsx', 1, 'AK3:AM19'));

x = MF(1,:);
y = MF(2,:);
z = MF(3,:);
Sdr = S(2,:);
Rdr = F(1,:).*Sdr;

% Calculate incorporation coefficients for each species.
Sinc = zeros(3, length(MF(1,:)));
Sinc_400 = [0, 0, 0];
Sinc_420 = [0, 0, 0];
Sinc_avg = zeros(3, 2);

for i=1:3
    Sinc(i,:) = MF(i,:)./F(i,:);

    Sinc_400(i) = sum(Sinc(i,1:7))/7;
    Sinc_420(i) = sum(Sinc(i,8:17))/10;

    Sinc_avg(i,:) = [Sinc_400(i), Sinc_420(i)];
end

% The Sb and As mole fraction uncertainties are related to the Bi mole
% fraction uncertainty.
sigma(1,:) = sigmax;
sigma(2,:) = 1.3*sigmax;
sigma(3,:) = 2.3*sigmax;

%%
```

```
%%%%%%%%%%%%%%%%%%%%%%%%%%%%%%%%%%%%%%%%%%%%%%%%%%%%%%%%%%%%%%%%%%%%%%%%%%%%

% Iteratively calculate an average droplet uptake rate Rdro and fit the
% growth model to the Bi mole fraction.
% Exit the loop when the droplet uptake rate Rdro has converged.

% Absolute tolerance on Rdro, normalized to In flux
tol = 1e-5;

% Initialize the droplet uptake rate Rdro. Assume theta_Bi = 0.2 for
% droplet covered samples.
% Droplet-covered samples: B2566, B2567, B2568
Rdro_400 = (sum(Rdr(2:4))/3)/0.2;
% Droplet-covered samples: B2519, B2524, B2527
Rdro_420 = (sum([Rdr(13), Rdr(15), Rdr(17)])/3)/0.2;
Rdro = zeros(1,17);
Rdro(1:7) = [0, 1, 1, 1, 0, 0, 0]*Rdro_400;
Rdro(8:17) = [0, 0, 0, 0, 0, 1, 0, 1, 0, 1]*Rdro_420;

% Initialize Rdro_err, equal to Rdro - Rdro_last.
Rdro_400_last = 0;
Rdro_420_last = 0;
Rdro_400_err = Rdro_400 - Rdro_400_last;
Rdro_420_err = Rdro_420 - Rdro_420_last;

% Specify the number of random initial conditions to use.
N = 1000;

% Set upper and lower bounds on all model parameters.
lb = zeros(3, 8);
ub = zeros(3, 8);

% Bi model parameters
% Rdes_400, Rdes_420, Rinc_400, Rinc_420, Prem_As, Prem_Sb, Pexc_As,
Pexc_Sb
lb(1,:) = [0.00, 0.00, 0.00, 0.00, 0.00, 0.00, 0.00, 0.00];
ub(1,:) = [1.00, 1.00, 1.00, 0.00, 1.00, 1.00, 1.00, 1.00];

% Sb model parameters
% Rdes_400, Rdes_420, Rinc_400, Rinc_420, Prem_As, Prem_Sb, Pexc_As,
Pexc_Sb
lb(2,:) = [0.00, 0.00, 0.00, 0.00, 0.00, 0.00, 0.00, 0.00];
ub(2,:) = [1.00, 0.00, 1.00, 0.00, 1.00, 1.00, 1.00, 1.00];

% As model parameters
% Rdes_400, Rdes_420, Rinc_400, Rinc_420, Prem_As, Prem_Sb, Pexc_As,
Pexc_Sb
lb(3,:) = [0.00, 0.00, 0.00, 0.00, 0.00, 0.00, 0.00, 0.00];
ub(3,:) = [1.00, 0.00, 5.00, 0.00, 1.00, 1.00, 1.00, 1.00];

% Generate an array of random numbers ranging between 0 and 1.
P0 = rand(N, 3, length(lb));
```

```
% Use these bounds to specify the range of the initial conditions.
for i=1:N
    for j=1:3
        P0(i,j,:) = lb(j,:) + (ub(j,:) -
lb(j,:)).*transpose(squeeze(P0(i,j,:)));
    end
end

% Manually specify the fmincon options.
options = optimoptions('fmincon');
options.Algorithm = 'interior-point';
options.ObjectiveLimit = 1e-20;
options.OptimalityTolerance = 1e-7;
options.StepTolerance = 1e-12;
options.MaxFunctionEvaluations = 1e4;
options.MaxIterations = 2e3;
options.ConstraintTolerance = 1e-6;

% There are no linear constraints, so set these all to null.
A = [];
b = [];
Aeq = [];
beq = [];

% Loop counter to limit iterations and prevent infinite loops.
count = 0;
limit = 10;

% Enter the main loop on the droplet uptake rate. Exit when the droplet
% rates have converged.
while ((abs(Rdro_400_err) > tol) || (abs(Rdro_420_err) > tol)) &&
(count < limit)

      % Use MATLAB's function fmincon to minimize the sum of squared
      error with respect to the Bi mole fraction.
    chisq = @(P)chisqfun(MBEmodel(F, MF, T, Rdr, Sinc_avg, P), MF,
    sigma);

    % Loop on the initial conditions and minimize the model parameters.
    Pmin = zeros(N, 3, length(lb(1,:)));
    MFfit = zeros(N, 3, length(MF(1,:)));
    theta = zeros(N, 3, length(MF(1,:)));
    chisq_out = zeros(1,N);

    if (count == 1)
        for i=1:N
            % Perform the minimization using stochastic initialization
            for the first iteration of the Rdro loop.
            Pmin(i,:,:) = fmincon(chisq, squeeze(P0(i,:,:)), A, b, Aeq,
            beq, lb, ub, @(P)nonlincon(F, MF, T, Rdr, Sinc_avg, P),
            options);

            % Get the mole fractions and surface coverage fractions
            corresponding to the optimized model parameters.
```

```
            [MFfit(i,:,:), theta(i,:,:)] = MBEmodel(F, MF, T, Rdr,
            Sinc_avg, squeeze(Pmin(i,:,:)));

            % Calculate the sum of mean squared error.
            chisq_out(i) = chisqfun(squeeze(MFfit(i,:,:)), MF, sigma);

            % Get the global minimum.
            [chisqmin, index] = min(chisq_out);
            P_global = squeeze(Pmin(index,:,:));
            MF_global = squeeze(MFfit(index,:,:));
            theta_global = squeeze(theta(index,:,:));
        end

    else
        % Otherwise, use the last best-fit model parameters as the
      initial condition.
        Pmin(1,:,:) = fmincon(chisq, P_last, A, b, Aeq, beq, lb, ub,
        @(P)nonlincon(F, MF, T, Rdr, Sinc_avg, P), options);

        % Get the mole fractions and surface coverage fractions
      corresponding to the optimized model parameters.
        [MFfit(1,:,:), theta(1,:,:)] = MBEmodel(F, MF, T, Rdr,
        Sinc_avg, squeeze(Pmin(i,:,:)));

        % Calculate the sum of mean squared error.
        chisq_out(i) = chisqfun(squeeze(MFfit(1,:,:)), MF, sigma);

        % Get the global minimum.
        chisqmin = min(chisq_out);
        P_global = squeeze(Pmin(1,:,:));
        MF_global = squeeze(MFfit(1,:,:));
        theta_global = squeeze(theta(1,:,:));
    end

    % Assign the current values for Rdro to Rdro_last.
    Rdro_400_last = Rdro_400;
    Rdro_420_last = Rdro_420;
    P_last = P_global;

    % Update the droplet uptake rate Rdro from the measured droplet
    % uptake rates by dividing by theta_Bi and averaging the result.
    % Droplet-covered samples: B2566, B2567, B2568
    Rdro_400 = Rdr(2:4)./theta_global(1,2:4);
    % Droplet-covered samples: B2519, B2524, B2527
    Rdro_420 = [Rdr(13), Rdr(15), Rdr(17)]./[theta_global(1,13),
theta_global(1,15), theta_global(1,17)];
    Rdro_400 = sum(Rdro_400)/3;
    Rdro_420 = sum(Rdro_420)/3;

    % Calculate the error in droplet uptake rates between iterations.
    Rdro_400_err = Rdro_400 - Rdro_400_last;
    Rdro_420_err = Rdro_420 - Rdro_420_last;
```

```
    % Update the individual sample droplet uptake rates.
    Rdro(1:7) = [0, 1, 1, 1, 0, 0, 0]*Rdro_400;
    Rdro(8:17) = [0, 0, 0, 0, 0, 1, 0, 1, 0, 1]*Rdro_420;

    % Increment loop counter.
    count = count + 1;

end
```

MBEmodel.m

```
function [MFfit, theta] = MBEmodel(F, MF, T, Rdr, Sinc, P)
% InAsSbBi_MBE_model
% Kinetic growth model for MBE growth of InAsSbBi based on the work:
% C. R. Tait and J. M. Millunchick, "Kinetics of droplet formation and
Bi
% incorporation in GaSbBi alloys", J. Appl. Phys. 199, 215302 (2016).
% All model parameters (e.g. desorption and incorporation rates) are
% assumed to scale with In flux (i.e. growth rate), unless otherwise
stated
%
% Inputs:
% F         Array of flux ratios: Bi/In, Sb/In, As/In.
% MF        Array of mole fractions: Bi, Sb, As (x, y, z)
% T         Vector of growth temperatures, in Celsius.
% Rdr       Bi droplet accumulation rate, unitless. Measured by AFM
% Sinc      Average incorporation coefficients for Bi, Sb, and As at
400
%           and 420 C, used to calculate Rinc
% P         Array of model parameters, to construct a global fitting
%           algorithm: Bi, Sb, As
%
% Outputs:
% MFfit     Modeled mole fractions: Bi, Sb, As (x, y, z)
% theta     Modeled surface coverage fractions: Bi, Sb, As

% Unpack model parameters.
% Bi first:
Rdes_Bi_400    = P(1,1);    % Rate of Bi self-desorption at 400 C,
normalized to In flux (unitless)
Rdes_Bi_420    = P(1,2);    % Rate of Bi self-desorption at 420 C,
normalized to In flux (unitless)
Rinc_Bi_400    = P(1,3);    % Rate of Bi incorporation at 400 C,
normalized to In flux (unitless)
% Rinc_Bi_420    = P(1,4);    % Rate of Bi incorporation at 400 C,
normalized to In flux (unitless)
Prem_Bi_As_400 = P(1,5);    % Probability of As-assisted removal at 400
C
Prem_Bi_As_420 = P(1,5);    % Probability of As-assisted removal at 420
C
Prem_Bi_Sb_400 = P(1,6);    % Probability of Sb-assisted removal at 400
C
Prem_Bi_Sb_420 = P(1,6);    % Probability of Sb-assisted removal at 420
C
Pexc_Bi_As_400 = P(1,7);    % Probability of anion exchange, As
displacing Bi, at 400 C
Pexc_Bi_As_420 = P(1,7);    % Probability of anion exchange, As
displacing Bi, at 420 C
Pexc_Bi_Sb_400 = P(1,8);    % Probability of anion exchange, Sb
displacing Bi, at 400 C
Pexc_Bi_Sb_420 = P(1,8);    % Probability of anion exchange, Sb
displacing Bi, at 420 C

% Sb second:
```

```
Rdes_Sb_400    = P(2,1);    % Rate of Sb self-desorption at 400 C,
normalized to In flux (unitless)
% Rdes_Sb_420    = P(2,2);    % Rate of Sb self-desorption at 420 C,
normalized to In flux (unitless)
Rinc_Sb_400    = P(2,3);    % Rate of Sb incorporation at 400 C,
normalized to In flux (unitless)
% Rinc_Sb_420    = P(2,4);    % Rate of Sb incorporation at 400 C,
normalized to In flux (unitless)
Prem_Sb_As_400 = P(2,5);    % Probability of As-assisted removal at 400
C
Prem_Sb_As_420 = P(2,5);    % Probability of As-assisted removal at 420
C
Prem_Sb_Bi_400 = P(2,6);    % Probability of Bi-assisted removal at 400
C
Prem_Sb_Bi_420 = P(2,6);    % Probability of Bi-assisted removal at 420
C
Pexc_Sb_As_400 = P(2,7);    % Probability of anion exchange, As
displacing Sb, at 400 C
Pexc_Sb_As_420 = P(2,7);    % Probability of anion exchange, As
displacing Sb, at 420 C
Pexc_Sb_Bi_400 = P(2,8);    % Probability of anion exchange, Bi
displacing Sb, at 400 C
Pexc_Sb_Bi_420 = P(2,8);    % Probability of anion exchange, Bi
displacing Sb, at 420 C

% As third:
Rdes_As_400    = P(3,1);    % Rate of As self-desorption at 400 C,
normalized to In flux (unitless)
% Rdes_As_420    = P(3,2);    % Rate of As self-desorption at 420 C,
normalized to In flux (unitless)
Rinc_As_400    = P(3,3);    % Rate of As incorporation at 400 C,
normalized to In flux (unitless)
% Rinc_As_420    = P(3,4);    % Rate of As incorporation at 400 C,
normalized to In flux (unitless)
Prem_As_Sb_400 = P(3,5);    % Probability of Sb-assisted removal at 400
C
Prem_As_Sb_420 = P(3,5);    % Probability of Sb-assisted removal at 420
C
Prem_As_Bi_400 = P(3,6);    % Probability of Bi-assisted removal at 400
C
Prem_As_Bi_420 = P(3,6);    % Probability of Bi-assisted removal at 420
C
Pexc_As_Sb_400 = P(3,7);    % Probability of anion exchange, Sb
displacing As, at 400 C
Pexc_As_Sb_420 = P(3,7);    % Probability of anion exchange, Sb
displacing As, at 420 C
Pexc_As_Bi_400 = P(3,8);    % Probability of anion exchange, Bi
displacing As, at 400 C
Pexc_As_Bi_420 = P(3,8);    % Probability of anion exchange, Bi
displacing As, at 420 C

%%%%%%%%%%%%%%%%%%%%%%%%%%%%%%%%%%%%%%%%%%%%%%%%%%%%%%%%%%%%%%%%%%%%%%%%

% Calculate characteristic temperature of incorporation coefficients.
Tc = [0, 0, 0];
```

```
for i=1:3
    Tc(i) = (420 - 400)/log(Sinc(i,1)/Sinc(i,2));
end

% Manually calculate the incorporation rates at 420 C from the 400 C
rates.
Rinc_Bi_420 = Rinc_Bi_400*exp(-(420 - 400)/Tc(1));
Rinc_Sb_420 = Rinc_Sb_400*exp(-(420 - 400)/Tc(2));
Rinc_As_420 = Rinc_As_400*exp(-(420 - 400)/Tc(3));

% The Sb and As desorption rates are constant with growth temperature.
Rdes_Sb_420 = Rdes_Sb_400;
Rdes_As_420 = Rdes_As_400;

% Unpack flux ratios.
F_Bi = F(1,:);
F_Sb = F(2,:);
F_As = F(3,:);

% Unpack mole fractions.
x = MF(1,:);
y = MF(2,:);
z = MF(3,:);

% Calculate excess fluxes. If this quantity is negative, then set
% it to zero.
Fxs_Bi = F_Bi - x;
Fxs_Sb = F_Sb - y;
Fxs_As = F_As - z;

for i=1:length(F_Bi)
    if (Fxs_Bi(i) < 0)
        Fxs_Bi(i) = 0;
    end

    if (Fxs_Sb(i) < 0)
        Fxs_Sb(i) = 0;
    end

    if (Fxs_As(i) < 0)
        Fxs_As(i) = 0;
    end
end

%%%%%%%%%%%%%%%%%%%%%%%%%%%%%%%%%%%%%%%%%%%%%%%%%%%%%%%%%%%%%%%%%%%%%%%%%%%%

% Solve for the Bi, Sb, and As mole fractions and surface coverage
% fractions. Initialize the outputs.
theta_Bi = 0*T;
theta_Sb = 0*T;
theta_As = 0*T;
```

```
xf = 0*T;
yf = 0*T;
zf = 0*T;

% Loop on each sample.
for i=1:length(T)
    % This condition is used to eliminate issues related to floating-
    point representation.
    if (T(i) > 0.999*400) && (T(i) < 1.001*400)
        % Bismuth model at 400 C
        theta_Bi(i) = F_Bi(i)*(1 + F_As(i)*Pexc_Bi_As_400 +
F_Sb(i)*Pexc_Bi_Sb_400)/((Rdes_Bi_400 + Rdr(i) +
Fxs_As(i)*Prem_Bi_As_400 + Fxs_Sb(i)*Prem_Bi_Sb_400)*(1 +
F_As(i)*Pexc_Bi_As_400 + F_Sb(i)*Pexc_Bi_Sb_400) + Rinc_Bi_400);

        xf(i) = Rinc_Bi_400*F_Bi(i)/((Rdes_Bi_400 + Rdr(i) +
Fxs_As(i)*Prem_Bi_As_400 + Fxs_Sb(i)*Prem_Bi_Sb_400)*(1 +
F_As(i)*Pexc_Bi_As_400 + F_Sb(i)*Pexc_Bi_Sb_400) + Rinc_Bi_400);

        % Antimony model at 400 C
        theta_Sb(i) = F_Sb(i)*(1 + F_As(i)*Pexc_Sb_As_400 +
F_Bi(i)*Pexc_Sb_Bi_400)/((Rdes_Sb_400 + Fxs_As(i)*Prem_Sb_As_400 +
Fxs_Bi(i)*Prem_Sb_Bi_400)*(1 + F_As(i)*Pexc_Sb_As_400 +
F_Bi(i)*Pexc_Sb_Bi_400) + Rinc_Sb_400);

        yf(i) = Rinc_Sb_400*F_Sb(i)/((Rdes_Sb_400 +
Fxs_As(i)*Prem_Sb_As_400 + Fxs_Bi(i)*Prem_Sb_Bi_400)*(1 +
F_As(i)*Pexc_Sb_As_400 + F_Bi(i)*Pexc_Sb_Bi_400) + Rinc_Sb_400);

        % Arsenic model at 400 C
        theta_As(i) = F_As(i)*(1 + F_Sb(i)*Pexc_As_Sb_400 +
F_Bi(i)*Pexc_As_Bi_400)/((Rdes_As_400 + Fxs_Sb(i)*Prem_As_Sb_400 +
Fxs_Bi(i)*Prem_As_Bi_400)*(1 + F_Sb(i)*Pexc_As_Sb_400 +
F_Bi(i)*Pexc_As_Bi_400) + Rinc_As_400);

        zf(i) = Rinc_As_400*F_As(i)/((Rdes_As_400 +
Fxs_Sb(i)*Prem_As_Sb_400 + Fxs_Bi(i)*Prem_As_Bi_400)*(1 +
F_Sb(i)*Pexc_As_Sb_400 + F_Bi(i)*Pexc_As_Bi_400) + Rinc_As_400);

    else
        % Bismuth model at 420 C
        theta_Bi(i) = F_Bi(i)*(1 + F_As(i)*Pexc_Bi_As_420 +
F_Sb(i)*Pexc_Bi_Sb_420)/((Rdes_Bi_420 + Rdr(i) +
Fxs_As(i)*Prem_Bi_As_420 + Fxs_Sb(i)*Prem_Bi_Sb_420)*(1 +
F_As(i)*Pexc_Bi_As_420 + F_Sb(i)*Pexc_Bi_Sb_420) + Rinc_Bi_420);

        xf(i) = Rinc_Bi_420*F_Bi(i)/((Rdes_Bi_420 + Rdr(i) +
Fxs_As(i)*Prem_Bi_As_420 + Fxs_Sb(i)*Prem_Bi_Sb_420)*(1 +
F_As(i)*Pexc_Bi_As_420 + F_Sb(i)*Pexc_Bi_Sb_420) + Rinc_Bi_420);

        % Antimony model at 420 C
        theta_Sb(i) = F_Sb(i)*(1 + F_As(i)*Pexc_Sb_As_420 +
F_Bi(i)*Pexc_Sb_Bi_420)/((Rdes_Sb_420 + Fxs_As(i)*Prem_Sb_As_420 +
```

```
Fxs_Bi(i)*Prem_Sb_Bi_420)*(1 + F_As(i)*Pexc_Sb_As_420 +
F_Bi(i)*Pexc_Sb_Bi_420) + Rinc_Sb_420);

        yf(i) = Rinc_Sb_420*F_Sb(i)/((Rdes_Sb_420 +
Fxs_As(i)*Prem_Sb_As_420 + Fxs_Bi(i)*Prem_Sb_Bi_420)*(1 +
F_As(i)*Pexc_Sb_As_420 + F_Bi(i)*Pexc_Sb_Bi_420) + Rinc_Sb_420);

        % Arsenic model at 420 C
        theta_As(i) = F_As(i)*(1 + F_Sb(i)*Pexc_As_Sb_420 +
F_Bi(i)*Pexc_As_Bi_420)/((Rdes_As_420 + Fxs_Sb(i)*Prem_As_Sb_420 +
Fxs_Bi(i)*Prem_As_Bi_420)*(1 + F_Sb(i)*Pexc_As_Sb_420 +
F_Bi(i)*Pexc_As_Bi_420) + Rinc_As_420);

        zf(i) = Rinc_As_420*F_As(i)/((Rdes_As_420 +
Fxs_Sb(i)*Prem_As_Sb_420 + Fxs_Bi(i)*Prem_As_Bi_420)*(1 +
F_Sb(i)*Pexc_As_Sb_420 + F_Bi(i)*Pexc_As_Bi_420) + Rinc_As_420);

    end
end

% Assign mole fractions and surface coverage fractions to the output.
MFfit = [xf; yf; zf];
theta = [theta_Bi; theta_Sb; theta_As];

end
```

nonlincon.m

```
function [c, ceq] = nonlincon(F, MF, T, Rdr, Sinc, P)
% nonlincon
% Nonlinear constraints on the fitting parameters for the complete (Bi
+ Sb
% + As) MBE growth model.
% Nominally, the modeled mole fractions must all sum to 1: x + y + z =
1
% Nominally, the modeled surface coverage fractions must all sum to 1:
% theta_Bi + theta_Sb + theta_Bi = 1
%
% Inputs:
% F         Array of flux ratios: Bi/In, Sb/In, As/In.
% MF        Array of mole fractions: Bi, Sb, As (x, y, z)
% T         Vector of growth temperatures, in Celsius.
% Rdr       Bi Droplet accumulation rate, unitless. Measured by AFM
% Sinc      Array of average Bi, Sb, and As incorporation coefficients
at
%           400 C and 420 C, used to calculate Rinc
% P         Array of model parameters, to construct a global fitting
%           algorithm: Bi, Sb, As
%
% Outputs:
% c         Nonlinear inequality, not used.
% ceq       Nonlinear equality, the mole fractions and surface coverage
%           fractions should sum to unity. This should be equal to zero
to
%           satisfy the nonlinear equality.

% Call the MBE model function to get the modeled mole fractions and
surface
% coverage fractions.
[MFfit, theta] = MBEmodel(F, MF, T, Rdr, Sinc, P);

% Calculate the nonlinear equalities.
theta_tol = 0.10;   % Surface coverage fraction tolerance
theta_sum = theta(1,:) + theta(2,:) + theta(3,:);   % Should be equal
to one for each sample.

% Check each sample and see if the surface coverage fractions sum to
unity +/- tolerance.
ceq = zeros(1, length(MF(1,:)));

for i=1:length(MF(1,:))
    if (theta_sum(i) > 1 - theta_tol) && (theta_sum(i) < 1 + theta_tol)
        ceq(i) = 0;
    else
        ceq(i) = 1;
    end
end

% Nonlinear inequalities not used.
c = [];
```

```
end
```

chisqfun.m

```
function [chisq] = chisqfun(MFfit, MF, sigma)
% chisqfun
% Simple function to calculate the mean squared error between MFfit and
MF, weighted by variance in measured mole fraction, sigma.
chisq_Bi = sum(((MFfit(1,:) - MF(1,:)).^2)./(sigma(1,:).^2));
chisq_Sb = sum(((MFfit(2,:) - MF(2,:)).^2)./(sigma(2,:).^2));
chisq_As = sum(((MFfit(3,:) - MF(3,:)).^2)./(sigma(3,:).^2));

chisq = chisq_Bi + chisq_Sb + chisq_As;
end
```